PROTON CYCLOTRON ECHO
– a Phenomenon of Wave-Wave and Wave-Particle Interactions in Topside Sounding of the Ionosphere –

by

Guang-Ming Chen

B.Sc., University of Science and Technology of China, 1963
M.Sc., University of Alberta, 1987

ACCEPTED
FACULTY OF GRADUATE STUDIES

A Dissertation Submitted in Partial Fulfilment of the Requirements for the Degree of

DOCTOR OF PHILOSOPHY

DEAN

DATE 15 Oct 93

in the Department of Physics and Astronomy

We accept this dissertation as conforming to the required standard

Dr. R.E. Horita (Dept. of Physics and Astronomy), Supervisor

Dr. J.B. Tatum (Dept. of Physics and Astronomy), Departmental Member

Dr. D.A. VandenBerg (Dept. of Physics and Astronomy), Departmental Member

Dr. G.G. Miller (Dept. of Mathematics and Statistics), Outside Member

Dr. M.B. Hocking (Dept. of Chemistry), Outside Member

Dr. T. Watanabe (University of British Columbia), External Examiner

Department of Physics and Astronomy
University of Victoria
Victoria, B.C., Canada V8W 3P6
Fax: (604)721-7715
Tel: (604)721-7727

September 16, 1993

Terra Scientific Publishing Company (TERRAPUB)
2-24-302 Midorigaoka, Meguro-ku, Tokyo 152, Japan
Fax: 81-3-3718-4406
Tel: 81-3-3718-4403

Dear Sir:

I have adopted a figure in my dissertation from C. T. Russell (1987), The magnetosphere, in *The Solar Wind and the Earth*, edited by S.-I. Akasofu and Y. Kamide, Chapter 5, p.80, Figure 6. Could you kindly give a written permission as soon as possible? I am looking forward to hearing from you. Thank you.

Sincerely,

G.-M. Chen

Dear Dr. Chen:

Thank you for your Fax. as above. I would like to permit to use your proposed material(s).

Yours sincerely,

Keiji Oshida
Publisher, TERRAPUB

P.S. Will you please cite author's name, book name, publisher?

Department of Physics and Astronomy
University of Victoria
Victoria, B.C., Canada V8W 3P6

August 24, 1993

The Johns Hopkins University Press
701 West 40th Street
Baltimore, Maryland 21211

Dear Sir:

I have adopted a figure in my dissertation from A. T. Y. Lui (1987), Road map to magnetotail domains, in *Magnetotail Physics*, edited by A. T. Y. Lui, p. 5, Plate I.1. Could you kindly give a written permission as soon as possible? I am looking forward to hearing from you. Thank you.

Sincerely,

G.-M. Chen

PERMISSION GRANTED:

Arlene W. Sullivan, Assistant to the Director
Rights & Permissions Date: 8.30.93

THE JOHNS HOPKINS UNIVERSITY PRESS
2715 N. Charles Street
Baltimore, MD 21218-4319

= 6 SEP. 1993

Department of Physics and Astronomy
University of Victoria
Victoria, B.C., Canada V8W 3P6

August 24, 1993

Gordon and Breach, Science Publishers Ltd.
41/42 William IV Street
London W.C.2

Dear Sir:

I have adopted a figure in my dissertation from M. D. Papagiannis (1972), *Space Physics and Space Astronomy*, Chapter 2, p. 4[illegible], Figure 2.5-I. Could you kindly give a written permission as soon as possible? I am looking forward to hearing from you. Thank you.

Sincerely,

G.-M. Chen

Permission granted insofar as we are the copyright holder and provided suitable reference* is given and material is reset.

© 1972 By: GORDON AND BREACH. SCIENCE PUBLISHERS Ltd.

.....

Publisher

RIGHTS AND PERMISSIONS OFFICER

Date 16 SEP. 1993

* to: Space Physics and Space Astronomy by M. D. Papagiannis

NAGOYA UNIVERSITY

DEPARTMENT OF ELECTRICAL ENGINEERING AND ELECTRONICS
FURO-CHO, CHIKUSA-KU, NAGOYA 464 JAPAN
PHONE 052-781-5111 FACSIMILE 052-782-1992

September 3, 1993

Mr. G.-M. Chen
Department of Physics and Astronomy
University of Victoria
Victoria, B. C., Canada V8W 3P6

Dear Mr. Chen:

I received your letter of August 24, 1993. I herewith permit you to reproduce a figure in your dissertation from my paper: Excitation of electrostatic ion cyclotron waves by a power-modulated transversely excited atmosphere (TEA) CO_2 laser, *Phys. Fluids, B5*, p.1155, Figure 1 (1993).

It should be noted that the copyright of the above paper has been transferred to the American Institute of Physics. Accordingly, it may be necessary to receive the permission of the AIP to use the figure in your dissertation.

I hope you get your Ph.D. successfully.

Sincerely yours,

K. Sasaki

Dr. G.-M. Chen
Department of Physics and Astronomy
University of Victoria
Victoria, B.C., Canada V8W 3P6

September 23, 1993

American Institute of Physics
335 East 45th Street
New York, NY 10017-3483

Dear Sirs:

I would like to notify you that I have adopted a figure in my dissertation from the article of Sasaki *et al.* (1993): Excitation of electrostatic ion cyclotron waves by a power-modulated transversely excited atmosphere (TEA) CO_2 laser, *Phys. Fluids, B 5*, p.1155, Figure 1. and Dr. Sasaki has kinndly given his permission for my use. Thank you very much.

Sincerely,

G.-M. Chen

SUPERVISOR: PROFESSOR ROBERT E. HORITA

Abstract

Proton cyclotron echoes are phenomena related to the proton cyclotron frequency discovered on topside sounder swept-frequency ionograms from the Canadian satellite Alouette II in 1969. Subsequent studies were also limited to the use of the swept-frequency ionograms and devoted only to these so called regular proton cyclotron echoes. The regular proton cyclotron echoes occur on the swept-frequency ionograms at constant apparent ranges predominantly at frequencies below the electron plasma frequency f_N, and slightly above the electron cyclotron frequency f_H. In this dissertation over 2000 topside sounder ionograms (both swept-frequency mode and fixed-frequency mode) obtained from the Alouette II, ISIS I and II satellites of the Alouette-ISIS program are used to investigate proton cyclotron echoes in detail.

Examination of the combined swept-frequency and fixed ionograms indicates that the proton cyclotron echoes are also observed on the fixed-frequency ionograms. In addition to some features, such as constant apparent ranges and higher order multiple echoes, which have been already observed on the swept-frequency ionograms and also occur on the fixed-frequency ionograms, under some conditions non-constant apparent ranges and modulations in intensity of the proton cyclotron echoes on the fixed-frequency ionograms are observed.

Usually the proton cyclotron echoes on the fixed-frequency ionogram can be observed for a much longer time than on the swept-frequency ionograms due to the fixed sounding frequencies. A proton cyclotron echo can be under observation for several spin periods of the satellite if the plasma parameters encountered by the sounder are appropriate. The modulation in intensity of the

proton cyclotron echo by antenna orientation is evident. In terms of analysis of the combined swept-frequency and fixed-frequency ionograms, and the satellite orbital parameters and spin axis attitude, effects on proton cyclotron echoes of antenna orientation with respect to the earth's magnetic field are examined. It is found that higher intensity and higher harmonics of proton cyclotron echoes occur when the sounding antenna is parallel to the earth's magnetic field.

A new class of proton cyclotron echoes was discovered, which occur on electron plasma resonances. The proton cyclotron echoes on the f_H, nf_H ($n = 2, 3, 4$), f_{Q3} and f_D have been observed. The first three are checked in more detail. The proton cyclotron echoes observed on the f_H, $4f_H$, f_{Q3} and f_D resonances exhibit doublet, on the $2f_H$ resonance triplex and on $3f_H$ resonance single while the regular proton cyclotron echoes are always single. A frequency difference of about 5 – 10 Hz exists between subechoes in a doublet or triplex. The regular proton cyclotron echo seems to correspond to the first echo of the double or triple proton cyclotron echoes. No echo minus exists and most proton cyclotron echoes on the electron plasma resonances are observed at dip angles whose magnitudes are less than 8°. This new class of proton cyclotron echoes is attributed to the results of nonlinear interactions of ion and electron Bernstein waves or ion Bernstein waves and DKO mode electromagnetic waves (for the f_H resonance). Absorption phenomena on the $3f_H$, $4f_H$ and f_{Q3} resonance spikes near the proton cyclotron period on swept-frequency ionograms are observed occasionally, but not yet understood.

A theory based on nonlinear interaction of two waves is suggested to interpret proton cyclotron echoes. Many observational features of proton cyclotron echoes can be interpreted by this nonlinear interaction model of two waves.

Examiners:

Dr. R.E. Horita (Dept. of Physics and Astronomy), Supervisor

Dr. J.B. Tatum (Dept. of Physics and Astronomy), Departmental Member

Dr. D.A. VandenBerg (Dept. of Physics and Astronomy), Departmental Member

Dr. G.G. Miller (Dept. of Mathematics and Statistics), Outside Member

Dr. M.B. Hocking (Dept. of Chemistry), Outside Member

Dr. T. Watanabe (University of British Columbia), External Examiner

Contents

List of Tables

List of Figures

Acknowledgements

I wish to express my sincere thanks to Professor Robert E. Horita for suggesting this interesting topic for my dissertation and providing guidance and assistance. I value greatly his patience, support and encouragement throughout the course of this study.

I would like to thank D. B. Muldrew of the Communications Research Centre, Ottawa, for a comment in his communication to Dr. Horita which stimulated us to studying effects on proton cyclotron echoes of antenna orientation with respect to the earth's magnetic field.

My thanks are due to the staff of the Department of Physics and Astronomy, University of Victoria, for many instances of kind service and especially to Mr. C. R. Card, who spent much time scaling and labeling the ionograms and provided the excellent figures in this dissertation.

I thank the World Data Center A for Rockets and Satellites at the Goddard Space Flight Center, USA, and the Communications Research Centre in Ottawa, Canada, for providing the microfilmed Alouette II and ISIS I and II satellite ionograms and World maps for this research.

During the course of this study, I was supported by the Graduate Teaching Assistantship from the Department of Physics and Astronomy, University of Victoria, by the University of Victoria Fellowship and by the Graduate Research Assistantship from the Natural Sciences and Engineering Research Council of Canada through research grants to Dr. R. E. Horita.

Dedication

This thesis is dedicated to
Chen Xuduan
Wang Deying
Chen Yufei

Chapter 1

Introduction

A large variety of plasma-wave phenomena in the magnetosphere and the ionosphere have been detected by ground-based facilities and by receivers on board spacecraft. The term 'plasma wave' is used to denote all waves which are generated in the magnetospheric and ionospheric plasma or which have their wave characteristics significantly modified through propagation in the magnetosphere and the ionosphere. These waves may be electromagnetic or electrostatic. Naturally-occurring waves are generated by the conversion of free energy within plasma into wave energy through a variety of wave-particle interaction processes. In turn, these waves may interact with the particles and modify the distribution function characteristic of the particle populations within the plasma. Thus wave-particle interactions are very important in the magnetosphere and the ionosphere and are believed to be responsible for the generation of waves, the pitch angle distribution and the local acceleration of the charged particles, the energy transport between particles and waves. Some electromagnetic waves can propagate far enough from their source region so that their observation provides information on the remote source region.

Besides the natural plasma waves, plasma waves are also stimulated artificially by radio waves transmitted from spacecraft or from ground stations, and also by electron or ion beams injected from sounding rockets or spacecraft. For example, the plasma resonances observed in topside sounding of the ionosphere are explained to be attributed to electrostatic waves stimulated by the sounder pulse. The proton cyclotron echo observed in topside sounding of the ionosphere

is not quite understood yet. This dissertation is devoted to its investigation.

In view of the above discussion, the magnetosphere and the ionosphere are excellent laboratories for studying plasma waves. The events we will deal with (proton cyclotron echoes and topside-sounder resonances) take place in this laboratory. Thus in this chapter we introduce our laboratory – the magnetosphere and the ionosphere.

1.1 The Magnetosphere

A magnetosphere may be defined as a region in space created by the interaction between the intrinsic magnetic field or ionized atmosphere of a celestial body and a flowing magnetized plasma. Of the eight planets visited by spacecraft, four (Mercury, Earth, Jupiter and Saturn) are known to have internally-generated magnetic fields (Bagenal, 1985). Therefore, the magnetospheres for them are formed by the outflowing plasma from the sun, the solar wind, interacting with their intrinsic magnetic fields. However, there are several objects (such as comets, Venus, Mars and so on) in the solar system which are not magnetized but nevertheless strongly interact with the solar wind. So the definition of a magnetosphere is stretched to include them. Here we consider only the interaction of the earth's magnetic field with the solar wind and therefore the magnetosphere is referred to the earth's magnetosphere. The earth's magnetosphere has been surveyed in more detail than all other magnetospheres.

The magnetosphere is that region of space determined by the interaction of the solar wind with the earth's dipole-like magnetic field. It extends to about 10 – 12 earth radii ($r_E \sim 6380$ km) in the sunward direction and to more than 1000 earth radii in the anti-sunward direction from the center of the earth. It is shown schematically in Figures 1.1 and 1.2. Figure 1.1 shows a noon-midnight meridian cross-section of the magnetosphere and Figure 1.2 a three-dimensional

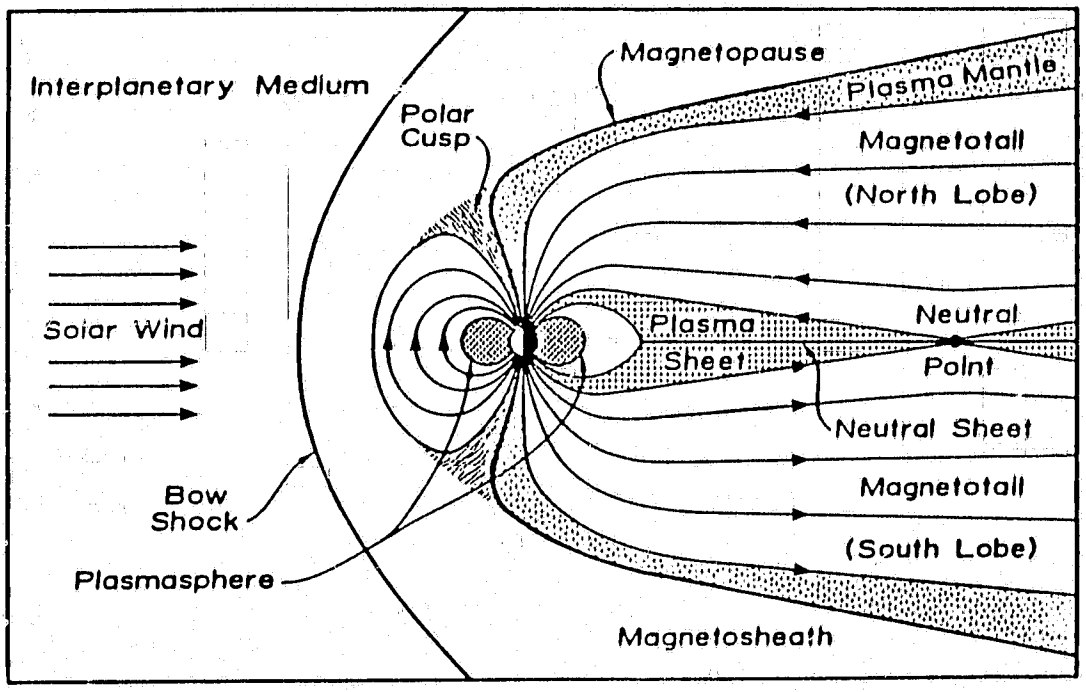

Figure 1.1: Noon-midnight meridian cross-section of the magnetosphere. The solar wind flows from left and the bow shock stands in front of the solar wind flow. The shocked flow, deflected, slowed and heated, flows around the magnetopause in the region called the magnetosheath. A small portion of the solar wind plasma enters the magnetosphere through the polar cusp. Some of this entering plasma forms a boundary layer called the plasma mantle, and some of this drifts down to the region of the neutral point where it is accelerated to form the plasma sheet. After Russell (1987).

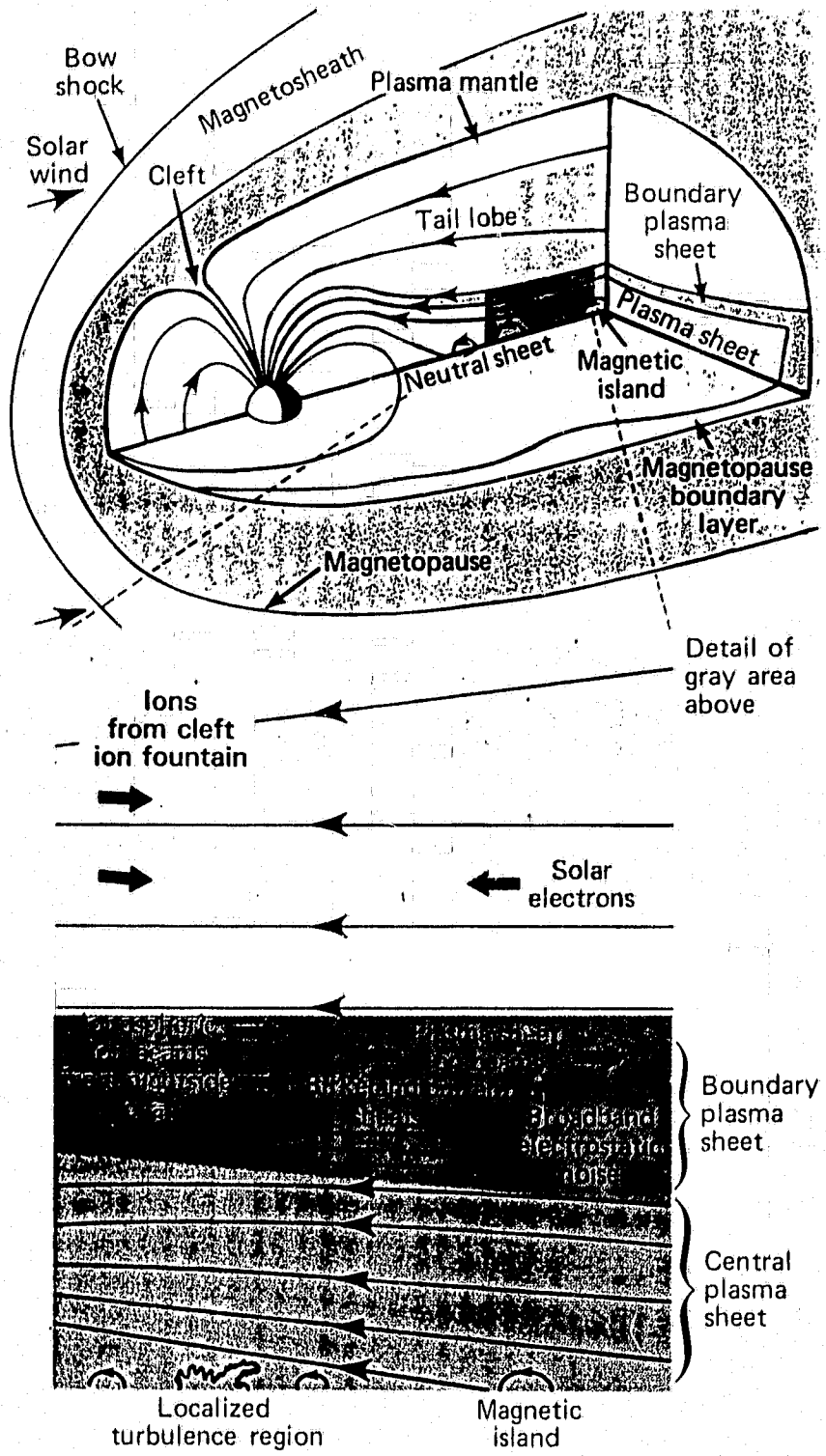

Figure 1.2: A three-dimensional of the magnetosphere, exhibiting the plasma domains within. After Lui (1987).

drawing of the magnetosphere. The name "magnetosphere" was introduced by Gold (1959). But under the name "geomagnetic cavity", it was discussed by Chapman and Ferraro (1931b), and the existence of such a cavity was anticipated by Birkeland (1908).

1.1.1 Magnetic Field Structures

The magnetosphere is bounded by the magnetopause (see Figures 1.1 and 1.2). The location and the shape of the magnetopause are determined primarily by the condition of pressure balance: the total pressures (Plasma plus magnetic field) just outside and inside of the magnetopause should be equal. Thus we may have

$$p_{sw} + \frac{B_{sw}^2}{2\mu_0} = p_{gm} + \frac{B_{gm}^2}{2\mu_0} \tag{1.1}$$

where subscripts sw and gm denote the solar wind and the geomagnetic field. The pressure p_{sw} exerted on the magnetopause depends on both the dynamic pressure $2nmv^2cos^2\psi$ and the thermal pressure nkT in the solar wind. Here ψ is the angle between the local normal to the magnetopause and upstream solar wind flow direction. Since the dynamic pressure is about two orders of magnitude greater than the thermal pressure, we may assume that

$$p_{sw} = 2nmv^2cos^2\psi \tag{1.2}$$

Since $p_{sw} \gg B_{sw}^2/2\mu_0$ and $p_{gm} \ll B_{gm}^2/2\mu_0$, we obtain

$$2nmv^2cos^2\psi = \frac{B_{gm}^2}{2\mu_0} \tag{1.3}$$

At the geomagnetic equator,

$$B_{gm} = \left(\frac{r_E}{r_e}\right)^3 B_0 \tag{1.4}$$

where r_e is the equatorial distance of the magnetopause from the earth's center, r_E the earth's radius and B_0 the magnetic induction at the earth's surface of the

geomagnetic equator. However, B_{gm} has aproximately twice its value due to the compression of the solar wind so that many more magnetic field lines is piled up near the magnetopause. Also we assume $\psi = 0$ at the geomagnetic equator. Then combining (1.3) and (1.4) yields

$$r_e = \left(\frac{B_0^2}{2\mu_0 nmv^2}\right)^{1/6} r_E \tag{1.5}$$

Take

$v = 300$ km/s
$m = 1.673 \times 10^{-27}$ kg
$n = 2 \times 10^6 \mathrm{m}^{-3}$
$B_0 = 0.3 \times 10^{-4}$ tesla
$\mu_0 = 4\pi \times 10^{-7}$ henry/m

thus we obtain

$$r_e \approx 10 r_E \tag{1.6}$$

This result is in good agreement with observations. The geocentric average distance to the subsolar point of the magnetopause is $10 - 11\ r_E$, but occasional extreme excursions are reached as close as $6.6\ r_E$ or as far as $18\ r_E$ depending on the solar wind dynamic pressure $2nmv^2$.

On the night side, the magnetic field lines are stretched out along the solar wind direction to form the magnetotail. Thus behind the earth the magnetopause becomes a cylindrical surface. The radius of the magnetotail is about $40\ r_E$ and remains the same for at least $100\ r_E$. The magnetotail extends for more than $1000\ r_E$ in space.

In the central part of the magnetotail, close to the anti-solar line, the direction of the magnetic field reverses in a short distance along the north-south direction. The field lines in the northern hemisphere are directed towards the earth and the ones in the southern hemisphere are directed away from the earth.

There is therefore a narrow zone with zero field. This neutral layer has a thickness of about 1,000 km and is called the neutral sheet.

At the interface between the day and night sides of the magnetosphere, there are two regions, one north and one south, of the magnetic field lines with a funnel-shaped geometry, known as the clefts or polar cusps. The neutral points exist in the polar cusps. The low magnetic fields in these regions allow some penetration of the solar wind. The outer parts of the magnetotail, which include the field lines that originate in the polar caps are known as the lobes.

Complex magnetic field structures, such as flux ropes and magnetic islands, are occasionally observed. Flux ropes are associated with strong currents along the magnetic field lines, giving rise to the field lines spiraling like the fibers of a rope. Magnetic islands, in which the entrapped magnetic field lines form closed loops, can be considered as a degenerate case of magnetic flux ropes.

1.1.2 Plasma Structures

With respect to plasma, the magnetopause behaves in a similar way as with respect to the magnetic field lines; it acts as a barrier and forces the solar wind plasma to flow around the magnetosphere. Thus the magnetopause may be regarded as a boundary that separates distinctly different regions – the solar wind plasma region and the magnetospheric plasma region. The average thickness of the magnetopause is about 600 – 800 km (Lundin, 1988). Interior to the magnetopause lies the boundary layer or plasma boundary layer. The boundary layer is the major region of solar wind mass, energy and momentum transfer into the magnetosphere (Burch, 1987; Lundin, 1988). Its characteristic feature is a mixture of magnetosheath and magnetosphere plasmas flowing tailward. From a topological and phenomenological point of view the boundary layer may be separated into two regions, the high-latitude boundary layer (HLBL) and the

low-latitude boundary layer (LLBL). The HLBL and LLBL are topologically interfaced with the polar cusp.

High-Latitude Boundary Layer (HLBL)

The HLBL or the plasma mantle is topologically the boundary region connected to the dayside polar cap just poleward of the cusp. It is formed by the plasma of predominantly magnetosheath origin flowing tailward along the geomagnetic field lines at a speed slightly less than the exterior magnetosheath plasma flow. The HLBL plays an important role in energy transfer. The solar wind mass and energy are transferred into the inner magnetosphere from it. The magnetosheath plasma is also believed to be brought to the central plasma sheet from the HLBL (Cowley, 1980).

Low-Latitude Boundary Layer (LLBL)

The LLBL is the low-latitude portion of the boundary layer which extends all the way from local noon to far downtail. It was also suggested by Eastman *et al.* (1976) that the LLBL is the major site of the solar wind energy and momentum transfer into the magnetosphere. The plasma flow in the sunward section of the LLBL also has a considerable cross-field flow component, as opposed to the HLBL where the plasma flow is preferentially field aligned. The LLBL is also believed to the main source region for solar wind plasma entry into the plasma sheet (Eastman *et al.*, 1985). Magnetosheath plasma would enter into the central plasma sheet along the flank of the magnetotail. This contrasts with the HlBL where magnetosheath plasma enters the central plasma sheet through the tail lobe.

Polar Cusp

At the magnetic polar cusp, magnetosheath plasma extends so deep into the magnetosphere that the name "boundary layer" is not appropriate: The entire funnel of the field lines, down to the upper atmosphere, is filled with magnetosheath-like plasma. This region is referred to by some as the "polar cusp" or by others as the "magnetospheric cleft". Its outmost part, near the magnetopause, is called the "entry layer", which is topologically connected to the equatorward edge of the dayside magnetic polar cusp. Characteristic of the entry layer is a plasma density almost as high as in the exterior magnetosheath but generally lacking the strong anti-sunward plasma flow. It was believed to be the main entry region of the solar wind into the magnetosphere.

Magnetotail

A large portion of the magnetotail consists of two low plasma density regions known as the tail lobes, one in the northern half of the magnetotail and the other in the southern half. Particles populating this region include ions from the polar cusp, ions from the polar region at low altitudes, and electrons from the solar wind entered into the tail lobe on open field lines.

Bordering the tail lobe at its lower latitude interface is the plasma-sheet boundary layer. This region is often the most dynamic plasma domain of the magnetotail, where ion beams coming from the earth and from further downstream are often found. It is also where a lot of plasma wave activities are detected. Magnetic field-aligned currents, flowing toward or away from the earth are often observed. These activities gradually decrease as one approaches the central plasma sheet. The plasma sheet as whole (i.e., the central plasma sheet and the plasma-sheet boundary layer) is thinnest near the midnight region and is about twice as thick near the flanks of the magnetotail. The plasma energy

density is comparable to the magnetic field energy density in the plasma-sheet region.

In the middle of this reservoir of particles in the plasma sheet lies the neutral sheet, where the magnetic field is very weak (a few nanoteslas).

Plasmasphere

For all the plasma structures discussed so far, the supplier of the major part of the plasma population is ultimately the solar wind. It, however, is not the sole source. A smaller but significant part of the plasma sheet population comes from the earth's ionosphere. There is also evidence for an ionospheric contribution to the plasma mantle (Hultqvist, 1982).

A region populated almost entirely by the plasma from the ionosphere is the plasmasphere, located deep within the inner magnetosphere; it extends from the ionosphere outward to a relatively sharp boundary (called the plasmapause), whose location is somewhat variable but typically coincides with a shell of magnetic field lines crossing the equator at distance from 4 to 6 r_E. The plasma in this region is relatively dense and cold, with number densities ranging from $\geq 10^{10}/\mathrm{m}^3$ just above the top of the ionosphere to values of the order of $10^8/\mathrm{m}^3$ near the plasmapause, with thermal energies of the order of a few eV or less.

Ring Current

Finally, the complex region generally named the ring current forms the interface between the plasmasphere on the inside and the plasma sheet on outside. A major source of plasma for the ring current is inward transport of the plasma from the plasma sheet, including both its solar wind and its ionosphere-source components. Significant electric currents exist in this region. These currents produce magnetic disturbances observable on the earth that have long been

attributed (Chapman and Ferraro, 1931) to a "ring current" in space.

1.1.3 Bow Shock and Magnetosheath

The bow shock and the magnetosheath lie to the outside of the magnetopause but they are very important and very closely related to the magnetosphere.

In considering a flow at supersonic uniform velocity past an obstacle, no signal can be propagated upstream. The flow ahead of the obstacle has no way of knowing that the obstacle exists, and therefore can not be modified by the presence of the obstacle. However, the flow can not reach the obstacle with the same uniform supersonic velocity because the boundary condition for the mass flow requires that at the surface of the obstacle the normal component of the flow velocity should vanish. Hence the formation of a "bow wave" is needed ahead of the obstacle. The bow wave is mathematically described as a surface across which the normal component of the flow velocity, as well as the density, the pressure and the temperature, undergo discontinuous changes. Physically, the transition occurs though a layer of finite thickness. Conservation equations for mass, momentum, and energy are applied to determine the velocity, the density, the pressure and the temperature on one side of the bow wave in terms of these quantities on the other side. As the flow crosses the bow wave, its velocity suddenly decreases while its temperature and density increase. The result is that the velocity becomes subsonic, and may receive "information" about the presence of the obstacle.

The above idea may be applied when the supersonic solar wind meets an obstacle, the magnetopause, in its path. Therefore, a bow wave (usually called the bow shock) should be formed ahead of the magnetopause. But more careful analysis reveals difficulties with the above idea. All shocks must be dissipative in an ordinary hydrodynamic situations. The dissipation usually takes the form

of collisions. However, in the solar wind collisions are often negligible, so that the bow shock can not take the form of such a collisional shock. The question of the "collisionless shock" in plasma has been actively investigated (Colburn and Sonett, 1966; Schwartz, 1985). It has been suggested that microinstabilities and turbulence of various kinds may replace collisions as the agency responsible for the dissipation (Tidman, 1967; Schwartz, 1985). The bow shock has been observed by *in situ* spacecraft measurements.

The magnetosheath is a transition region between the bow shock and the magnetopause, where the solar wind is slowed down to subsonic speeds and undergoes a deflection which causes it to envelop the magnetosphere.

1.2 The Ionosphere

According to the IEEE Standard (1969) the ionosphere is defined as "that part of a planetary atmosphere where ions and electrons are present in quantities sufficient to affect the propagation of radio waves". Here we consider only the earth's ionosphere. The ionosphere is a part of the earth's atmosphere extending from approximately 70 km to 1000 km in height above the surface of the earth.

The existence of the ionosphere, as an electrically conducting region of the atmosphere, was first advanced by Stewart (1878). He suggested that the most probable cause of the daily variations in the earth's magnetic field was the presence of electric currents flowing in the upper atmosphere. Marconi's successful experiments in 1901 of radio communication across the Atlantic (Fleming, 1902) prompted Heaviside (1902) and Kennelly (1902) to suggest independently the existence of an electrically conducting layer at a height of the order of 100 km to explain the reflection of radio waves. The final experimental proof of the existence of the ionosphere was carried out by Appleton and Barnett (1925) and by Breit and Tuve (1925).

1.2.1 Structure of the Ionosphere

The most important parameter in a description of the ionosphere is the electron density. A typical electron density profile against height for daytime is shown in figure 1.3. The ionosphere is usually classified into D, E and F regions or layers. The lowest layer is called the D-layer which extends in height from about 60 to 85 km. It is present only during the daytime. The peak electron density of the D-layer occurs near 80 km and is of the order of 3×10^9 electrons/m^3. The middle layer is called the E-layer. It extends from 85 km to about 150 km and has a daytime maximum electron density of about $\sim 10^{11}$ electrons/m^3 at a height of around 115 km. Quite often the valley between the D-layer and the E-layer is not very obvious. During the night the electron density decreases by at least two orders of magnitude and the E-layer disappears. Above the E-layer is the F-layer. The F-layer is more heavily ionized. It extends from 150 to about 1000 km. The F-layer may be subdivided into the F_1-layer and F_2-layer. The F_1-layer is present like the D- and E-layers only during the daytime. It extends from 150 to 200 km with a maximum electron density of 2×10^{11} electrons/m^3 at a height of about 180 km. The F_2-layer extends from 200 to roughly 1000 km and has a daytime electron density maximum near 250 km of about 5×10^{11} electrons/m^3. During the night the D-, E-, and F_1-layers disappear and the ionosphere takes the form of a single layer, called the F-layer, with a maximum electron density of about 10^{11} electrons/m^3 in the vicinity of 350 km.

Above the F_2-layer is the plasmasphere. The plasmasphere basically follows the rotation of the earth and has the shape of a doughnut, very much like the volume formed by the lines of the earth's magnetic field which keeps the plasmasphere rotating with the earth. The boundary of the plasmasphere is called the plasmapause, which at the equatorial plane occurs at a geocentric distance of 4 to 5 r_E. At the plasmapause the electron density drops sharply from

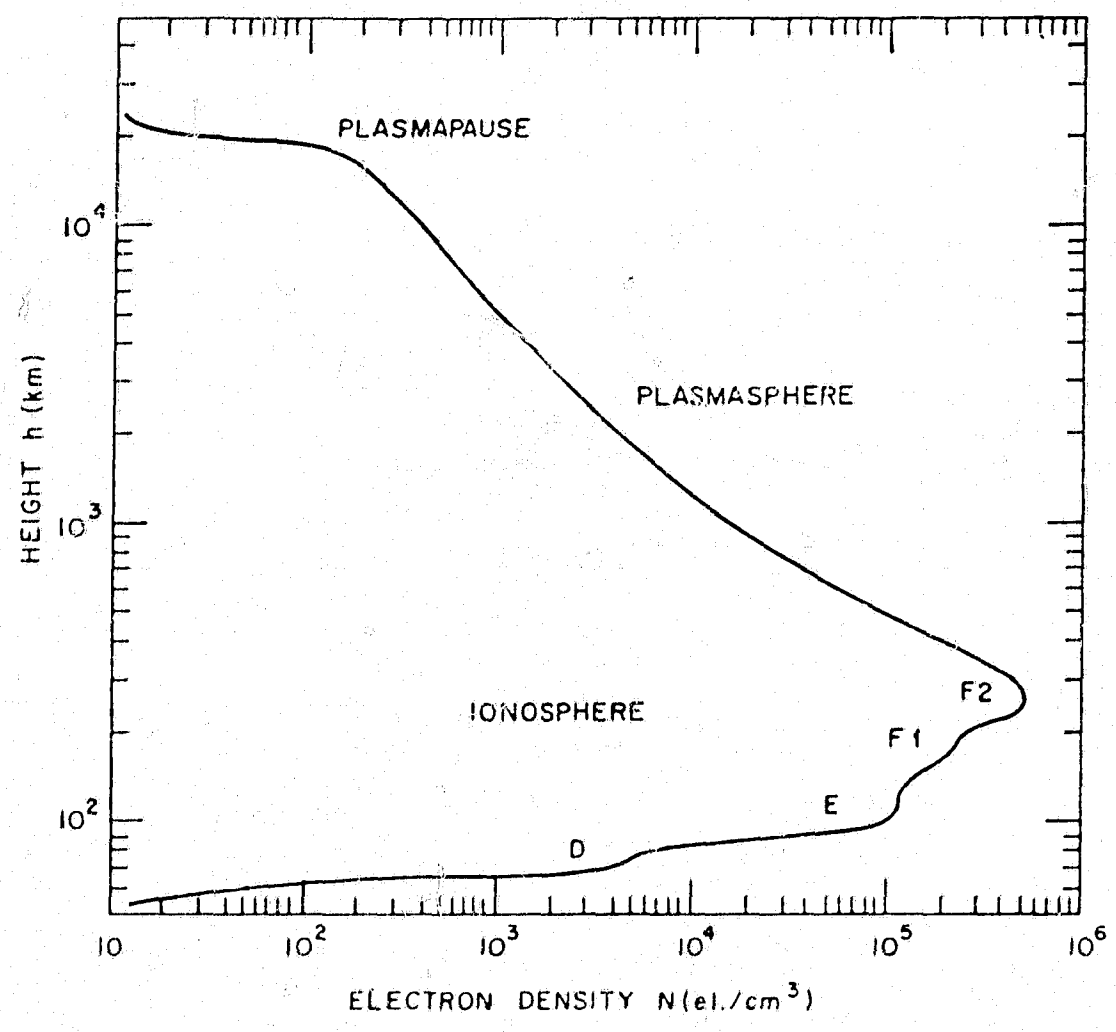

Figure 1.3: A typical daytime profile of the ionosphere and the plasmasphere. Modified from Papagiannis (1972).

$\sim 10^8$ to $\sim 10^6$ electrons/m^3. The plasmasphere is filled with thermal plasma (a plasma with a Maxwell's distribution of velocities and a temperature of a few thousand degrees Kelvin) which diffuses upwards from the upper ionosphere.

1.2.2 Layer Formation of the Ionosphere

The ionosphere is created through the photoionization process of the solar radiation. The rate of production of electron ion pairs per unit volume is given by

$$Q = \sigma n S \tag{1.7}$$

where σ is the effective ionization cross section of a given constituent gas, n its number density, and S the local intensity of the ionizing solar radiation. Incoming ultraviolet radiation and X-rays from the sun ionize the earth's atmosphere. At great heights of the order 1000 km or more the medium is almost fully ionized, but so tenuous that the ion and electron densities are small. At lower levels there is more gas to be ionized so that the radiation is more strongly absorbed and the ion and electron densities are greater. At still lower levels the radiation has been used up so that the degree of ionization is small again. The region where the ion and electron densities are greatest is the ionosphere.

The layers in the ionosphere are formed because the ionizing radiation from the sun is not monochromatic and because the atmosphere consists of several different constituents which are ionized at different wavelengths of the solar radiation spectrum. The height where maximum ionization occurs depends on the absorption of the air for the ionizing constituent of the solar radiation, and the mechanism by which ions and electrons are removed. Different ionizing constituents give maxima at different heights. Thus different ionospheric layers are formed. In the D-layer cosmic rays and the Lyman$-\alpha$ radiation (1216 $\mathring{A}$) ionize NO. In the E-layer the ionization is produced by solar X-rays in the 30–

100 $\mathring{A}$, by soft X-rays and by ultraviolet radiation in the range between 100 $\mathring{A}$ and the Lyman$-\beta$ at 1026 $\mathring{A}$. The main ions in the E-layer are NO^+ and O_2^+. In the F-layer the principal ionizing agent is the sun's ultraviolet radiation in the 200 to 900 $\mathring{A}$ range. The main atmospheric constituent which is ionized is O_2.

1.2.3 Difference between the Ionosphere and the Magnetosphere

In the F-layer the ion and electron density are only about 10^{-5} of the density of neutral particles, and in the E-layer the figure is about 10^{-11}. Thus gravity, acting mainly on the neutral particles, exerts a dominating control on the hydrostatic configuration of the medium. Hence the ionized layers tend to keep horizontally stratified.

The earth's magnetic field **B** is approximately that of a magnetic dipole near the earth's center. Its total field induction is given by

$$B = \frac{M}{r^3}(1 + 3sin^2\phi)^{1/2} \tag{1.8}$$

where M is the dipole moment of the earth's dipole magnetic field, r the distance from the earth's center and ϕ the geomagnetic latitude. A charged particle gyrating in the magnetic field has the magnetic moment $\mu = \frac{1}{2}mv_\perp^2/B$ and hence feels a force, which is given by (Jackson, 1975; Nicholson, 1983)

$$F = -\mu \bigtriangledown B \tag{1.9}$$

where m is mass of a charged particle gyrating in the earth's magnetic field and $v_\perp$ is the particle's velocity component perpendicular to the earth's magnetic field. The gravitational force per unit volume is ρg where ρ is the density of the air and **g** is the gravitational acceleration. Note the magnetic force and the gravitational force have opposite directions. These two forces are about equal at a height of 300 – 400 km. Gravity exerts a strong control up to heights of

the order of 1000 km. Above 1000 km the structure of the atmosphere is mainly controlled by the magnetic field and hence is no longer horizontally stratified but more like the structure formed by the earth's dipole magnetic field. This is the magnetosphere.

The magnetosphere is a fully ionized ion plasma and therefore a very good electrical conductor. In a perfectly conducting plasma, magnetic field lines behave as if they move with the plasma and hence this leads to the concept of "freezing in" of the magnetic field. The shape of the magnetosphere is also influenced by the solar wind. The solar wind is also a fully ionized plasma and a good conductor. They cannot quickly penetrate into each other, because they are 'frozen'. But the solar wind distorts the shape of the earth's magnetic field so that the magnetosphere is of its unique shape.

Chapter 2

Topside Sounding of the Ionosphere

Since proton cyclotron echoes were first observed in topside sounding of the ionosphere, here we introduce what is meant by "topside sounding" of the ionosphere and describe the instrumentation and the method of observing proton cyclotron echoes. The most important parameter in a description of the ionosphere is the electron number density N, and much effort has been devoted to its observation. Prior to about 1960 the knowledge of the ionosphere was obtained only from ground observations by radio methods. From about 1960 onwards rockets and satellites began to be used and it became possible for the first time to study the ionosphere at heights h above the maximum of $N(h)$ in the F_2 layer, that is the region called the topside of the ionosphere. The ionosonde technique employed by a satellite above the F_2 layer is similar to that used on the ground. This is called topside sounding of the ionosphere. The topside sounding has proven to be extraordinarily fruitful not only because of the information obtained about the structure of the topside ionosphere, but also because of the discoveries of the new phenomena due to the sounder being embedded in the plasma, such as proton cyclotron echoes, electron plasma resonances and so on.

2.1 Ground Observations of the Ionosphere

Ionospheric echo sounding was originally used in the classical pulse sounding experiments of Breit and Tuve (1925, 1926). Short pulses of radio waves from a transmitter are sent vertically upwards and return to a receiver on the ground

after reflection in the ionosphere. The time of travel t is measured. The combination of a swept-frequency pulse transmitter and an automatically tuned receiver is called the ionosonde. This is the same as the technique used in radar. If the pulse travelled entirely in free space it would have to go to a height $h' = \frac{1}{2}ct$ called the equivalent or apparent height. In fact, the pulse speed slows in the ionosphere, and therefore the apparent height is always greater than the true height of reflection. The apparent height is strongly frequency dependent. The apparent-height-versus-frequency record is called the ionogram.

Because of the earth's magnetic field the ionosphere is birefringent with the result that a transmitted radio pulse splits into two modes which travel independently at different group velocities and different polarizations. These are called the ordinary (O) and extraordinary (X) modes (or Waves). As the sounding frequency is increased, the electron number density required to reflect the transmitted signal increases until reflection occurs at a height of maximum electron density. Above a critical frequency corresponding to the electron number density at the peak of the F_2 layer, reflection can no longer take place and the ionosphere becomes transparent to the sounding signal.

For the O-wave the electron number density is given in SI units by

$$N = \frac{4\pi^2 \epsilon_0 m}{e^2} f^2 \simeq 0.0124 f^2 \tag{2.1}$$

N = electron number density

f = frequency of reflected sounding signal

ϵ_0 = permittivity of free space

m = mass of the electron

e = charge of the electron.

However considerable analysis is needed to obtain the vertical electron distribution, $N(h)$ profile, from $h'(f)$ curves. Since the pulse travels with the group

velocity u, the apparent height can be written as

$$h' = \frac{1}{2}ct = c\int_0^{h_r} \frac{dh}{u} = \int_0^{h_r} \mu'(f,N)dh \tag{2.2}$$

where h_r is the real height of reflection of the pulse and μ' the the group refractive index that depends on the electron number density and the frequency of the pulse. We wish to solve equation (2.2) to obtain $N(h)$. This is accomplished by writing it as an integral with respect to plasma frequency instead of height (which assumes that N and f_N vary monotonically with height)

$$h'(f) = \int_0^f \mu'(dh/df_N)df_N + h_r(0) \tag{2.3}$$

where $h_r(0)$ is the height of the base of the ionosphere, below which it is assumed that $f_N = 0$. At this base the real and apparent heights are equal. A good review of the ways of inverting equation (2.3) has been given by Thomas (1959). The methods of solving the integral equation (2.3) mainly fall into two classes, "lamination" and "polynomial." The former, represented by the "matrix method" of Budden (1955), replaces the integration in (2.3) by a summation over a number of thin slabs while the latter assumes that the function $h(f_N)$ can be represented by a polynomial in f_N (Titheridge, 1961).

Prior to about 1960 our knowledge of the structure of the ionosphere was mainly obtained from the ground observations by the above radio method. Even when ionospheric sounding had been brought to a high degree of refinement, it had the inherent deficiency that it provided $N(h)$ only up to the peak of the F_2 layer. Thus little had been learned about the "topside" of the ionosphere. In about 1958, the topside sounding of the ionosphere began to look feasible after the Sputnik and Explorer satellites were launched. From about 1960 onwards rockets and satellites began to be used and it became possible for the first time to study the ionosphere at heights above the maximum of $N(h)$ in the F_2 layer, which was called the topside of the ionosphere. An ionospheric sounder, which

is similar to the use of an ionosonde on the ground, carried with a satellite above the peak of the F_2 layer sounds the ionosphere from above.

2.2 The Alouette-ISIS Program

The concept of a joint topside sounder program between Canada and the United States arose during the second half of the International Geophysical Year (July 1957 to December 1958). One highlight of the IGY cooperation was the very successful U.S./Canadian rocket program conducted at Fort Churchill, Canada, which, in a sense, was a precursor to the Alouette-ISIS program. Since then topside sounder experiments were proposed and discussed by ionospheric research workers in a number of countries, including West Germany, Great Britain, the United States, and Canada. A joint U.S./Canadian effort to investigate the topside of the ionosphere began at the end of 1958 on the Topside Sounder program at the Goddard Space Flight Center (GSFC) of NASA and Central Radio Propagation Laboratory (CRPL) of the National Bureau of Standards in the U.S.A., and at the Defence Research Telecommunications Establishment (DRTE) of the Defence Research Board in Canada. Great Britain participated in the program in 1961. Until 1963 this was named the Topside Sounder program. This program led to the first topside sounder satellite, Alouette I, launched on September 29, 1962. The satellite was built in Canada and launched by the United States.

On December 23, 1963, Canada (the Defence Research Board) and the United States (NASA) agreed to a continued and expanded program of satellite studies of the ionosphere (International Satellites for Ionospheric Studies, ISIS). The expanded program led to three additional Canada-built and U.S.-launched satellites: Alouette II, ISIS I and ISIS II; and two U.S.-built satellites: Explorer XX and Explorer XXXI. International participation was increased to include France, Japan, and Norway after 1966; India, New Zealand, and Australia after

1971; and Finland after 1977. To 1986, over 50 research groups and agencies had made use of topside sounder data. The topside sounder, however, was only one of many experiments included in the Alouette-ISIS program. Collectively, these satellites have provided continuous observations of the topside ionosphere from 1962 until the present day (1993) for over 30 years. Reviews of the topside sounding of the ionosphere and the Alouette-ISIS program have been given by Chapman and Warren (1968), and Jackson (1986), especially, the special issue, Topside Sounding and the Ionosphere, of the *IEEE Proceedings* (June 1969), included 46 papers which were all based upon the Alouette-ISIS program.

2.2.1 Early Experiments

Several exploratory experiments were conducted prior to the launching of a full scale topside sounder satellite, in order to establish the feasibility of the technique and to obtain some preliminary data of the environment.

A radiometer for measuring the intensity of radio noise in the topside ionosphere at 1.8 MHz was constructed and placed in the U.S. satellite Transit 2A (Chapman and Molozzi, 1961), which was launched on June 22, 1960. The measured value of the cosmic noise provided the required design information.

A rocket experiment was flown on June 14, 1961 to test the technique of extending from a spinning vehicle the 22.9-m antennas needed for efficient radiation of the sounder transmissions (Molozzi and Richardson, 1967). Two antenna units were flown on the rocket; one of the antennas extended its full length of 22.9 m, the other extended three-quarters of its length. The engineering information obtained was adequate for specifying the modifications of the antennas used in the Alouette and Explorer XX satellites.

Feasibility of the topside sounding technique was established by two rocket tests instrumented by Airborne Instruments Laboratory (AIL). The first one was

launched on June 24, 1961, carrying a topside sounder with the fixed-frequencies 4.07 and 5.97 MHz; the second was launched on October 31, 1961, carrying a topside sounder with single frequency 4.07 MHz only. The required engineering information was obtained and, in addition, important new phenomena were observed (Knecht *et al.*, 1961; Knecht and Russell, 1962). Especially, the evidence of plasma resonances in the topside ionosphere was first observed.

2.2.2 Alouette I (launched September 29, 1962)

The primary purpose of the Alouette I was to investigate the geographic and diurnal properties of the topside ionosphere at altitudes up to 1000 km. The orbit was nearly circular at 1000 ± 60 km altitude with an inclination to the equator of 80.5° and a period 105.4 min.

Operating frequencies of the sounder in Alouette I change at an average rate of about 1 MHz per sec., sampling the band of frequencies between about 0.5 and 12 MHz. Cycle duration took 18 sec. The operating frequencies were chosen to be those that would propagate from the satellite and be reflected from the ionosphere. Pulse lengths of about 100 μs were similar to those used for ground ionosondes, and pulse repetition frequency was 67/sec.

A dipole antenna 45.7 meters from tip to tip was used for the band 0.5 to 5 MHz, while one 22.9 meters long was used from 5 MHz upward. the two dipoles were perpendicular to the spin axis and to each other.

Alouette I was spin-stabilized with the spin axis (at the time of launch) normal to the plane of the ecliptic. The initial spin rate after antenna deployment was 1.4 rpm. The spin rate, however, decreased down to 0.9 rpm at the end of 1 year (Mar and Garrett, 1969). After a few years, this rapid decay in spin rate caused Alouette I to become gravity-stabilized with the long antennas aligned with the local vertical.

2.2.3 Explorer XX (launched August 25, 1964)

Explorer XX was developed in the United States as a part of the International Topside Sounder program. Explorer XX was initially planned to be a first-generation topside sounder satellite because of its simplicity compared with Alouette I. However, it was delayed by problems with the Scout launch vehicle, and Alouette I was launched first. Explorer XX was launched into a nominally circular orbit at 1000 km (perigee 870 km, apogee 1019 km), similar to that of Alouette I, with an inclination of 79.9° and a period of 103.9 min.

The topside sounder operated on six fixed frequencies: 1.50, 2.00, 2.85, 3.72, 5.47 and 7.22 MHz. The sounder completed its 6-frequency sounding in about 0.1 sec, during which time the satellite would travel less than 1 km along its orbit. The time required for a complete sounding on Alouette I was about 18 sec, corresponding to a horizontal displacement of 126 km. Thus, the Explorer XX sounder provided a horizontal resolution considerably greater than that of Alouette I. The frequency resolution (or the vertical resolution), however, was two orders of magnitude greater on Alouette I. So the two sounder techniques were complementary.

Explorer XX had provided useful data for the period from August 1964 to January 1966. The fixed-frequency sounder had yielded data on the fine structures of ionospheric irregularities and plasma resonances which are impossible to obtain with a swept-frequency sounder.

2.2.4 Alouette II (launched November 29, 1965)

Alouette II was launched in an orbit with perigee 502 km, apogee 2982 km and an inclination of 79.8° and a period of 121.4 min. The spin axis was orthogonal to the orbital plane. Alouette I was launched just prior to a period of sunspot minimum and was in an about 1000-km circular orbit; but Alouette II

was launched at a time of increasing solar activity. Under this condition the ionosphere was expanded and the maximum density in the ionosphere became greater, so a higher orbit was required and hence the frequency range of the sounder was extended (0.2 to 13.5 MHz). Reducing the lower frequency limit required in turn that the length of the longer sounder antenna be increased from 45.7 to 73.0 meters. The sweep rate was reduced to 0.125 MHz/sec below 2 MHz, in order that the plasma resonances and long-delayed echoes would be more readily observed and measured. Above 2 MHz, the frequency changes at a rate of 1 MHz/sec. The increased altitude at apogee meant that all transmitters had to be increased in power, while the pulse repetition frequency of the sounder had to be halved (30 Hz).

Alouette II and a sister satellite, Explorer XXXI, were launched into the same orbit by the same vehicle. The combined launch was named ISIS X. Explorer XXXI was built in the U.S.A. and contains temperature probes and an ion mass spectrometer. Comparison between the identical measurements on two satellites showed that the Alouette II structure would be satisfactory for direct sensing experiments. ISIS X achieved all of its scientific and technological objectives.

2.2.5 ISIS I (launched January 30, 1969)

The objectives of ISIS I were similar to those of ISIS X during a period of maximum and declining solar activity. The selected ISIS I orbit (3500 km apogee and 565 km perigee), therefore, was similar to that of the ISIS X satellites, but with an inclination of 88.40°. It was decided, however, that ISIS I would complete the most measurements of important ionospheric parameters with a single spacecraft instead of the two satellites required for the ISIS X mission. ISIS I basically had the same experiments as those of ISIS X. The swept-frequency sounder covers the frequency range 0.1 to 10 MHz in 16.6 sec, or an extended

range to 20 MHz in 26.6 sec. In addition, it had a fixed-frequency sounder similar to that of Explorer XX: the six fixed frequencies being 0.25, 0.48, 1.0, 1.95, 4.0, and 9.303 MHz.

Active spin rate and attitude controls were incorporated in the ISIS I spacecraft. Magnetic torquing techniques were used to control the spin rate within the range 1 to 3 rpm and to correct the spin-axis attitude (when necessary) at a rate of 3° per orbit.

Prior to 1986, ISIS I had been operated for over 17 years, and its longevity had exceeded the 10-year records of Alouettes I and II. ISIS I also provided data during the 1975–1976 sunspot minimum and participated in the IMS program (International Magnetospheric Study, January 1, 1976 to December 31, 1979). The ISIS I was the oldest of the 27 IMS satellites.

2.2.6 ISIS II (launched April 1, 1971)

ISIS II is the final and also the most complex satellite launched in the Alouette-ISIS program. The ISIS II mission stresses the study of latitudinal and diurnal variations of the topside ionosphere during a period of high solar activity. It was launched into a near-circular orbit at about 1400 km, (1429 apogee and 1358 perigee), with an inclination of 88.16° and an orbit period of 113.55 min.

Control of attitude and spin axis was done by means of magnetic torquing. The spin rate varies between about 2.5 and 3.5 rpm and can be changed by about 0.1 to 0.15 rpm per orbit. The spin axis is normally kept in the orbital plane (orbit aligned mode) or at right angles to the orbital plane (cartwheel mode). For the orbital aligned mode the attitude can be changed by $2.0° - 2.5°$ per orbit and in the cartwheel mode, by about 0.5° per orbit. This was done to provide ram and wake data for some experiments. The lengths of the two crossed-dipole antennas were 78.9 and 20.2 meters, respectively. The cross-over

frequency was 5 MHz.

The swept-frequency sounder operated between 0.1 and 20 MHz sampling every 14 or 21 sec and one of six fixed frequencies was also used for sounding for a few seconds during each 14- or 21-sec period. The pulses with approximately 100 μs in duration were repeated at the rate of 45 per second. The fixed-frequency sounder operated on six selected frequencies, which were 0.12, 0.48, 1.0, 1.95, 4.0, and 9.303 MHz.

The ISIS II mission was initiated during a period of declining solar activity and had continued through the subsequent 1975 – 1976 sunspot minimum. The ISIS II spacecraft has provided a unique and most comprehensive combination of experiments for ionospheric and magnetospheric studies.

2.2.7 Summary

The Alouette-ISIS program is the one of the earliest and one of the best examples of international cooperation in space research by the National Aeronautics and Space Administration (NASA). It has excellently completed all its scientific and technological objectives and provided a more complete understanding of the ionosphere and the magnetosphere. In particular, as a by-product of topside sounding, the new plasma resonances were observed. To the plasma physicist they could even be said to be of greater interest than the original purpose of the program.

2.3 Observations of Plasma Resonances or Waves Phenomena

Previous reviews (Chapman and Warren, 1968; Muldrew, 1972b; McAfee, 1973; Jackson *et al.*, 1980) have shown that topside sounder studies are of two general types: studies of the large and small scale structures of the ionosphere by means of reflected and scattered radio waves, and studies of the plasma resonance

phenomena of the ionospheric and magnetospheric magnetoplasma.

The swept-frequency sounders have provided a comprehensive representation of the large scale structure of the topside ionosphere up to a height 3000 km (including the densities and temperatures). They have also revealed the geographical location, time dependence and geomagnetic-field-aligned character of the small scale structure. The fixed-frequency sounders have even provided detailed measurements of small scale irregularities. Here we confine ourself to the plasma resonances and waves phenomena.

Since the topside sounders were located in the ionospheric and magnetospheric plasmas themselves, a number of plasma resonance phenomena were observed. What the plasma resonances indicate are that very strong signals are received at certain plasma characteristic frequencies and can persist from a fraction of one ms to over 30 ms after the termination of a 100 μs pulse. Plasma resonances in the ionosphere were first reported in rocket sounder experiments (Knecht *et al.*, 1961; Knecht and Russell, 1962), but it was not until the the first satellite sounder, Alouette I, that extensive observations became available.

From the results of over 30 years of plasma resonance observations from rocket- and satellite-borne topside sounders, the major resonances were observed at the electron plasma frequency f_N, the electron cyclotron frequency f_H, the upper hybrid frequency $f_T = (f_N^2 + f_H^2)^{1/2}$, the harmonics $2f_N$, $2f_T$ and nf_H with $n > 1$, and two series of resonances that occur between nf_H: the f_{Qn} resonances observed above f_T (at the maximum frequency of the Bernstein mode) and f_{Dn} resonances observed below f_T (called the diffuse resonances). Most resonances are interpreted by the reception of electrostatic waves stimulated by the sounder pulse. The electrostatic waves for the f_N, f_T and lower-order nf_H resonances propagate in the plasma, become reflected a short distance away and return to the satellite, producing a continuous receiver response following the transmitted pulse. The reflections for the f_N and f_T resonances are due to small changes in

electron density while for the lower-order nf_H to small changes in magnetic field strength. For the f_{Qn} and higher-order nf_H resonances the signal reception is due to the matching of a component of the wave group velocity to the satellite velocity. The above interpretation does not work for f_{Dn} resonances because the associated Bernstein electrostatic modes do not have a low group velocity in the frequency range below f_N except nf_H. The f_{Dn} resonances are due to waves generated by the ambient sounder-perturbed plasma. Several nonlinear mechanisms have been suggested for the interpretation of f_{Dn} resonances (Oya, 1971a; Benson, 1974 and 1982; Kiwamoto and Benson, 1979). Recently the f_{Dn} resonances were interpreted as force-free electromagnetic eigenmode oscillations of the system with cylindrical geometry (Osherovich, 1987 and 1989; Osherovich and Benson, 1991). The f_H resonance is less understood and $2f_N$ and $2f_T$ resonances are not understood yet.

All of the above resonances are related to electron plasma. In the interpretation of these resonances the motions of ions are ignored because of their large mass. Thus, they might be called the electron plasma resonances. There are, however, other phenomena observed on the Alouette-ISIS program, which are associated with ions (mainly protons). Three different proton effects have been observed:

(1) Graff (1967) reported an amplitude modulation with a period equal to the proton cyclotron period on the f_N resonance on the Alouette II ionogram.

(2) King and Preece (1967) reported spurs on the f_N resonance on the Alouette I ionogram which occur at time delays equal to multiples of the proton cyclotron period.

(3) Matuura and Nishizaki (1969) reported proton cyclotron echoes on Alouette II ionograms. The echoes occur on the ionograms at nearly constant apparent ranges which corresponds to the proton cyclotron period at the satellite position and mostly within the frequency range between f_H and f_N. Second,

third and higher-order multiple echoes are often associated with the fundamental one.

Following the reports of the discovery of these phenomena related to the proton cyclotron period, subsequent studies for spurs and proton cyclotron echoes have been done by Horita (1974, 1987), Benson (1975), Ondoh *et al.* (1975), Oya (1978), and Chen and Horita (1991). However these phenomena have not been investigated in as much detail as the electron plasma resonances. Many details and in particular, the generation mechanisms are still not understood. Further work needs to be done in order to obtain better understanding of them. This dissertation is devoted to studies of the proton cyclotron echoes.

Chapter 3

The Basic Theory of Waves in Hot Magnetoplasma

3.1 Introduction

One of the attractions of plasma wave theory is its common ground with so much of classical physics, ranging from the electrodynamics of charged particles through fluid mechanics to statistical mechanics. The plasma wave theory has been treated in many excellent textbooks, such as those by Stix (1962), Bekefi (1966), Clemmow and Dougherty (1969), Boyd and Sanderson (1969), Chen (1974) or more recently, Nicholson (1983), Jones *et al.* (1985), Swanson (1989), and Ichimaru (1992). This chapter is only intended as a reminder of the basic theory of plasma waves and as a convenient source of reference for subsequent use and, moreover, is restricted to waves in hot magnetoplasmas that will be studied in this dissertation.

Since the explanation for the major topside sounder resonance observations involves waves with both group and phase velocities small compared to the velocity of light, the cold plasma approximation is inadequate. Those particles whose velocities are near the phase velocity of the wave interact with the wave strongly. Thus the background motion of the particle must be considered. On the other hand, the earth's magnetic field has a very important influence on the motion of charged particles and the propagation of waves in the ionospheric and magnetospheric plasmas. Adding a magnetic field introduces a rich variety of new effects on waves and charged particles. So we must treat waves in a hot

plasma in a magnetic field. We assume that collisions of particles in the plasma are neglected, and the zero order magnetic field is uniform and constant. Hence the waves in the hot magnetoplasma should be treated by combining the Vlasov equation with the Maxwell equations.

3.2 The Main Equations

3.2.1 Maxwell's Equations

The behavior of the macroscopic electromagnetic fields in a plasma, as all physical media, is governed by Maxwell's equations. The Maxwell equations for the wave propagation in a plasma can be written in SI units as

$$\nabla \times \mathbf{E} = -\frac{\partial \mathbf{B}}{\partial t} \tag{3.1}$$

$$\nabla \times \mathbf{H} = \mathbf{J}_{ex} + \frac{\partial \mathbf{D}}{\partial t} \tag{3.2}$$

$$\nabla \cdot \mathbf{D} = \rho_{ex} \tag{3.3}$$

$$\nabla \cdot \mathbf{B} = 0 \tag{3.4}$$

with the equation

$$\frac{\partial \mathbf{D}}{\partial t} = \epsilon_0 \frac{\partial \mathbf{E}}{\partial t} + \mathbf{J} \tag{3.5}$$

and the constitutive relations

$$\mathbf{D} = \epsilon \cdot \mathbf{E} \tag{3.6}$$

$$\mathbf{B} = \mu \cdot \mathbf{H} \tag{3.7}$$

$$\mathbf{J} = \sigma \cdot \mathbf{E} \tag{3.8}$$

where

$\mathbf{E}$ = the electric field intensity

$\mathbf{H}$ = the magnetic field intensity

$\mathbf{D}$ = the electric flux density or the electric displacement vector

$\mathbf{B}$ = the magnetic flux density or magnetic induction

ρ = the electric charge density

ρ_{ex} = the external electric charge density

$\mathbf{J}$ = the electric current density

$\mathbf{J}_{ex}$ = the external electric current density

ϵ = the permittivity

ϵ_0 = the permittivity of free space

μ = the magnetic permeability

σ = the conductivity

The physical properties of the medium are manifested through ϵ, μ and σ. In an isotropic medium, they are all scalars, while in an anisotropic medium they may all become tensors. $\mathbf{J}_{ex}$ and ρ_{ex} can be applied from outside the plasma (e.g., in conductors surrounding the plasma, on grids inside the plasma etc.).

Eq. (3.5) and the relation $\epsilon = \epsilon_0 \mathbf{1} - \sigma/i\omega$ are required to be satisfied when the above Maxwell equations in a classical dielectric can be applied to wave motion in a plasma (as a kind of dielectric) (see Jones, Doucet and Buzzi, 1985).

The above constitutive relations are valid in wave-number-frequency domain. In the space-time domain the products in the equations become the convolution products, i.e.

$$\mathbf{D} = \epsilon * \mathbf{E} \tag{3.9}$$

$$\mathbf{B} = \mu * \mathbf{H} \tag{3.10}$$

$$\mathbf{J} = \sigma * \mathbf{E} \tag{3.11}$$

3.2.2 The Vlasov Equation

The single most important equation in space plasma physics is probably the Vlasov equation,

$$\frac{\partial f_j}{\partial t} + \mathbf{v} \cdot \frac{\partial f_j}{\partial \mathbf{r}} + \frac{q_j}{m_j}(\mathbf{E} + \mathbf{v} \times \mathbf{B}) \cdot \frac{\partial f_j}{\partial \mathbf{v}} = 0, \tag{3.12}$$

for each species, with

$$\rho = \sum_j n_j q_j \int f_j d\mathbf{v} \tag{3.13}$$

$$\mathbf{J} = \sum_j n_j q_j \int \mathbf{v} f_j d\mathbf{v} \tag{3.14}$$

as the sources, where f_j, q_j, m_j, n_j and $\mathbf{v}$ are the distribution function, charge, mass, number density and velocity vector for charged particle of type j.

The Vlasov equation is sometimes referred to as the collisionless Boltzmann equation, and the collisionless Boltzmann equation along with the Maxwell equations are called the Vlasov equations.

3.2.3 The Wave Equation

After Fourier transformation in both time and space, Equations (3.1) and (3.2), with $\mathbf{J}_{ex} = \rho_{ex} = 0$, combine to give the resulting wave equation in the form

$$\mathbf{n} \times (\mathbf{n} \times \mathbf{E}) + \mathbf{K} \cdot \mathbf{E} = 0 \tag{3.15}$$

where $\mathbf{n} = \mathbf{k}c/\omega$ has the magnitude of the refractive index and the direction of the propagation vector, and $\mathbf{K} = \mathbf{1} - \sigma/i\omega\epsilon_0$ may be called the equivalent dielectric tensor, where ϵ_0 is the permittivity of free space. The tensor $\epsilon = \epsilon_0\mathbf{K}$ is called the equivalent permittivity tensor. The electric displacement vector $\mathbf{D}$ can be written in wave number and frequency domains in terms of tensor $\mathbf{K}$ and ϵ as

$$\mathbf{D} = \epsilon \cdot \mathbf{E} = \epsilon_0 \mathbf{K} \cdot \mathbf{E} = \epsilon_0 \mathbf{E} - \mathbf{J}/i\omega \tag{3.16}$$

3.3 The Dispersion Relation of Waves in Hot Magnetoplasma

3.3.1 Solution of the Vlasov Equation

The technique we use is called the method of characteristics or integration over the unperturbed orbits. The idea is to find the perturbation of the distribution function due to the wave by integrating along the unperturbed trajectories.

Since the $\mathbf{E}$ and $\mathbf{B}$ depend on the distribution function $f(\mathbf{r},\mathbf{v},t)$, the Vlasov equation (3.12) is a nonlinear equation for $f(\mathbf{r},\mathbf{v},t)$, which is consequently difficult to solve. We now split the distribution function and the fields $\mathbf{E}$ and $\mathbf{B}$ into unperturbed and perturbed parts; i.e.,

$$f_j(\mathbf{r},\mathbf{v},t) = f_{j0}(\mathbf{r},\mathbf{v}) + f_{j1}(\mathbf{r},\mathbf{v},t) \tag{3.17}$$

$$\mathbf{E}(\mathbf{r},t) = 0 + \mathbf{E}_1(\mathbf{r},t) \tag{3.18}$$

$$\mathbf{B}(\mathbf{r},t) = \mathbf{B}_0(\mathbf{r}) + \mathbf{B}_1(\mathbf{r},t) \tag{3.19}$$

These quantities are substituted into the Vlasov equation (3.12) with assuming that the small second-order terms can be neglected and the unperturbed plasma is assumed to satisfy the Vlasov equation

$$\mathbf{v}\cdot\frac{\partial f_{j0}}{\partial \mathbf{r}} + \frac{q_j}{m_j}(\mathbf{v}\times\mathbf{B}_0)\cdot\frac{\partial f_{j0}}{\partial \mathbf{v}} = 0, \tag{3.20}$$

then we obtain the linearized Vlasov equation for the perturbed distribution function f_{j1},

$$\frac{\partial f_{j1}}{\partial t} + \mathbf{v}\cdot\frac{\partial f_{j1}}{\partial \mathbf{r}} + \frac{q_j}{m_j}(\mathbf{v}\times\mathbf{B}_0)\cdot\frac{\partial f_{j1}}{\partial \mathbf{v}} = -\frac{q_j}{m_j}(\mathbf{E}_1 + \mathbf{v}\times\mathbf{B}_1)\cdot\frac{\partial f_{j0}}{\partial \mathbf{v}} \tag{3.21}$$

Thus instead of calculating the exact distribution function f_j from the complete Vlasov equation, we calculate the perturbed distribution function f_{j1} which satisfies the linearized Vlasov equation in the study of small-amplitude waves.

The linearized Vlasov equation is an approximation to the exact equation, but is much easier to solve.

If we use

$$\frac{d\mathbf{r}}{dt} = \mathbf{v} \tag{3.22}$$

$$\frac{d\mathbf{v}}{dt} = \frac{q_j}{m_j}(\mathbf{v} \times \mathbf{B}_0) = \mathbf{a} \tag{3.23}$$

where $\mathbf{v}$ and $\mathbf{a}$ are the velocity and the acceleration of the charged particle of type j in the unperturbed field, then equation (3.21) may be written as

$$\frac{df_{j1}}{dt} = -\frac{q_j}{m_j}(\mathbf{E}_1 + \mathbf{v} \times \mathbf{B}_1)\frac{\partial f_{j0}}{\partial \mathbf{v}} \tag{3.24}$$

Integrating (3.24) along the unperturbed trajectory in $(\mathbf{r}, \mathbf{v}, t)$ space from $t' = -\infty$ to $t' = t$ gives

$$f_{j1}(\mathbf{r}, \mathbf{v}, t) = -\frac{q_j}{m_j}\int_{-\infty}^{t} dt' \left[\mathbf{E}_1(\mathbf{r}', t') + \mathbf{v}' \times \mathbf{B}_1(\mathbf{r}', t')\right] \cdot \frac{\partial f_{j0}(\mathbf{r}', \mathbf{v}')}{\partial \mathbf{v}'} \tag{3.25}$$

The choice of integral limits is valid for growing solutions, i.e. $f_{j1}(\mathbf{r}, \mathbf{v}, t) \to 0$ as $t \to -\infty$.

In order to integrate Eq. (3.25), we assume that the wave fields are of the form

$$\mathbf{E}_1 = \mathbf{E}e^{i(\mathbf{k}\cdot\mathbf{r}' - \omega t')} \tag{3.26}$$

$$\mathbf{B}_1 = \mathbf{B}e^{i(\mathbf{k}\cdot\mathbf{r}' - \omega t')} \tag{3.27}$$

and use Maxwell equation (3.1) to obtain

$$\mathbf{B}_1 = \frac{\mathbf{k} \times \mathbf{E}_1}{\omega} = \frac{\mathbf{k} \times \mathbf{E}}{\omega} e^{i(\mathbf{k}\cdot\mathbf{r}' - \omega t')} \tag{3.28}$$

Thus (3.25) may be written as

$$f_{j1}(\mathbf{r}, \mathbf{v}, t) = -\frac{q_j}{m_j}\int_{-\infty}^{t} dt' \mathbf{E}\left[1 + \frac{\cdot\mathbf{v}'\mathbf{k} - \mathbf{v}' \cdot \mathbf{k}}{\omega}\right] \cdot \frac{\partial f_{j0}(\mathbf{r}', \mathbf{v}')}{\partial \mathbf{v}'} e^{i(\mathbf{k}\cdot\mathbf{r}' - \omega t')} \tag{3.29}$$

The integrand in (3.29) is evaluated along the unperturbed trajectory, $\mathbf{r}'(t')$. The end point of the trajectory is $\mathbf{r}' = \mathbf{r}$ at $t' = t$. For the case considered

($\mathbf{E}_0 = 0$, $\mathbf{B}_0 = B_0\hat{\mathbf{z}}$), the trajectory is a helix, which is governed by the equation of motion for the particle.

$$\frac{d\mathbf{v}'}{dt} = \xi_j \mathbf{v}' \times \omega_{cj}\hat{\mathbf{z}} \tag{3.30}$$

where

$$\omega_{cj} = \left|\frac{q_j \mathbf{B}_0}{m_j}\right| \tag{3.31}$$

and $\xi_j = q_j/|q_j|$. The solution of (3.30) that reaches $\mathbf{v}' = \mathbf{v}$ at $t' = t$ is

$$\begin{aligned} v'_x &= v_x cos\omega_{cj}\tau - \xi_j v_y sin\omega_{cj}\tau \\ v'_y &= \xi_j v_x sin\omega_{cj}\tau + v_y cos\omega_{cj}\tau \\ v'_z &= v_z \end{aligned} \tag{3.32}$$

where $\tau = t - t'$. Integrating these gives the unperturbed trajectory that ends at $\mathbf{r}' = \mathbf{r}$ as $t' = t$

$$\begin{aligned} x' &= x - \frac{v_x}{\omega_{cj}} sin\omega_{cj}\tau + \xi_j \frac{v_y}{\omega_{cj}}(1 - cos\omega_{cj}\tau) \\ y' &= y - \xi_j \frac{v_x}{\omega_{cj}}(1 - cos\omega_{cj}\tau) - \frac{v_y}{\omega_{cj}} sin\omega_{cj}\tau \\ z' &= z - v_z\tau. \end{aligned} \tag{3.33}$$

In order to integrate (3.29), we also need to make assumptions about the form of the unperturbed distribution function. Suppose a distribution function f_j is constructed from functions $C_i(\mathbf{x}, \mathbf{v}, t)$ that are constants of the motion along the trajectory of a particle, then we may have

$$\frac{d}{dt} f_j([C_i(\mathbf{x}, \mathbf{v}, t)]) = \sum_i \frac{\partial f_j}{\partial C_i}\frac{d}{dt} C_i = 0 \tag{3.34}$$

and so the Vlasov equation is satisfied. Thus, any distribution that is a function only of the constants of the motion of the individual particle trajectories is a solution of the Vlasov equation. In the case considered, the constants of the motion are the momentum mv_z in the $\hat{\mathbf{z}}$-direction and the energy $mv_\perp^2/2 =$

$m(v_x^2 + v_y^2)/2$ in the plane perpendicular to $\mathbf{B}_0$. Thus any function

$$f_{j0} = f_{j0}(\frac{v_x^2 + v_y^2}{2}, v_z) \tag{3.35}$$

is an equilibrium solution to the Vlasov equation in the presence of a uniform magnetic field and we have the relation

$$f_{j0}(\frac{v_x'^2 + v_y'^2}{2}, v_z') = f_{j0}(\frac{v_x^2 + v_y^2}{2}, v_z) \tag{3.36}$$

Hence it is quite reasonable to choose a Maxwellian across $\mathbf{B}_0$ and a shifted Maxwellian along $\mathbf{B}_0$ as the unperturbed distribution function

$$\begin{aligned} f_{j0} &= f_{j0}(\frac{v_x^2 + v_y^2}{2}, v_z) \\ &= \frac{m}{2\pi\kappa T_\perp}\left(\frac{m}{2\pi\kappa T_\parallel}\right)^{1/2} exp\left[-\frac{m(v_x^2 + v_y^2)}{\kappa T_\perp} - \frac{m(v_z - V_z)}{\kappa T_\parallel}\right] \end{aligned} \tag{3.37}$$

where T denotes the temperature and $\parallel$ and $\perp$ refer to along and across the unperturbed magnetic field; κ is the Boltzmann constant and V_z is a drift velocity in the z direction.

After completing the variable change from primed to unprimed coordinates, (3.29) can be written in the form

$$f_{j1}(\mathbf{r}, \mathbf{v}, t) = -\frac{q_j}{m_j}\int_{-\infty}^{t} dt'(\cdots) = -e^{i(\mathbf{k}\cdot\mathbf{r} - \omega t)}\frac{q_j}{m_j}\int_0^{\infty} d\tau(\cdots) \tag{3.38}$$

It is interesting that $\mathbf{r}$ and t can be taken out of the integral, and enter only as the phase factor. We suppress this phase factor and can consider f_{j1} as the Fourier transform $f_{j1}(\mathbf{k}, \omega, \mathbf{v})$. So the integral is now over the variable τ with limits from 0 to ∞.

When calculations of f_{j1} and its moments are completed, the current density and the mobility tensor, and hence the equivalent dielectric tensor can be calculated. However, the algebra for these calculations is horrendous and therefore we miss out much of the algebraic detail to avoid being cluttered for our purposes, and also excellent references exist already (for example, Stix, 1962; Swanson, 1989). We concentrate only on the essential features of calculations.

3.3.2 Calculations for Mobility tensor $\mathbf{M}^j$ and Dielectric Tensor K

The current density **J** may be given in terms of the perturbed distribution function f_{j1}

$$\mathbf{J} = \sum_j n_j q_j \int \mathbf{v} f_{j1} d^3v = \sum_j n_j q_j \langle \mathbf{v}^j \rangle \tag{3.39}$$

and we may define the mobility tensor $\mathbf{M}^j$ in dimensionless units for each type of particle by the relation

$$\langle \mathbf{v}^j \rangle = \int\int\int \mathbf{v} f_1 dv_x dv_y dv_z = \frac{\mathbf{M}^j \cdot \mathbf{E}}{B_0} \tag{3.40}$$

With choosing $k_y = 0$, the components of $\mathbf{M}^j$ have been calculated (from Equation 9.8, page 188, Stix, 1962, and note that the subscript and superscript j have been dropped and that $\xi_j = q_j/|q_j|$),

$$\begin{aligned}
M_{xx} &= -\frac{\omega_c \xi e^{-\lambda} \kappa T_\perp}{m k_z} \sum_{n=-\infty}^{\infty} \frac{n^2}{\lambda} I_n [\langle \Theta \rangle_n] \\
M_{xy} &= -\frac{\omega_c e^{-\lambda} \kappa T_\perp}{m k_z} \sum_{n=-\infty}^{\infty} in(I_n - I_n')[\langle \Theta \rangle_n] \\
M_{xz} &= -\frac{\xi e^{-\lambda} \kappa T_\perp}{m k_z} \sum_{n=-\infty}^{\infty} \frac{n k_x}{\lambda} I_n [n\langle \Phi \rangle_n - \langle \Psi \rangle_n] \\
M_{yx} &= \frac{\omega_c e^{-\lambda} \kappa T_\perp}{m k_z} \sum_{n=-\infty}^{\infty} in(I_n - I_n')[\langle \Theta \rangle_n] \\
M_{yy} &= -\frac{\omega_c \xi e^{-\lambda} \kappa T_\perp}{m k_z} \sum_{n=-\infty}^{\infty} \left(\frac{n^2}{\lambda} I_n + 2\lambda I_n - 2\lambda I_n' \right) [\langle \Theta \rangle_n] \\
M_{yz} &= \frac{e^{-\lambda} \kappa T_\perp}{m k_z} \sum_{n=-\infty}^{\infty} ik_x (I_n - I_n')[n\langle \Phi \rangle_n - \langle \Psi \rangle_n] \\
M_{zx} &= \frac{\xi e^{-\lambda} \kappa T_\perp}{m k_z} \sum_{n=-\infty}^{\infty} \frac{n k_x}{\lambda} I_n [\langle v_z \Theta \rangle_n] \\
M_{zy} &= \frac{e^{-\lambda} \kappa T_\perp}{m k_z} \sum_{n=-\infty}^{\infty} ik_x (I_n - I_n')[< v_z \Theta >_n] \\
M_{zz} &= \frac{\omega \xi e^{-\lambda}}{k_z} \sum_{n=-\infty}^{\infty} I_n [n\langle v_z \Phi \rangle_n - \langle v_z \Psi \rangle_n]
\end{aligned} \tag{3.41}$$

where

$$\langle\Theta\rangle_n = \frac{2}{\omega T_\perp}\left(\frac{m}{2\kappa T_\parallel}\right)^{3/2}\left\{ik_z\left(\frac{2\kappa T_\parallel}{m}\right)^{1/2}(T_\perp - T_\parallel) - [(\omega - k_z V_z + n\omega_c)T_\perp - n\omega_c T_\parallel]F_0\right\} \tag{3.42}$$

$$\langle v_z\Theta\rangle_n = \frac{2}{k_z\omega T_\perp}\left(\frac{m}{2\kappa T_\parallel}\right)^{3/2}\left\{ik_z\left(\frac{2\kappa T_\parallel}{m}\right)^{1/2}[(\omega + n\omega_c)T_\perp - (k_z V_z + n\omega_c)T_\parallel] - (\omega + n\omega_c)[(\omega - k_z V_z + n\omega_c)T_\perp - n\omega_c T_\parallel]F_0\right\} \tag{3.43}$$

$$\langle\Phi\rangle_n = \frac{2\omega_c}{k_z\omega T_\perp}\left(\frac{m}{2\kappa T_\parallel}\right)^{3/2}\left\{ik_z\left(\frac{2\kappa T_\parallel}{m}\right)^{1/2}(-T_\perp + T_\parallel) + [(\omega - k_z V_z + n\omega_c)T_\perp - (\omega + n\omega_c)T_\parallel]F_0\right\} \tag{3.44}$$

$$\langle v_z\Phi\rangle_n = \frac{2\omega_c}{k_z^2\omega T_\perp}\left(\frac{m}{2\kappa T_\parallel}\right)^{3/2}\left\{ik_z\left(\frac{2\kappa T_\parallel}{m}\right)^{1/2} [(-\omega - n\omega_c)T_\perp + (\omega + k_z V_z + n\omega_c)T_\parallel)] + (\omega + n\omega_c)[(\omega - k_z V_z + n\omega_c)T_\perp - (\omega + n\omega_c)T_\parallel]F_0\right\} \tag{3.45}$$

$$\langle\Psi\rangle_n = \frac{2}{k_z}\left(\frac{m}{2\kappa T_\parallel}\right)^{3/2}\left\{ik_z\left(\frac{2\kappa T_\parallel}{m}\right)^{1/2} - (\omega - k_z V_z + n\omega_c)F_0\right\} \tag{3.46}$$

$$\langle v_z\Psi\rangle_n = \frac{2}{k_z^2}\left(\frac{m}{2\kappa T_\parallel}\right)^{3/2}\left\{ik_z\left(\frac{2\kappa T_\parallel}{m}\right)^{1/2}(\omega + n\omega) - (\omega + n\omega_c)(\omega - k_z V_z + n\omega_c)F_0\right\} \tag{3.47}$$

$$F_0(\alpha_n) = \sqrt{\pi}\frac{k_z}{|k_z|}exp(-\alpha_n^2) + 2iS(\alpha_n) \tag{3.48}$$

$$S(z) = exp(-z^2)\int_0^z exp(t^2)dt \tag{3.49}$$

$$\alpha_n = \frac{\omega - k_z V_z + n\omega_c}{k_z}\left(\frac{m}{2\kappa T_\parallel}\right)^{1/2} \tag{3.50}$$

$$\lambda = \frac{k_x^2\kappa T_\perp}{\omega_c^2 m} = \frac{1}{2}k_x^2\rho_L^2 \tag{3.51}$$

$$\rho_L = \frac{v_t}{\omega_c} \tag{3.52}$$

$$v_t = \sqrt{\frac{2\kappa T_\perp}{m}} \tag{3.53}$$

$$I_n(\lambda) = \sum_{l=0}^{\infty} \frac{1}{l!(n+l)!}\left(\frac{\lambda}{2}\right)^{n+2l} \tag{3.54}$$

In the above expressions, ρ_L is the Larmor radius of gyration, v_t is the transverse thermal speed, and I_n is the modified Bessel function of the first kind. We note that we may have

$$n\langle\Phi\rangle_n - \langle\Psi\rangle_n = -\langle v_z\Theta\rangle_n - \frac{ik_zV_z}{\omega}\left(\frac{m}{\kappa T_\perp}\right) \tag{3.55}$$

Combining (3.40), (3.39) and (3.16) gives the equivalent dielectric tensor

$$\mathbf{K} = \mathbf{1} + i\sum_j \frac{\xi_j\omega_{pj}^2}{\omega\omega_{cj}}\mathbf{M}^j \tag{3.56}$$

where **1** is the unit dyad and ω_{pj} the plasma frequency for type j particle.

3.3.3 Dispersion Relation of Plasma Waves

The vector wave equation (3.15), when $k_y = 0$, can take in matrix form

$$\begin{pmatrix} -n_z^2 + K_{xx} & K_{xy} & n_xn_z + Kxz \\ K_{yx} & -n_x^2 - n_z^2 + K_{yy} & K_{yz} \\ n_xn_z + K_{zx} & K_{zy} & -n_x^2 + K_{zz} \end{pmatrix}\begin{pmatrix} E_x \\ E_y \\ E_z \end{pmatrix} = 0. \tag{3.57}$$

This is a linear homogeneous equation. The condition for a non-zero solution is that the determinant of coefficients must vanish. This condition gives the dispersion relation of plasma waves,

$$\begin{vmatrix} -n_z^2 + K_{xx} & K_{xy} & n_xn_z + Kxz \\ K_{yx} & -n_x^2 - n_z^2 + K_{yy} & K_{yz} \\ n_xn_z + K_{zx} & K_{zy} & -n_x^2 + K_{zz} \end{vmatrix} = 0 \tag{3.58}$$

3.3.4 Dispersion Relation of Electrostatic Waves

If the oscillating magnetic field of a wave is zero, the wave is called the electrostatic wave; otherwise it is the electromagnetic wave. For electrostatic waves,

we have

$$\nabla \times \mathbf{E} = -\frac{\partial \mathbf{B}}{\partial t} = 0 \tag{3.59}$$

and hence we may represent the electric field by a scalar potential

$$\mathbf{E} = -\nabla\phi = -i\mathbf{k}\phi \tag{3.60}$$

so that **E** is parallel to **k** and the electrostatic waves are longitudinal waves.

Taking the scalar product of **n** into Equation 3.15 from the left, we obtain

$$\mathbf{n} \cdot \mathbf{K} \cdot \mathbf{E} = \mathbf{n} \cdot \mathbf{K} \cdot (\mathbf{n}\frac{E}{n}) = 0 \tag{3.61}$$

which leads to the dispersion relation for electrostatic waves (with assumption of $E/n \neq 0$),

$$\mathbf{n} \cdot \mathbf{K} \cdot \mathbf{n} = 0 \tag{3.62}$$

When we take $V_z = 0$ in Equation (3.55), we may have $M_{xz} = M_{zx}$ and hence $K_{xz} = K_{zx}$ so that Equation (3.62) can be reduced to the form, with $k_y = 0$

$$k_x^2 K_{xx} + 2k_x k_z K_{xz} + k_z^2 K_{zz} = 0 \tag{3.63}$$

Computing the necessary elements of the equivalent dieletric tensor needed in (3.63) by Eqs. (3.56) and putting them into (3.63), one finds

$$\begin{aligned} k_x^2 + k_z^2 + \sum_j \frac{\omega_{pj}^2 m_j e^{-\lambda_j}}{\kappa T_{\|}} \sum_{n=-\infty}^{\infty} I_n(\lambda_j) \Bigg\{ 1 + \\ i \left[\alpha_{nj} - \frac{n\omega_{cj}}{k_z} \left(\frac{m_j}{2\kappa T_{\|}} \right)^{1/2} \frac{T_{\|}}{T_{\perp}} \right] F_0(\alpha_{nj}) \Bigg\} \quad = \quad 0 \end{aligned} \tag{3.64}$$

where

$$\alpha_{nj} = \frac{\omega + n\omega_{cj}}{k_z} \left(\frac{m_j}{2\kappa T_{\|}} \right)^{1/2} \tag{3.65}$$

Equation (3.64) is similar to the formula given by Stix (9.103, p.225, 1962). Eq. (3.64) is the complete electrostatic wave dispersion relation in a hot magnetoplasma.

3.4 Summary

In this chapter, we have reviewed the basic theory of waves in the hot magnetoplasma. The main equations, e.g., the Maxwell equations, the Vlasov equation and the wave equation were presented. After the linearized Vlasov equation was solved by the method of characteristics, we calculated the mobility and the equivalent dielectric tensors. Inserting the values of the equivalent dielectric tensor into the wave equation, we obtained the dispersion relation of full waves, and the dispersion relation of electrostatic waves. Since the wave equation is too complicated to solve, discussions of the dispersion relations of waves, especially electrostatic waves, in explanations of the plasma resonance phenomena observed in topside sounding of the ionosphere are very important. The theoretical work in this dissertation is based on these kinds of discussion.

Chapter 4

Observations of the Proton Cyclotron Echoes on Fixed-Frequency Ionograms

4.1 Introduction

Proton cyclotron echoes were first reported by Matuura and Nishizaki (1969) on Alouette II satellite ionograms. They found that the echoes occur at a nearly constant apparent range with respect to the swept frequency and the time delay between the transmission of the sounder pulse and the reception of signal at the satellite is equal to the proton cyclotron period at the satellite position, deduced from the observed electron cyclotron frequency. This phenomenon appears as a very thin, horizontal trace on the ionograms usually between the plasma frequency f_N and the electron cyclotron frequency f_H at the satellite but sometimes below f_H. The proton cyclotron echoes are observed at all altitudes over the altitude range of the Alouette II satellite and more frequently near the geomagnetic equator. Second, third and up to the fifth order multiple echoes associated with the fundamental echo are often present.

Horita (1974) scaled Alouette II, ISIS I and ISIS II ionograms for about sixty satellite passes to study the characteristics of proton cyclotron echoes and spurs (the spur is another phenomenon related to the proton cyclotron period first discovered on the Alouette I ionograms by King and Preece (1967)). He confirmed the previous observations by Matuura and Nishizaki that the proton cyclotron echoes occur on the ionograms at frequencies below the electron plasma

frequency f_N and predominantly slightly above the electron cyclotron frequency f_H. He also found that the echoes were observed most often when nf_H (n=1, 2, 3, 4) was approximately equal to one of the other characteristic frequencies, that is: $nf_H \approx f_N$, $nf_H \approx f_zS$ and $nf_H \approx f_T$, where f_H, f_N, f_T and f_zS are the electron cyclotron, electron plasma, upper hybrid resonance frequencies and the cut-off frequency of the Z-wave at the height of the satellite, respectively.

Improvements in the design of the VLF experiment aboard the ISIS II satellite (Daniels, 1971; Jackson, 1986) made possible the detection of VLF signals which were stimulated by the high-power pulses of the topside sounding transmitter. Previous Alouette and ISIS satellites did not detect such signals because the operation of their high-powered HF transmitters produced a reduction in the gain of the VLF receivers (Florida, 1969). Palmer and Barrington (1973) described and discussed VLF emissions observed by the ISIS II VLF receiver, that were stimulated by the high-power pulses of the topside sounder. They had observed a damped oscillation near the lower hybrid resonance frequency with a superimposed pulse modulation separated by the proton cyclotron period, following a single sounder pulse. Ondoh *et al.* (1975) observed proton cyclotron emissions and their higher harmonics by the VLF receiver on the ISIS II satellite, which occurred at the same time as the proton cyclotron echoes on an ISIS II swept-frequency ionogram.

Horita (1987) examined over 1000 ionograms from Alouette II and ISIS II exhibiting proton cyclotron echoes and spurs, and made a classification system. The major classification is echoes only, spurs only and spur-echo combinations. The subclassification for echoes only includes a plus, zero, or minus sign to indicate if the observed proton cyclotron period is greater than, equal to, or less than the calculated proton cyclotron period in vicinity of the satellite from the electron cyclotron resonance frequency. Also the letters U and D indicate whether the echo trace curves up (to lower apparent ranges) or down (to higher

apparent ranges) as it approaches a resonance spike from the high-frequency side, indicated by HS, or the lower-frequency side, indicated by LS. One of the interesting features is an absence of echo minus.

Oya (1978) presented a theory for the generation mechanism of proton cyclotron echoes. The theory is based on the nonlinear wave-particle interaction. The RF pulse from the transmitter stimulates an electrostatic electron cyclotron wave in the ambient plasma and, at the same time, produces a proton concentration surrounding the antenna. The electrostatic electron cyclotron wave produces a fast electron stream in opposite directions with respect to the wave propagation direction due to damping of the wave. The bunched protons in the proton concentration area repeat their motions in the earth's magnetic field with the proton cyclotron period and produce a pseudo-wave of the electric field. The interaction of the pseudo-wave with the electron stream produces the observed proton cyclotron echoes.

Oya's theory is consistent with the observation that the apparent range of the echo is always greater than the theoretical apparent range, i.e., no echo minus. However, it excludes observations of proton cyclotron echoes at high geomagnetic latitudes. A proton cyclotron echo at a geomagnetic latitude of $59.7°N$ has been already observed in apparent contradiction to the theory (Horita, 1987).

All of the above studies were done, based on ionograms from swept-frequency observations. In the swept-frequency observations the sounding frequency is gradually increased so that each pulse is slightly higher in frequency than the preceding pulse. The ionograms produced by these observations show the delay of the received signals as a function of frequency under nearly constant plasma conditions. However, there is another type of observation, the fixed-frequency observations. The fixed-frequency observations use only a few fixed frequencies and process the data from each one separately. The ionograms produced by these observations show the delay as a function of the varying plasma conditions

encountered by the satellite. Such ionograms are useful in studying the fine structure of the resonances. The fixed-frequency observations have been used on the satellites Explorer XX, ISIS I and ISIS II. The ISIS I and II satellites have the capability to combine the advantages of the fixed-frequency mode used by Explorer XX with the swept-frequency mode used by Alouette I and II.

This chapter will present the proton cyclotron echoes on the fixed-frequency observations obtained from ISIS I. The ionograms were recorded at the ground station in Ouagadougou, Upper Volta (ODG, 12.7°S, 1.2°W). The fixed-frequency ionograms provide some information for proton cyclotron echoes not available on the swept-frequency observations.

4.2 Observations

Figure 4.1 is a combined fixed-frequency (left portion) and swept-frequency (right portion) ionogram observed with the ISIS I satellite. ISIS I operated at six fixed frequencies: 0.25, 0.48, 1.00, 1.95, 4.00 and 9.303 MHz in the fixed-frequency mode and at a frequency range from 0.1 to 20 MHz in the swept-frequency mode. A continuum of frequency between 0.1 and 20 MHz was sampled once every 19 or 29 sec, and one of six selected frequencies was used for a period of 3 to 5 sec during this 19- or 29-sec period.

An ionogram consists of closely spaced lines the darkness of which corresponds to the received signal strength. The distance downward from the top of the diagram indicates the time delay of the received signal after the transmission of each sounding pulse or the apparent range of the reflection point of the pulse. The lines for subsequent pulses are placed side-by-side in ionogram. The horizontal axis for the swept-frequency mode is the sounding frequency, increasing to the right; however, the horizontal axis for the fixed-frequency mode becomes the time of the sounding or, equivalently, the geographic position of the satellite.

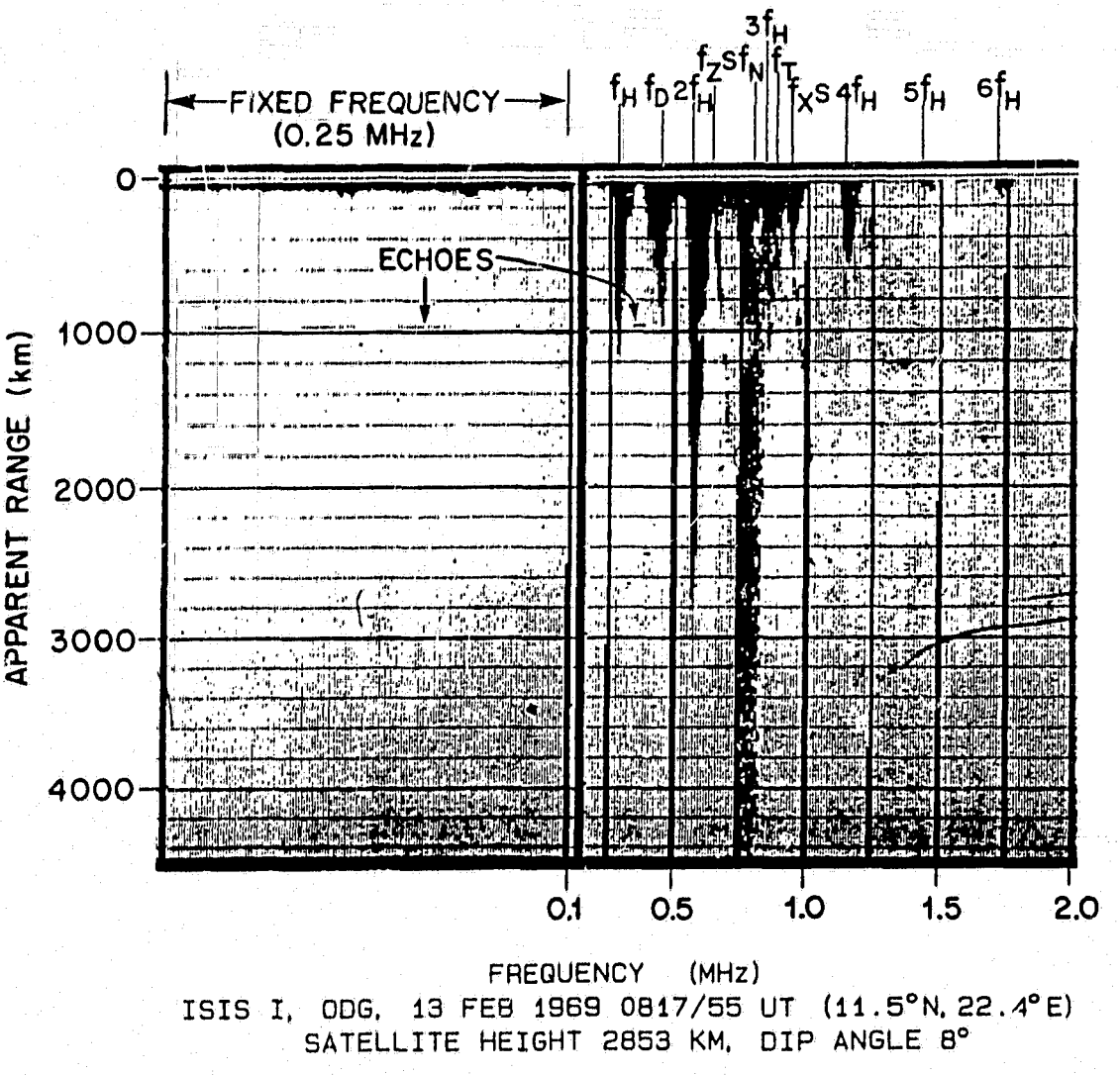

Figure 4.1: ISIS I combined fixed-frequency (0.25 MHz) (left portion) and swept-frequency ionogram (right portion) illustrating proton cyclotron echoes on both modes.

Figure 4.1 was taken on February 13, 1969 at 0817:55 UT when the satellite was located at $11.5°N$ and $22.4°E$ geographic coordinates, and at an altitude 2853 km. The dip angle was 8°. The sounder operated at 0.25 MHz during the fixed frequency portion of the ionogram.

The swept-frequency portion of the ionogram, beginning at 0.1 MHz to the right, shows the resonances at the electron cyclotron frequency f_H and its harmonics nf_H ($n > 1$, integer), the plasma frequency f_N, the upper hybrid frequency f_T, and the diffuse resonance f_D, which occurs below f_T and between nf_H with $n \geq 1$. These resonances have been studied by many authors (e.g., Muldrew, 1972b; Benson, 1977). Oya (1970) introduced the notation f_{Dn} for a sequence of diffuse resonances. The f_{Dn} resonances include f_D resonance and f_{D1} corresponds to f_D. The swept-frequency portion also shows the cutoffs f_zS for Z-wave, f_xS for X-wave and $f_oS \equiv f_N$ for O-wave, where S signifies the satellite height. The cutoffs are the lowest frequencies for which waves of a particular mode (Z, O, and X) can propagate and the refractive index for that mode is zero at the cutoffs.

The proton cyclotron echo occurs on the fixed frequency portion of the ionogram as a horizontal trace at about 973 km apparent range. It occurs at constant apparent range on the fixed-frequency mode but its intensity appears to be modulated. The constant apparent range corresponds to the proton cyclotron period at the satellite position, which may be deduced from the observed electron cyclotron frequency on the swept-frequency mode. Since the sounding frequency is fixed, a proton cyclotron echo is observed as the sounder passes through a region where the plasma parameters are appropriate. Thus it may be under observation for a long time. The proton cyclotron echo in this example occurs during the whole fixed-frequency observation period (about 5 sec). The proton cyclotron echo also occurs on the swept-frequency portion of the ionogram at about 965 km apparent range between the resonances f_H and f_D as a short

trace due to the change of the sounding frequency. The echo shows some curvature (Horita, 1987). This kind of proton cyclotron echoes has been observed and studied previously. We note that the proton cyclotron echo on the swept-frequency mode occurs at a frequency range between 0.34 and 0.39 MHz which is above the selected fixed frequency 0.25 MHz.

Figure 4.2 shows another combined fixed-frequency and swept-frequency ionogram, showing the proton cyclotron echo on the fixed-frequency observation. This ionogram was taken on February 19, 1969 at 0743:28 UT when the satellite was located at $13.0°N$ and $24.5°E$ geographic coordinates, and at an altitude of 2515 km. The dip angle was 10°. The sounder was operated at 0.25 MHz during the fixed frequency portion of the ionogram.

This figure is similar to Figure 4.1. However, the proton cyclotron echoes on both modes of the ionogram occur at a constant apparent range of about 838 km. The proton cyclotron echo on the swept-frequency portion of the ionogram is observed at the RF range between 0.1 and 0.47 MHz and no curvature occurs for it. A second multiple is observed at the RF range between 0.39 and 0.47 MHz.

A basic feature shown by the above two combined ionograms is that the proton cyclotron echoes on the fixed-frequency mode occur at the constant apparent ranges. The constant apparent range indicates that plasma parameters encountered by the satellite, such as magnetic field, electron and ion densities, electron and ion temperatures are smooth and nearly constant.

Figure 4.3 was taken on February 10, 1969 at 1138:05 UT when the satellite was located at $9.8°S$ and $25.1°W$ geographic coordinates, and at an altitude 3376 km. The dip angle was $-10°$.

The apparent range on the fixed-frequency mode in this figure is subject to a smooth change. The apparent range increases from 1344 km at the beginning of the observation to 1389 km and then decreases to 1372 km at the end of the

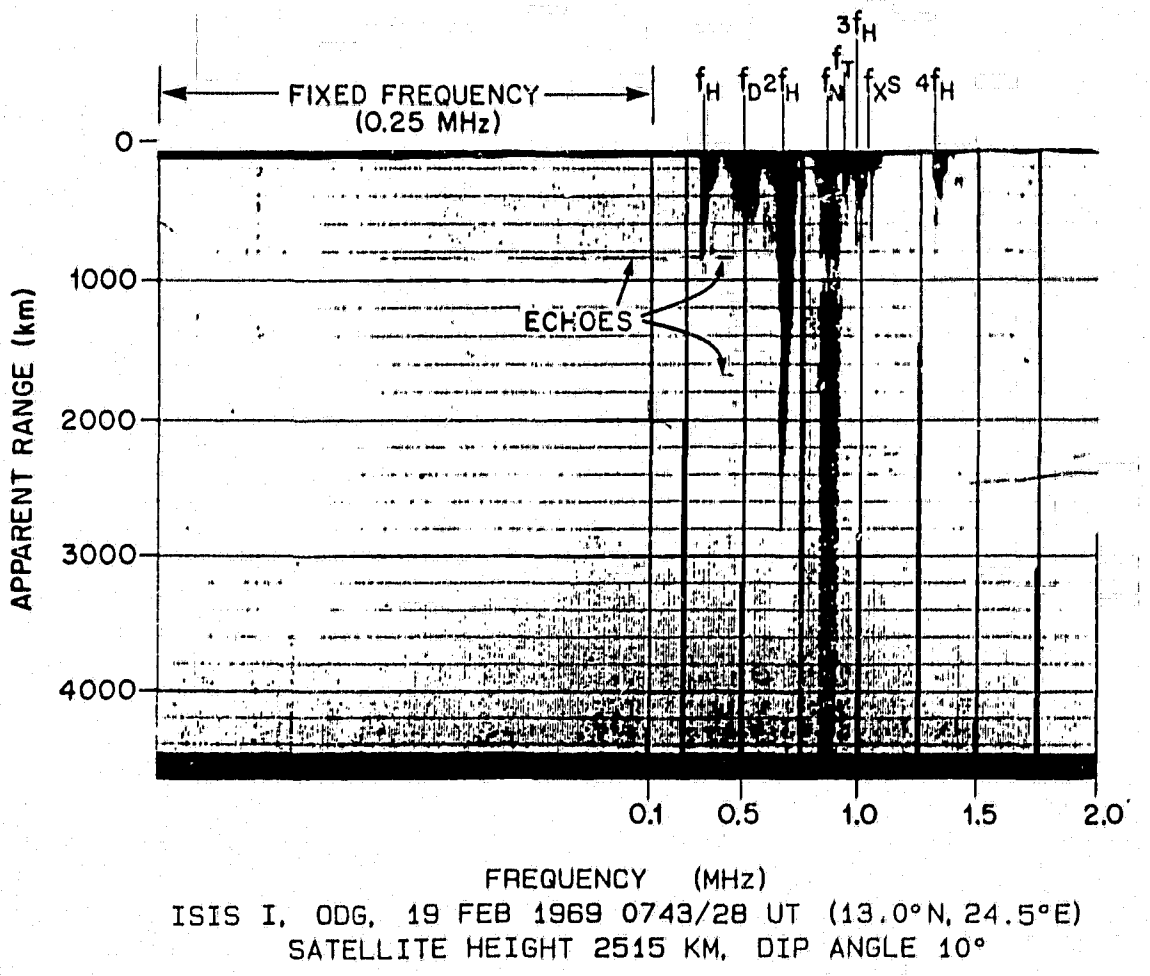

Figure 4.2: ISIS I combined fixed-frequency (0.25 MHz) (*left portion*) and swept-frequency ionogram (right portion) illustrating proton cyclotron echoes on both modes and a second multiple echo associated with the fundamental echo on the swept-frequency mode.

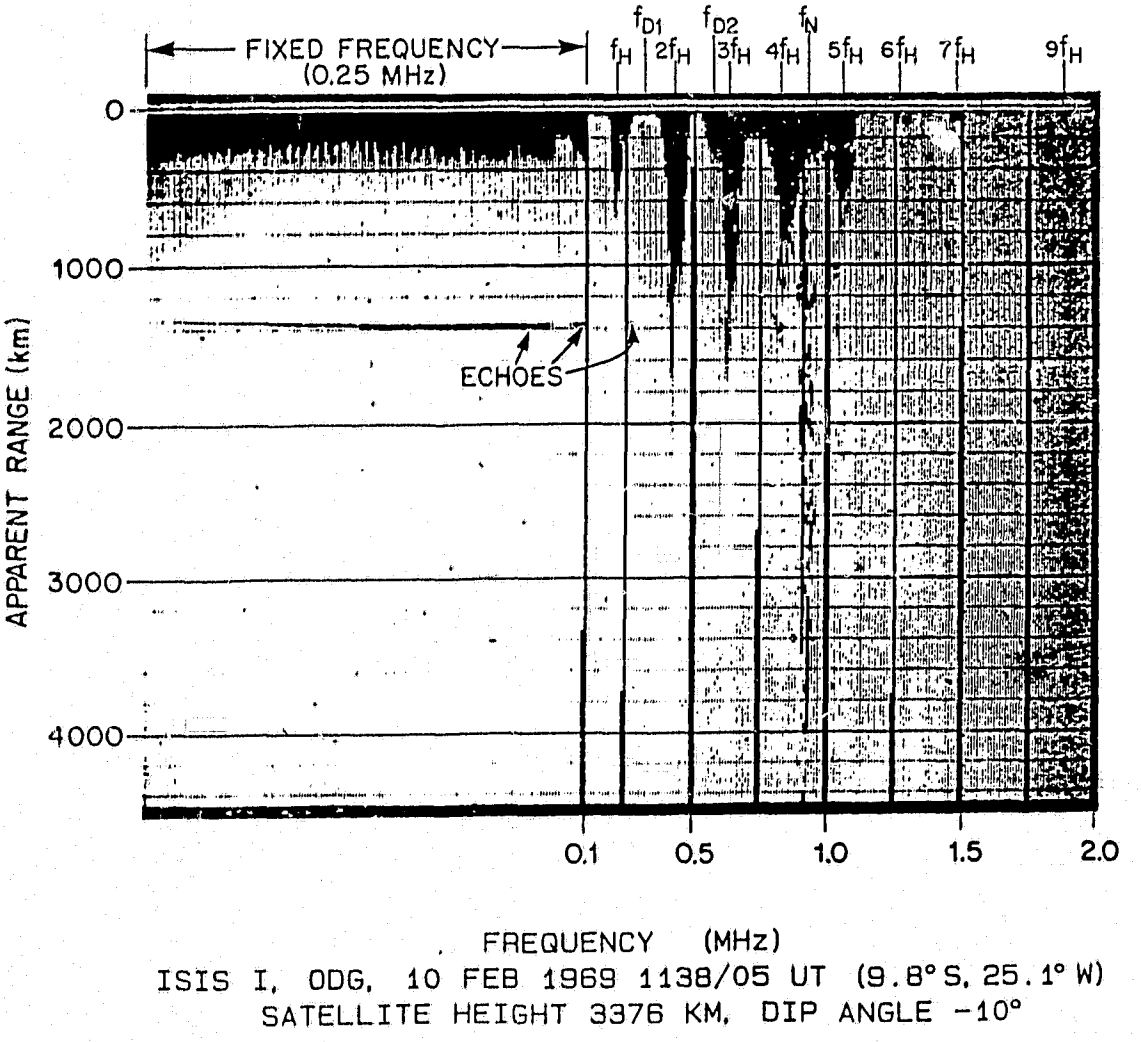

Figure 4.3: ISIS I combined fixed-frequency (0.25 MHz) (left portion) and swept-frequency ionogram (right portion) illustrating proton cyclotron echoes on both modes and the non-constant apparent range on the fixed-frequency mode.

fixed-frequency mode observation. Figure 4.4 shows a similar case. However, the apparent range increases from 1315 km to 1365 km and stays there till the end of the fixed-frequency mode observation. This ionogram was obtained 30 sec later from the former. The proton cyclotron echoes on the swept-frequency mode in both figures occur at a RF range very close to but above the selected fixed-frequency (0.25 MHz). The echoes show curvatures.

Matuura and Nishizaki (1969) had pointed out in their paper first reporting observation of the proton cyclotron echoes that second, third and higher order multiple echoes were often associated with the fundamental echo. This statement is also true for the fixed-frequency mode observation.

Figure 4.5 was taken on February 10, 1969 at 1135:38 UT when the satellite was located at $14.8°S$ and $24.4°W$ geographic coordinates, and at an altitude 3438 km. The dip angle was 17°. This ionogram shows that the fundamental proton cyclotron echo and its second multiple echo occurs on the fixed-frequency mode. Both apparent ranges are subject to the changes. However, this time they first decrease, arrive at their minimum values and then increase. Similar features are also shown in Figure 4.6. The ionogram in Figure 4.6 was taken on February 9, 1969 at 1203:08 UT when the satellite was located at $14.0°S$ and $30.4°W$ geographic coordinates, and at an altitude of 3449 km. The dip angle was $-14°$.

4.3 Summary

The combined fixed-frequency and swept-frequency ionograms obtained from ISIS I at the ground station Ouagadougou (ODG), Upper Volta, have been examined. The proton cyclotron echoes on the fixed-frequency mode have been observed. In addition to the features, such as constant apparent range and higher order multiple echoes, which occur on the swept-frequency observations

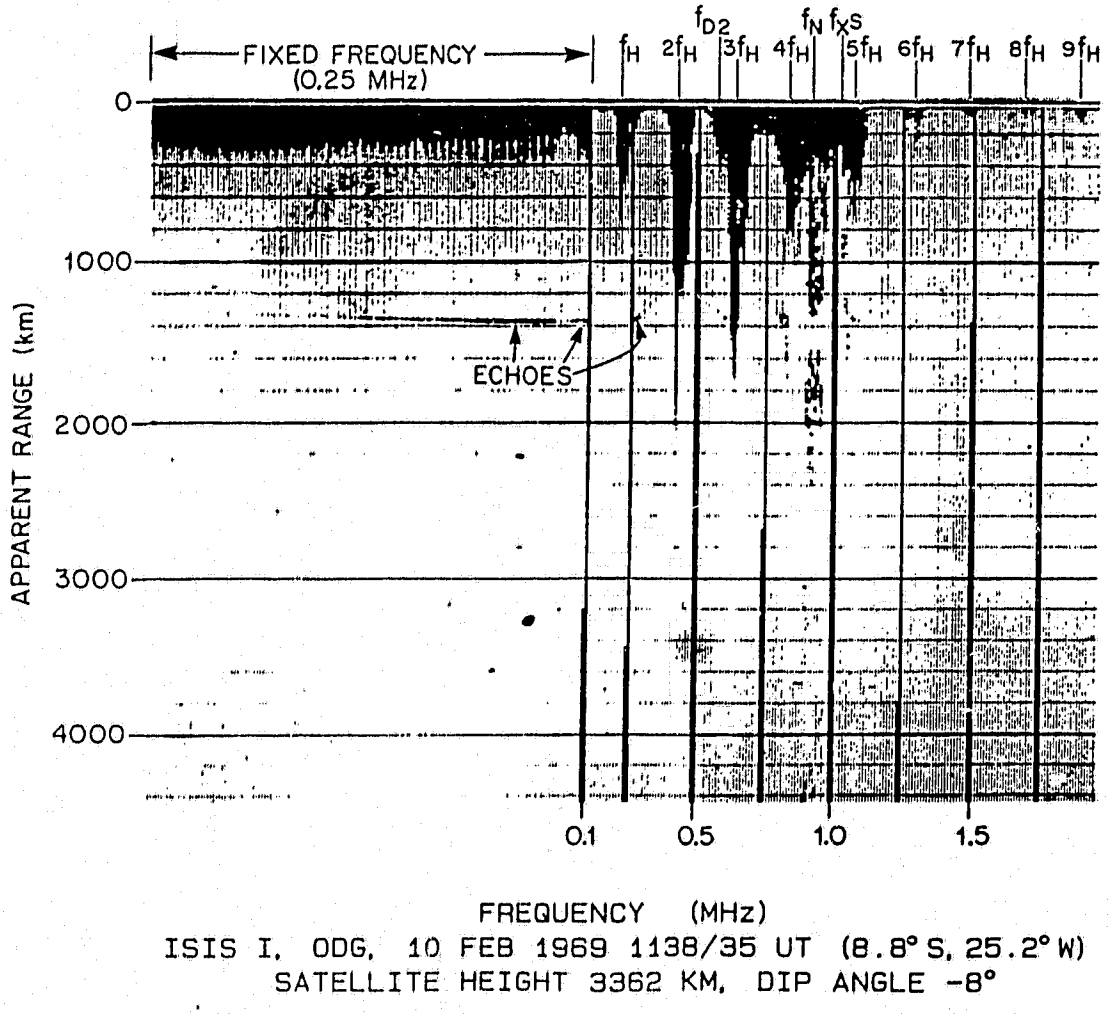

Figure 4.4: ISIS I combined fixed-frequency (0.25 MHz) (left portion) and swept-frequency ionogram (right portion) illustrating proton cyclotron echoes on both modes and the non-constant apparent range on the fixed-frequency mode.

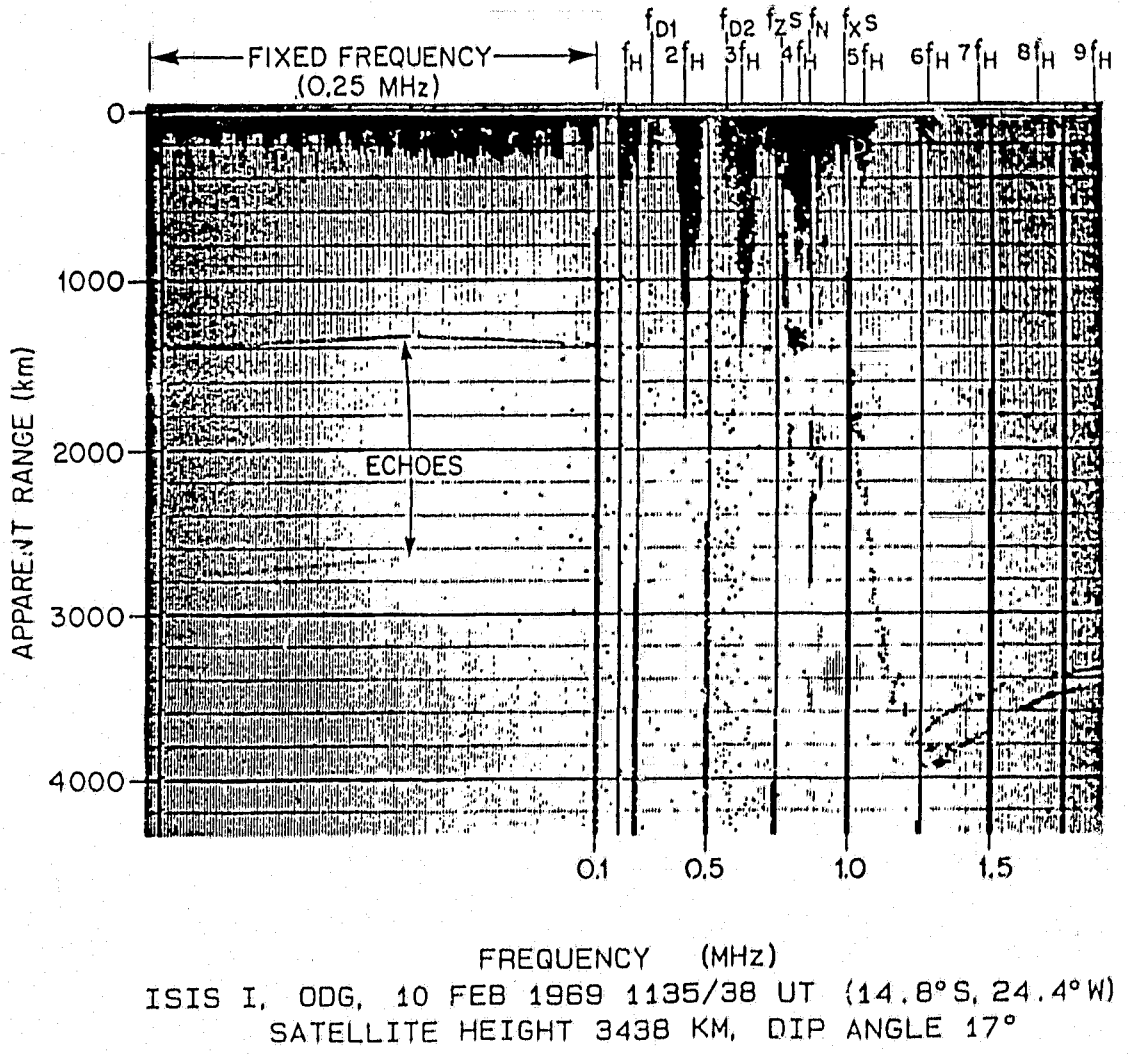

Figure 4.5: ISIS I combined fixed-frequency (0.25 MHz) (left portion) and swept-frequency ionogram (right portion) illustrating fundamental proton cyclotron echo and its second multiple echo, and their non-constant apparent ranges on the fixed-frequency mode.

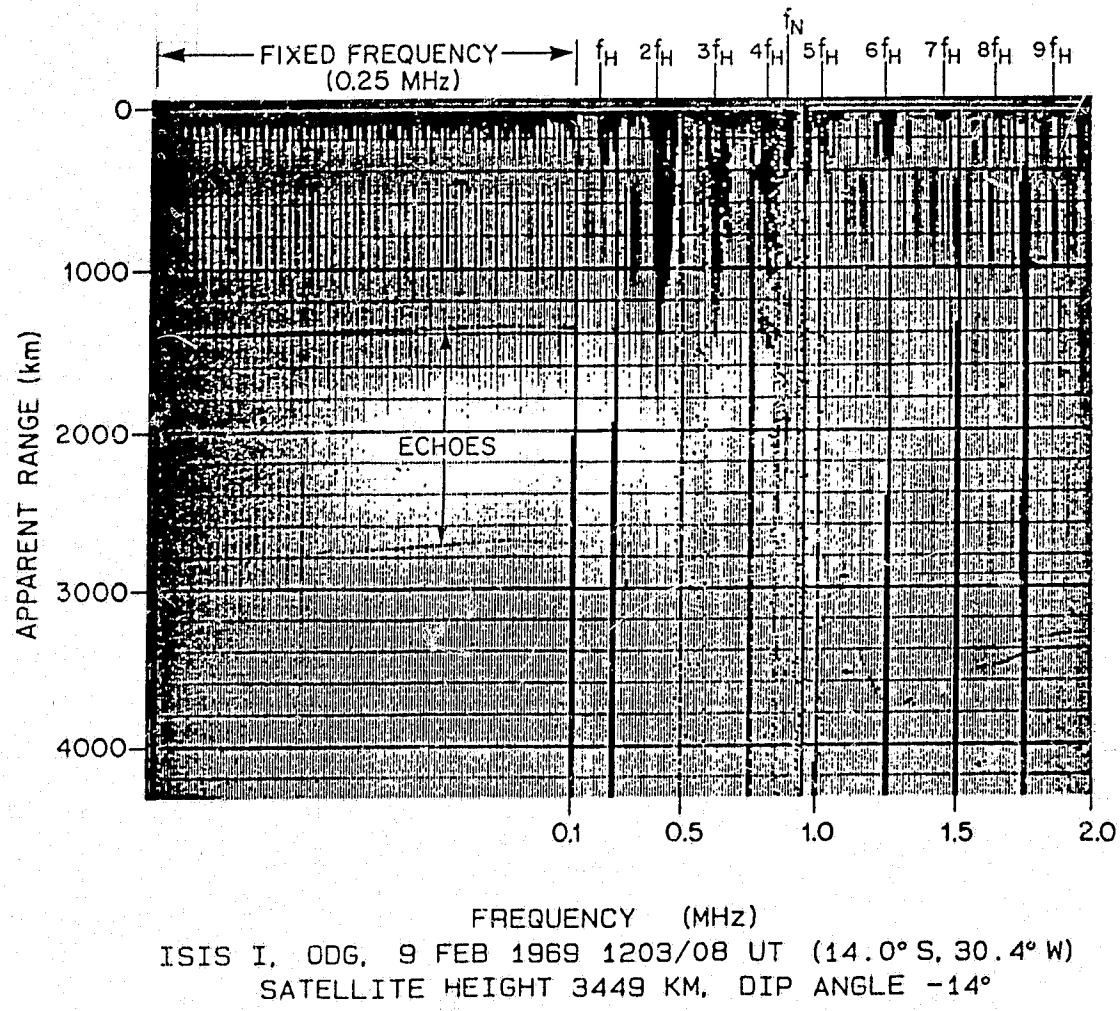

Figure 4.6: ISIS I combined fixed-frequency (0.25 MHz) (left portion) and swept-frequency ionogram (right portion) illustrating the fundamental proton cyclotron echo and its second multiple echo, and their non-constant apparent ranges on the fixed-frequency mode.

and are also observed on the fixed-frequency observations, some new features are obtained. For instance, under certain conditions the apparent range doesn't remain constant and the proton cyclotron echo would be subject to modulation in intensity. All the above observations occur at low dip angles ($\leq 17°$ from geomagnetic equator). This information will give some insight into the generation mechanism of the proton cyclotron echo. More discussions about the proton cyclotron echoes on the combined fixed-frequency and swept-frequency ionograms will be given in the next chapter, where we will deal with effects on proton cyclotron echoes of antenna orientation with respect to the earth's magnetic field.

Chapter 5

Effects on Proton Cyclotron Echoes of Antenna Orientation with Respect to the Earth's Magnetic Field

5.1 Introduction

Lockwood (1965) studied the antenna dependence of electron cyclotron resonances in the ionosphere by using the swept-frequency ionograms and magnetometer data obtained by the topside sounder satellite, Alouette I, and the celestial coordinate data of the Alouette I spin vector. He found that the number of electron cyclotron resonance spikes occurring on an ionogram is a maximum when the sounding antenna is parallel to the earth's magnetic field. Calvert *et al.* (Calvert, Knecht and VanZandt, 1964; Calvert and VanZandt, 1966; Calvert and McAfee, 1969) found that on the fixed-frequency ionograms of the topside sounder aboard Explorer XX the harmonics of the electron cyclotron resonances were modulated both in intensity and fringe pattern by the satellite spin. Two patterns were observed: one occurs when the antenna is parallel to the earth's magnetic field and does not exhibit fringes while the other occurs when the antenna is perpendicular to the earth's magnetic field and has modulated fringes. Stronger resonances and higher harmonics are observed when the antenna and the earth's magnetic field are aligned. The fundamental cyclotron resonance is not observed by Explorer XX because the sounding frequencies are too high. However Muldrew (1972b) presented a fringe pattern of f_H which occurred on an ISIS I ionogram, which was modulated by antenna orientation.

The antenna orientation effect on plasma frequency resonances has been

discussed by several authors (Calvert and VanZandt, 1966; Calvert and McAfee, 1969; Muldrew, 1972b; Fleury and Petit, 1974) in terms of the fixed-frequency ionograms recorded by Explorer XX. Calvert and VanZandt (1966), and Calvert and McAfee (1969) observed that the plasma frequency resonance consisted of two parts: a strong continuous signal lasting 3 to 4 ms and narrow columns of fringes. The antenna orientation has little effect on the first part, however, when the antenna was closely perpendicular to the earth's magnetic field, the second part occurs and has a narrow gap of intensity minimum in its middle. Muldrew (1972b) reported that nulls (gaps) occurred in the plasma frequency resonances on ISIS I fixed-frequency ionograms if the angle between the antenna and the earth's magnetic field was 90°. He gave a straightforward interpretation based on the oblique echo theory (McAfee, 1968; 1969a). The electric field of the wave responsible for the plasma frequency resonance is parallel to the earth's magnetic field. When the antenna is perpendicular to the earth's magnetic field, no electric field can be observed and, therefore, a null is to be expected. However Muldrew did not give an explanation for the signal of large duration on both sides of 90°. Fleury and Petit (1974) presented an ionogram recorded by the ISIS I satellite on March 5, 1970 at 1620. The fixed frequency record shows that the plasma frequency resonance signals strongly depend on the antenna orientation with respect to the earth's magnetic field. The angle between the earth's magnetic field and the long dipole antenna (which is used to record the fixed frequency ionogram) is deduced from the magnetometer data. The antenna orientation effects of the plasma frequency resonances have the following features: (1) when the antenna is nearly perpendicular to the earth's magnetic field, the duration of the resonance is a maximum and modulation fringes appears; (2) a very sharp minimum (null) in resonance intensity occurs in the middle of the the modulation fringe pattern; (3) the null does not appear exactly when $\theta = 90°$, but does appear when θ is close to 90°; (4) when the antenna is far from being

perpendicular to the earth's magnetic field, the modulation fringes disappear and the duration of the resonance shortens. Fleury and Petit gave a explanation of these features by considering the finite size of the antenna and its orientation to the earth's magnetic field.

The antenna orientation effects on the upper hybrid frequency and its second harmonic resonances were also studied (Calvert and VanZandt, 1966; Calvert, 1969; Calvert and McAfee, 1969). The upper hybrid frequency resonance is strongest when the antenna is perpendicular to the earth's magnetic field. The period of its modulation fringe is around 1 ms and decreases slightly during the decay. This period is somewhat greater when the antenna is more nearly parallel to the earth's magnetic field or when the resonance frequency is closer to $2f_H$. $2f_T$ resonance follows the f_T resonance in intensity, but it does not exhibit a fringe pattern.

It has been long-cherished to study the antenna orientation effects on proton cyclotron echoes with respect to the earth's magnetic field (Horita, 1987). This study can give some insight into the physics of the proton cyclotron echoes. It is helpful to study mechanisms of its generation. The purpose of this chapter is to investigate this problem.

5.2 Electromagnetic Wave in the Ionosphere

The propagation of electromagnetic waves in the ionosphere is described by a dispersion equation known as the Appleton-Hartree formula, which may written as follows (see, for example, Holt and Haskell, 1965; Budden, 1988)

$$n^2 = 1 - \frac{X(1-X)}{1 - X - \frac{1}{2}Y^2 sin^2\Theta \pm [\frac{1}{4}Y^4 sin^4\Theta + Y^2 cos^2\Theta(1-X)^2]^{\frac{1}{2}}} \tag{5.1}$$

where

$$X = \frac{\omega_N^2}{\omega^2}$$

$$Y = \frac{\omega_H}{\omega}$$

$$\omega_N^2 = \frac{Ne^2}{m\epsilon_0}$$

$$\omega_H = \frac{eB}{m}$$

Θ = the angle between the earth's magnetic field and the direction of propagation

ω_N = the angular plasma frequency

ω_H = the electron angular cyclotron frequency

ω = the angular frequency of the electromagnetic wave

e = the electron charge

m = the electron mass

N = the electron number density

ϵ_0 = the electric permittivity of free space

B = the magnetic induction of the earth's field

n = the refractive index of the ionospheric plasma

and collisions and ion motion are neglected; and a cold ionospheric plasma (i.e. the electron temperature $T_e = 0$) is assumed. Equation (5.1) shows that the refractive index depends upon the density of plasma, the frequency of the electromagnetic wave, and the magnitude and the direction of the earth's magnetic field. The electromagnetic wave in the ionosphere has two modes when the earth's magnetic field cannot be neglected. Each of the two electromagnetic wave modes may propagate in any direction with respect to the earth's magnetic field. Equation (5.1) for the general case is too complex and we, instead, consider the special case $\Theta = 0$ or $\Theta = \pi/2$ (principal solutions).

When $\Theta = 0$, equation (5.1) reduces to two solutions:

$$n_R^2 = 1 - \frac{X}{1 - Y} \tag{5.2}$$

$$n_L^2 = 1 - \frac{X}{1+Y} \tag{5.3}$$

These two principal waves propagate parallel to the earth's magnetic field and are circularly polarized with respect to the earth's magnetic field. Their electric fields rotate in opposite directions, and are, therefore, called the right-handed (R) and left-handed (L) waves respectively. The direction of rotation of the electric field for the R-wave corresponds to the direction of rotation of electrons, while the direction of rotation of the electric field for L-wave corresponds to the direction of rotation of protons.

When $\Theta = \pi/2$, equation (5.1) again reduces to two solutions:

$$n_O^2 = 1 - X \tag{5.4}$$

$$n_E^2 = 1 - \frac{X(1-X)}{1-X-Y^2} \tag{5.5}$$

These two principal waves propagate perpendicular to the earth's magnetic field. The first wave is linearly polarized along the earth's magnetic field direction, but is independent of the magnitude of the earth's magnetic field. This wave is called the ordinary (O) wave. The second wave has its electric field vector elliptically rotating in the plane perpendicular to the earth's magnetic field and is called the extraordinary (X) wave. The X-wave is both longitudinal and transverse wave, while other three are pure transverse waves.

The above discussion is summarized in Fig. 5.1. Fig. 5.1 illustrates the polarization of the four principal waves for propagation along the earth's magnetic field ($\Theta = 0$) and for propagation perpendicular to the earth's magnetic field ($\Theta = \pi/2$). When $\Theta = 0$, the two principal waves are circularly polarized; one wave (R-wave) rotates in the direction of the orbiting electron and exhibits electron cyclotron resonance. When $\Theta = \pi/2$, there are again two waves; one has its electric field vector parallel to the earth's magnetic field and is unaffected by its presence and the other is elliptically polarized in the plane perpendicular to

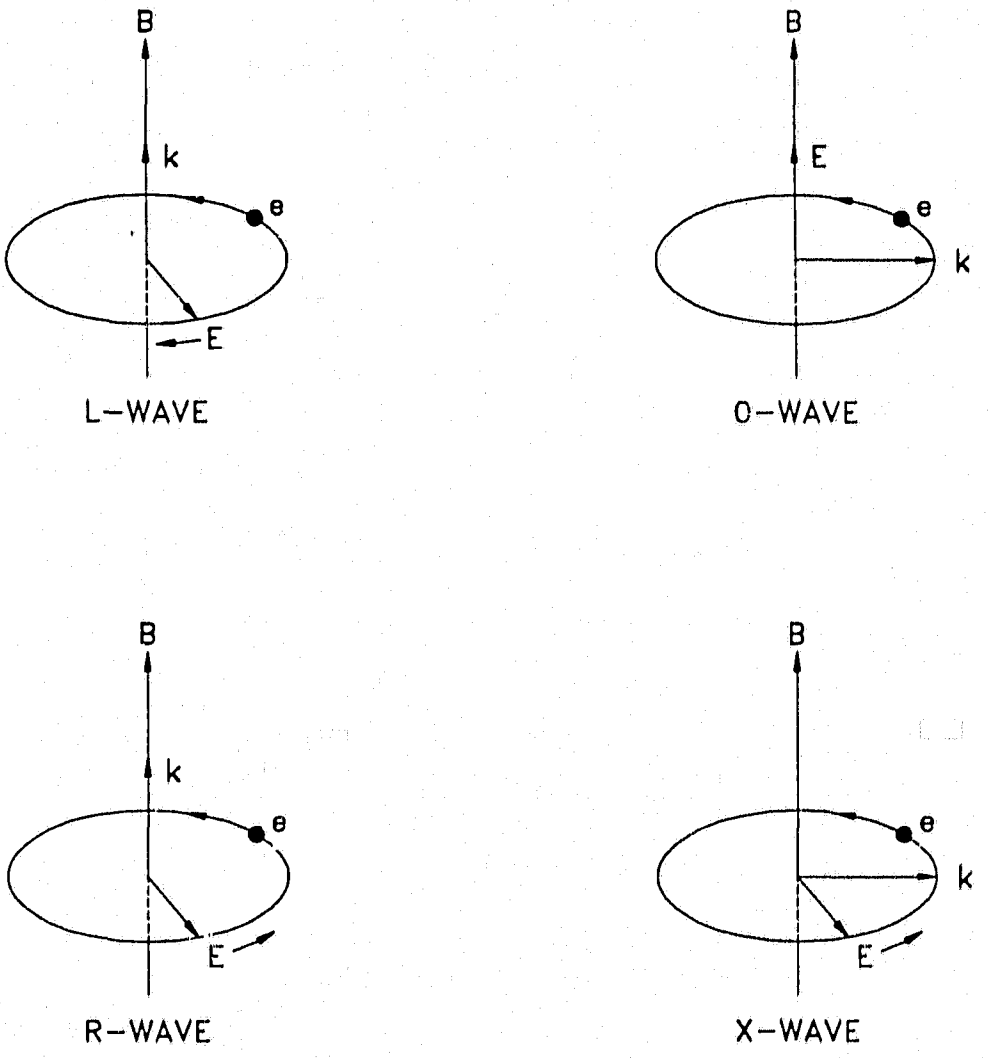

Figure 5.1: Polarization of the four principal waves that propagate parallel and perpendicular to the earth's magnetic field **B**; **E** is the electric field vector of the electromagnetic wave; **k** is the propagation vector; e is the electron charge and stands for an electron.

the earth's magnetic field.

We have discussed high frequency electromagnetic waves (ignoring ion motion) traveling in the ionosphere. Only principal waves traveling along or across the earth's magnetic field (R-wave and L-wave or O-wave and X-wave) were discussed. When waves propagate at any angle to the earth's magnetic field, there will be two modes for any angle of propagation, and their properties will be some combinations of the O-, X-, R- and L-waves.

5.3 Observations

As an International Topside Sounder Program – Alouette-ISIS Program, swept-frequency topside sounders were aboard the Canadian-built satellites: Alouette I (launched September 29, 1962) and Alouette II (launched November 29, 1965), and a fixed-frequency sounder was aboard a US-built satellite Explorer XX (launched August 25, 1964). These were followed by a combination of swept- and fixed-frequency sounder techniques which were aboard two Canadian-built satellites: ISIS I (launched January 30, 1969) and ISIS II (launched April 1, 1971). Proton cyclotron echoes were first observed on swept-frequency ionograms from the Alouette II satellite. The proton cyclotron echoes occur on the ionograms at nearly constant apparent ranges which correspond to the proton cyclotron period at the satellite position. Nearly all subsequent studies of the echoes have been based on the swept-frequency ionograms obtained from Alouette II, ISIS I or II satellites. The swept-frequency sounder provides soundings which are practically continuous in a band of frequencies at a series of discrete locations while the fixed-frequency sounder sounds continuously in space at a series of discrete frequencies. Thus the ionograms produced by swept-frequency observations show the delay of received signals as a function of frequency under nearly constant plasma conditions while the ionograms produced by fixed-frequency

observations show the delay as a function of the varying plasma conditions encountered by the satellite under a fixed frequency. Proton cyclotron echoes are also present on the fixed-frequency ionograms obtained from the ISIS I or ISIS II satellites. Since the sounding frequencies of the fixed-frequency ionograms are fixed, a proton cyclotron echo can be observed continuously over a time interval sufficient to determine the effect of the antenna orientation as the satellite spins. This chapter is devoted to the study of this problem by using the combined fixed- and swept-frequency ionograms recorded by ISIS I or II satellites.

Some experimental and orbital data of ISIS I and II are listed in Table 5.1. Some orbital parameters of the satellites are defined in Figure 5.2. ISIS II is

Data	ISIS I	ISIS II
Swept frequency	0.1 MHz to 20 MHz	0.1 MHz to 20 MHz
Transmitter power	400 W	400 W
Pulse repetition rate	30/sec	45/sec
Pulse width	100 μs	100 μs
Fixed frequency	0.25, 0.48, 1.0, 1.95, 4.0, and 9.303 MHz	0.12, 0.48, 1.0, 1.95, 4.0, and 9.303 MHz
Antennas (crossed dipoles)	73 and 18.7 meters	73 and 18.7 meters
Antenna crossover frequency	5 MHz	5MHz
Inclination	88.42°	88.16°
Perigee	578 km	1356 km
Apogee	3526 km	1423 km
Orbit period	128.42 min	113.55 min

Table 5.1: Some Experimental and Orbital Data of Two ISIS Satellites

the fourth and final satellite launched in the Alouette-ISIS series. Its spin axis was designed to be kept in the orbital plane (orbit-aligned) or orthogonal to the orbital plane (cartwheel). The spin rate varies between about 2.5 and 3.5 rpm and can be changed by about 0.1 – 0.15 rpm/orbit. For the orbit-aligned configuration the attitude can be changed by about 2.0° – 2.5°/orbit and in the cartwheel configuration, by about 0.5°/orbit. The tip of the spin axis vector lies on the celestial sphere. Its position is described by the celestial coordinate

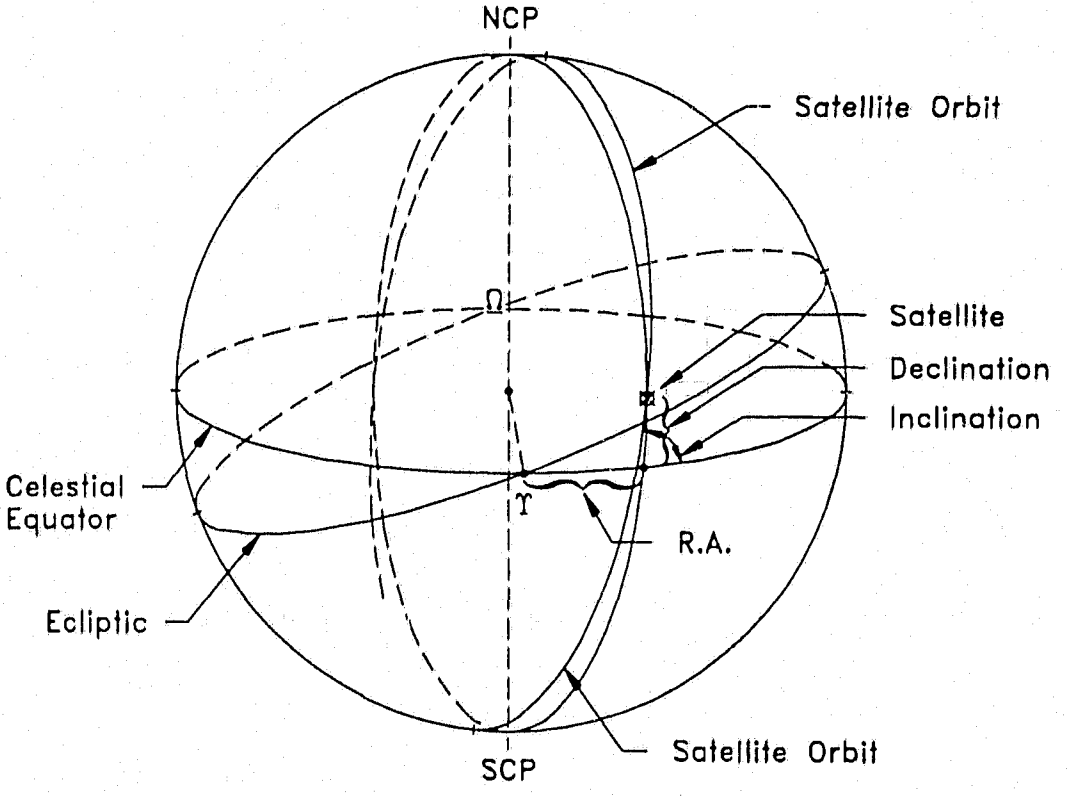

Figure 5.2: Satellite orbital parameters.

system (right ascension and declination or codeclination). The spin axis attitude of ISIS II in 1972 is given in Figure 5.3.

Figures 5.4, 5.5 and 5.6 are a set of ISIS II ionograms with the swept-frequency portion at the right and the fixed-frequency portion (0.12 MHz) at the left. The data were collected at the ground telemetry station in Santiago (SNT, $33.1°S$, $70.7°W$). These ionograms provide a great deal of information. We can see from them that the proton cyclotron echoes occur on the fixed-frequency portion and their intensity is subjected to modulation. On the swept-frequency portion the various plasma resonances are observed at the plasma frequency f_N, at the electron cyclotron frequency f_H and its harmonics $2f_H$, $3f_H$, $4f_H$ and $5f_H$, at the upper hybrid frequency f_T and its harmonic $2f_T$. Those labeled O, X are the echoes for vertical reflection of the usual electromagnetic waves by the underlying ionosphere (see 5.2). Their fade-outs occur when the sounding antenna is in a certain orientation.

Figure 5.7 shows another ISIS II ionogram recorded at the Santiago ground station. The fixed-frequency section of the ionogram excellently shows the echo and their harmonics. The first echo, the second echo, the third echo and the fourth echo are observed. They are all strongly subjected to modulation in intensity by the antenna orientation. On the swept-frequency section in addition to the plasma resonances we can see the harmonics of electron cyclotron resonance up to $11f_H$ and the diffuse resonance f_D. The first spur and the second spur occur on the side of the low frequency of the f_N resonance. Only the ordinary-wave trace and its fade-out are present, while the extraordinary-wave is absent. A so called spread echo occurs on the ordinary-wave trace between 1.5 and 2.5 MHz. It was explained in terms of backscatter from a low-latitude field-aligned irregularity (Lockwood and Petrie 1963; Muldrew, 1969). The Z-wave trace and its cutoff frequency f_zS is observed. We also observed the proton cyclotron echo, and its second and third harmonics which occurred between f_H and f_D

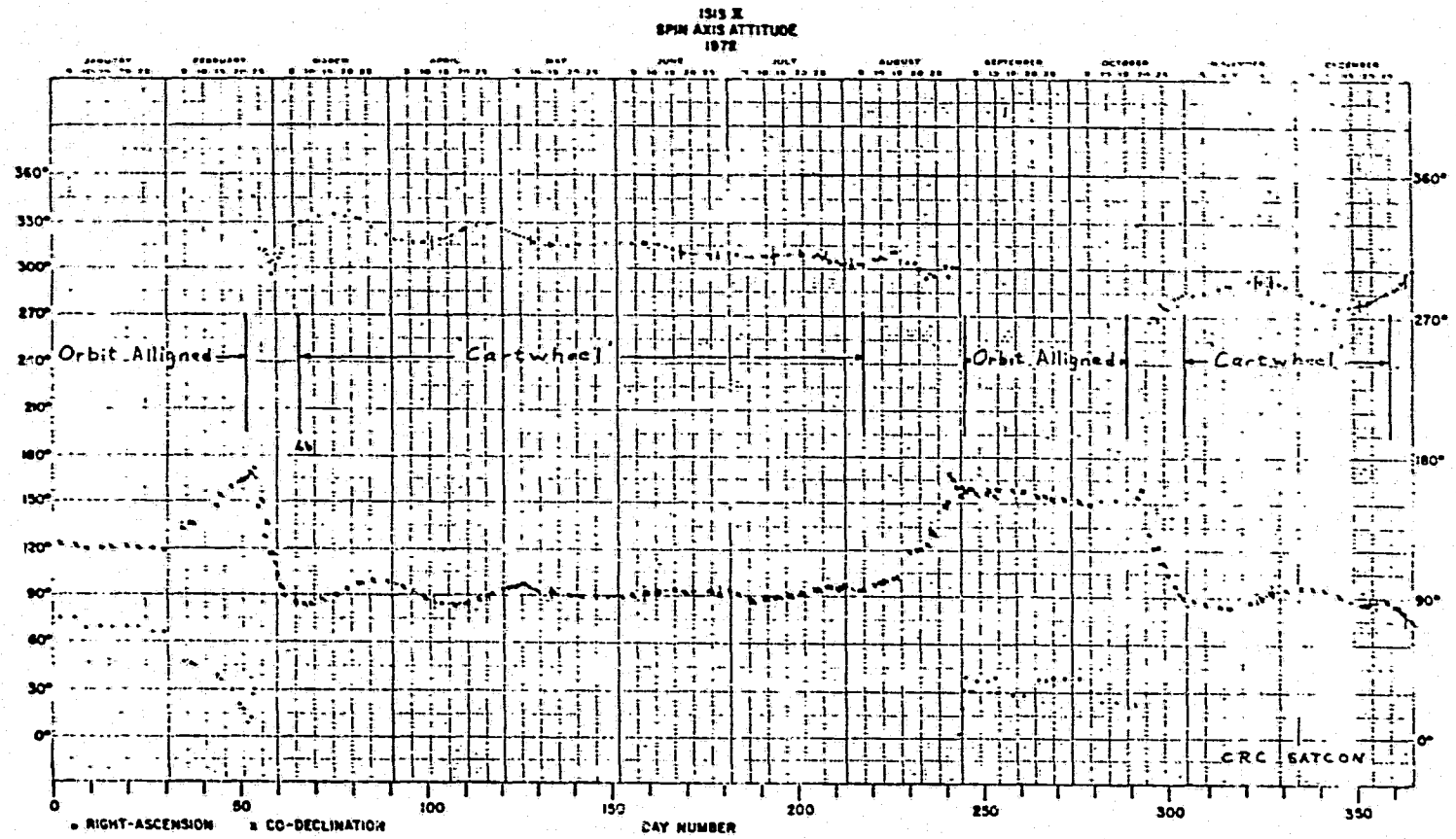

Figure 5.3: ISIS II spin axis attitude during the period of 1972.

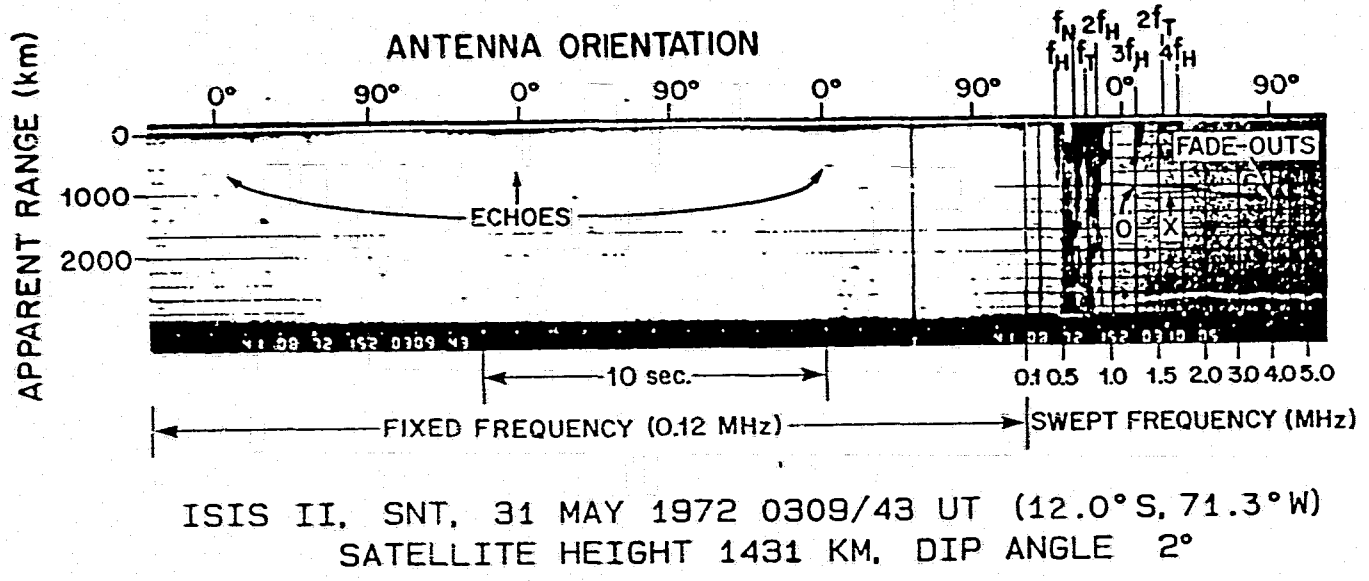

Figure 5.4: ISIS II combined swept-frequency and fixed-frequency ionogram illustrating modulation of the proton cyclotron echoes in intensity by antenna orientation. The ionogram was recorded at 0309/43 UT on May 31, 1972.

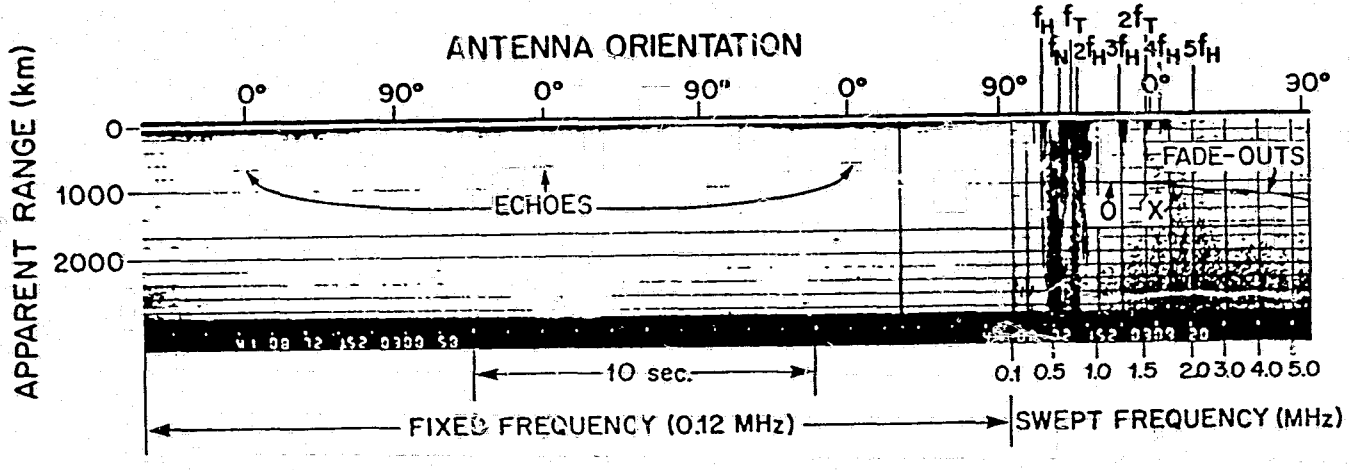

ISIS II, SNT, 31 MAY 1972 0308/58 UT (14.3° S, 71.2° W)
SATELLITE HEIGHT 1432 KM, DIP ANGLE −2°

Figure 5.5: ISIS II combined swept-frequency and fixed-frequency ionogram illustrating modulation of the proton cyclotron echoes in intensity by antenna orientation. The ionogram was recorded at 0308/58 UT on May 31, 1972.

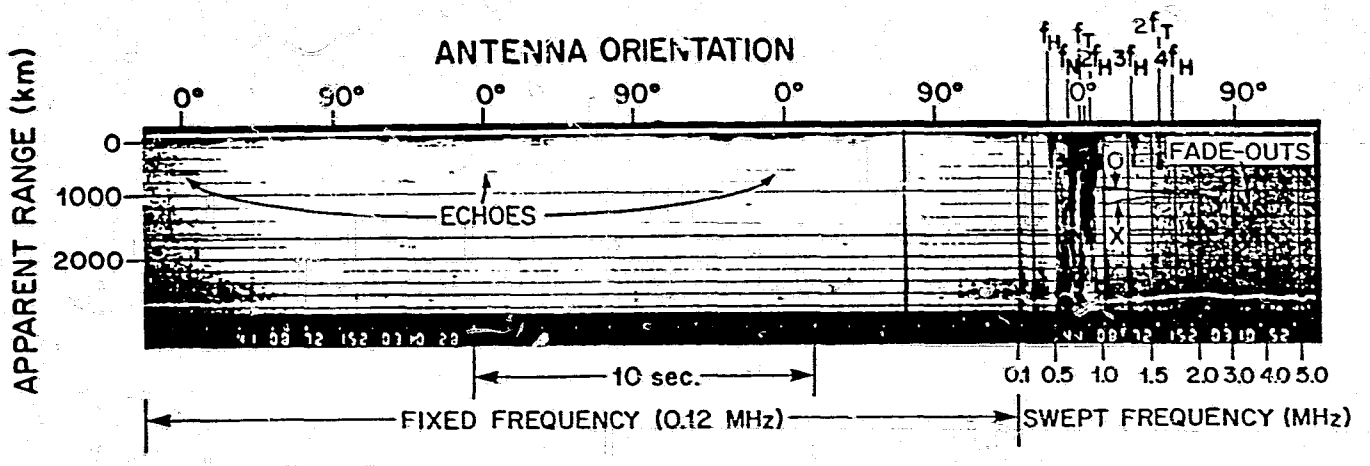

Figure 5.6: ISIS II combined swept-frequency and fixed-frequency ionogram illustrating modulation of the proton cyclotron echoes in intensity by antenna orientation. The ionogram was recorded at 0310/28 UT on May 31, 1972.

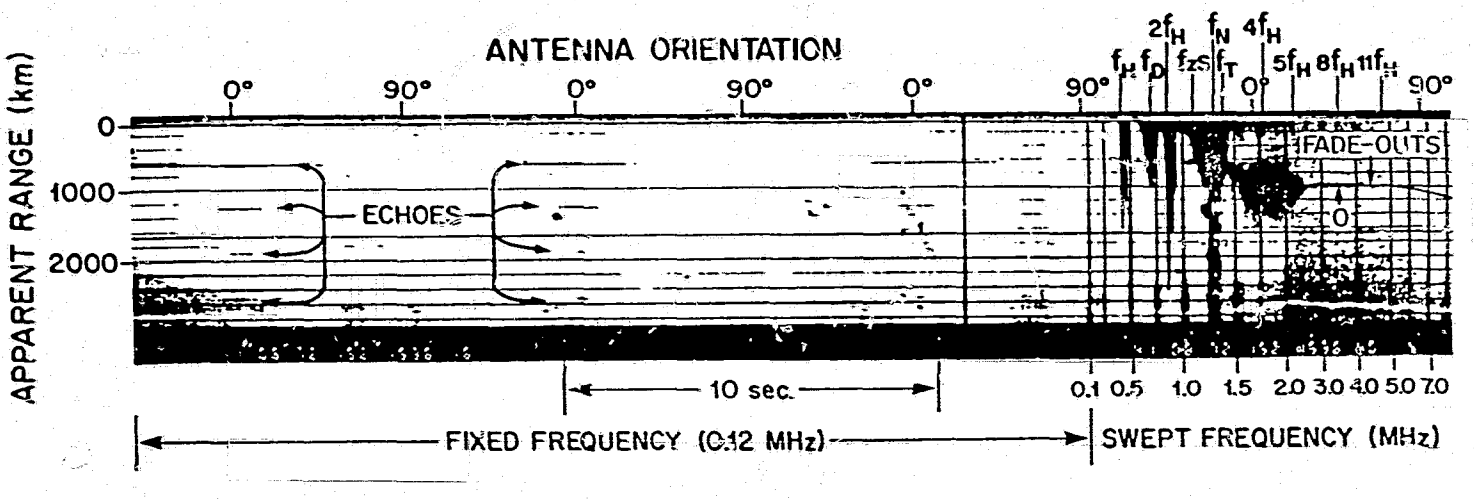

Figure 5.7: ISIS II combined swept-frequency and fixed-frequency ionogram illustrating modulation of the proton cyclotron echoes in intensity by antenna orientation. The ionogram was recorded at 1536/16 UT on May 31, 1972.

resonances on the swept-frequency section.

In this Chapter we will only concentrate our discussion on the modulation of the proton cyclotron echo in intensity by the antenna. In order to do so we must locate the position of the satellite and the orientation of the antenna in certain coordinate systems and at a certain time. Thus we will introduce the coordinate systems which will be employed.

5.4 Coordinate Systems

We will mainly employ three coordinate systems in our discussion. They include the terrestrial coordinate system, the celestial coordinate system and the geomagnetic coordinate system.

5.4.1 Terrestrial Coordinate System

The terrestrial coordinate system is based upon the earth's rotation, and therefore, upon the positions of its north and south poles and the position of its equator. In this system the latitude of a point is its distance in degrees north or south from the equator; its value ranges from 0° at the equator to 90° at either pole. The poles are distinguished by the letter N or S for north or south respectively. The longitude of the point is measured in degrees east or west, along the equator, to the meridian containing the point from a reference meridian, which is chosen as that which passes through Greenwich in England. This coordinate system is also called the geographical coordinate system or the geodetic coordinate system.

5.4.2 Celestial Coordinate System

The celestial coordinate system is quite similar to the terrestrial coordinate system. The north and south celestial poles are found by extending the rotational

axis of the earth to the celestial sphere. The celestial equator, by definition, is a great circle 90° away from either celestial pole, and hence it is in the plane of the earth's equator. In the celestial coordinate system directly analogous to the terrestrial latitude is the coordinate declination (DEC). Declination is measured in degrees north (+) or south (−) from the celestial equator to the north celestial pole or the south celestial pole along a meridian. The coordinate corresponding to terrestrial longitude is called the right ascension (R.A.). The reference ("zero") meridian of the right ascension is an arc of a great circle on the celestial sphere that passes through the celestial poles and the vernal equinox (V.E.). The right ascension of an object is thus the angular distance measured from the V.E. along the celestial equator eastward to the great circle passing through the celestial poles and the object. The celestial coordinate system is sometimes called the equatorial coordinate system.

5.4.3 Geomagnetic Coordinate System

The magnetic field of the earth is approximated by a uniformly magnetized sphere, which is equivalent to the field of a central magnetic dipole aligned parallel to the axis of magnetization. The points at which the extension of the axis of the central magnetic dipole intersects the earth's surface are called the geomagnetic poles. The north geomagnetic pole (actually the south pole of the magnetic dipole, since it attracts the north pole of a compass needle) is in northwestern Greenland at about 78.5°N, 69.1°W in the geographic coordinate system and the south geomagnetic pole is at about 78.5°S, 110.9°E in Antarctica at the present time. The axis of the magnetic dipole is inclined to the rotation axis by 11.5°. The geomagnetic coordinate system is based on the geomagnetic poles which are defined as ±90° geomagnetic latitude; plus is geomagnetic north. A geomagnetic equator is defined as a great circle located 90° away from

either pole in geomagnetic latitude and hence its geomagnetic latitude is zero. The prime geomagnetic meridian is the Greenwich half of the great circle that passes through both geomagnetic and geographic poles; it lies along a geographic meridian at about 70°W over most of its length. Geomagnetic longitude is measured eastward from the prime geomagnetic meridian. The geomagnetic poles are different from the magnetic poles (or magnetic dip poles) (approximately 73°N, 100°W and 68°S, 143°E in the geographic coordinate system at present time) where the magnetic dip angle becomes 90° (the horizontal component of the magnetic field of the earth is zero). The magnetic equator (or the magnetic dip equator) is the locus of points where the magnetic field is parallel to the earth's surface (the dip angle is equal to zero).

5.5 Analysis

Partial orbital data of the ISIS II satellite for May 31, 1972 from the World Map is given in Table 5.2 on page 86, where

GMT—Greenwich mean time, or Universal time (UT) in HHMMSS
LAST—Local apparent solar time in HHMMSS
GDLAT—Geodetic latitude in Degrees
GDLONG—Geodetic longitude in Degrees
HGT—Height above the geoid in Kilometers
GMLAT—Geomagnetic latitude in Degrees
GMLONG—Geomagnetic longitude in Degrees
DIP—Angle of dip of earth's magnetic field in Degrees.

Let us take a look at Figure 5.4. We can see that the fade-outs of the O-wave and X-wave start at 0310:12.3 UT on May 31, 1972, but we do not know when they end since the antenna crossover frequency is 5 MHz (see Table 5.1). The long antenna (73 meters) was used for the band 0.1 to 5 MHz, while the short

antenna (18.7 meters) was used from 5 MHz upward. The two dipoles were perpendicular to the spin axis of the satellite and to each other. If we take 0310:13.1 UT as the center time of the fade-outs, we can derive from Table 5.2 the geodetic coordinates (−10.40°, −71.38°), the geomagnetic coordinates (1.29°, −2.35°) and the dip angle (4°). Therefore the satellite was very close to the magnetic dip equator and the geodetic equator during the fade-outs of the O-wave and X-wave. The geomagnetic poles are approximately at 78.5°N, 69.1°W and 78.5°S, 110.9°E in the geodetic coordinates at the present time. The axis of the dipole is inclined to the rotation axis by 11.5°. However, for the sake of convenience in our discussion, we ignore the above difference. Also we can see from Table 5.2 that the ISIS II satellite was moving from south to north along a geodetic longitude about 71°*W*. The spin axis of ISIS II was designed to be kept in the orbital plane (orbit-aligned) or at right angles to the orbital plane (cartwheel) (Daniels, 1971; Burrows, Cogger and James, 1981). For the orbit-aligned configuration the attitude can be changed by 2.0° - 2.5°/orbit and in the cartwheel configuration, by about 0.5°/orbit. From Figure 5.3 we know that the spin axis was in the cartwheel configuration during this time and hence was perpendicular to the orbital plane. Since the orbit of the satellite is approximately in the south-north direction (the satellite moving from south to north), the spin axis of the satellite is approximately in the west-east direction. In what follows we discuss this more accurately.

The sun moves along the ecliptic inclined at an angle of 23.5° to the celestial equator (Figure 5.8). The sun crosses the celestial equator from south to north at the vernal equinox (♈) each year about March 21. The position of the sun on May 31, 1972 was C. We make the meridian through NCP, C and SCP, crossing the celestial equator at A. Consider the spherical triangle ABC with the sides a, b and c. The spherical angles BAC, CBA and ACB are denoted simply by A,

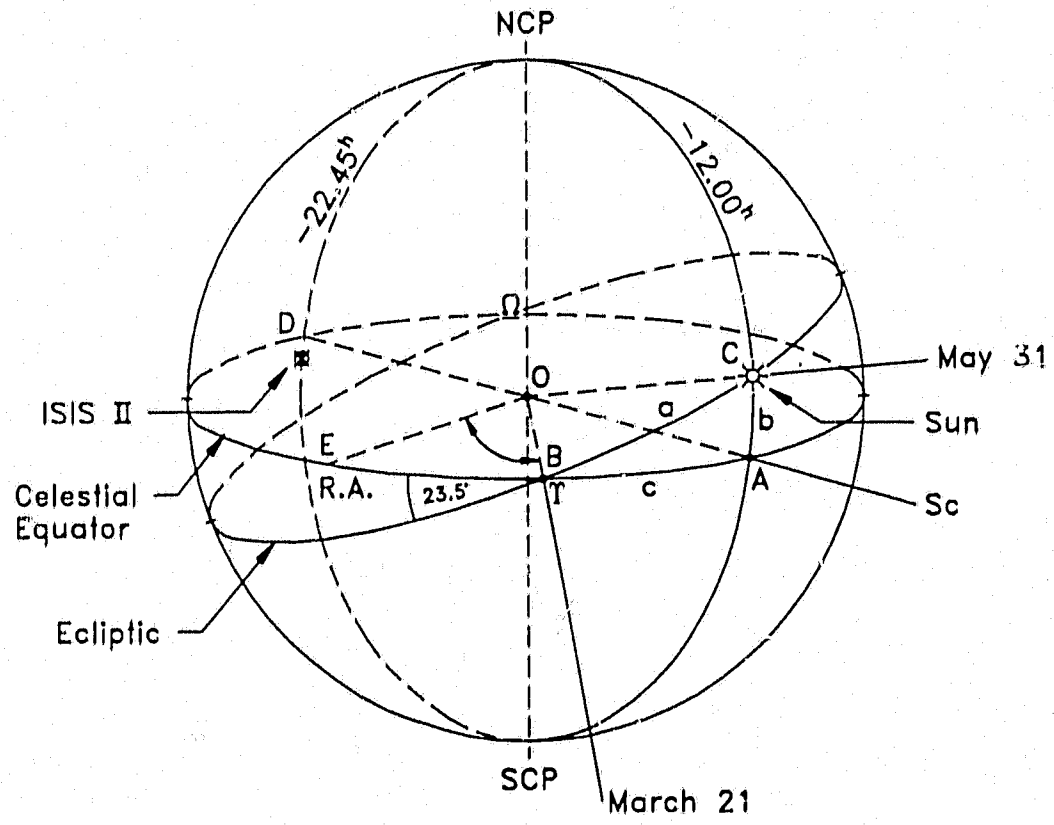

Figure 5.8: The positions of the sun and ISIS II satellite on the celestial sphere on May 31, 1972 0309/43 UT and the orientation of the spin axis of the satellite.

B and C respectively. Since

$$B = 23.5°$$

$$A = 90°$$

$$a = \frac{71 days}{366 days} \times 360° = 69.8°,$$

we have from the sine-formula and the cosine-formula that

$$b = \frac{a sin B}{sin A} = 27.8°$$

$$cos c = \frac{cos a}{cos b} = 0.3904$$

and

$$c = 67.0°.$$

Thus the declination (DEC) and the right ascension (R.A.) of the sun on May 31, 1972 are 27.8° and 67.0° respectively.

From Table 5.2 we can get that LAST is −222654 at 0309/43 UT and hence we get the hour angle between the satellite and the sun, which is 102654 (or 156.7°), i.e. $\angle AOD = 156.7°$. The latitude of the satellite is $12.0°S$. the position of the satellite is determined (shown in Figure 5.8).

From Figure 5.3 the right ascension and the declination of the spin axis of the satellite is about 315° and 0° respectively. So $\angle BOE = 45°$ and hence $\angle DOE = 360° - \angle BOE - \angle AOB - \angle AOD = 91.3°$. The same procedure is employed for Figure 5.5 (0308/58 UT) and Figure 5.6 (0310/28 UT). We get $\angle AOD = 91.4°$ and 91.2° respectively. The spin axis is parallel to the celestial equator plane. Therefore we conclude that the orientation of the spin axis was in the west - east direction and parallel to the horizontal plane of the earth in about 1.3° differences, with tending downwards to the east. Since Antennas are perpendicular to the spin axis, antennas are in the vertical plane containing the north-south direction (if 1.3° differences are ignored).

The antenna system contains a passive electrical crossover network located between the transmitter-receiver system and two orthogonal antennas. Below the crossover frequency of 5 MHz the long antenna is used, while above 5 MHz the short antenna is used. We discuss observations below the frequency of 5 MHz and hence we consider the orientation of the long antenna with respect to the earth's magnetic field. Since the direction of geomagnetic field is in the south - north direction, the angle between each antenna and the geomagnetic field changes between 0° and 90° twice per each rotation. The spin period of ISIS II varies between about 17 and 24 seconds. at the time the observation was made the spin period was 18 seconds.

From previous discussions (see 5.2) we know when the long antenna points downward (i.e. when the long antenna is perpendicular to the earth's magnetic field), the O-wave and the X-wave should fade out. In our case when the O-wave trace or X-wave trace fades out, the long antenna must point downward and is perpendicular to the earth's magnetic field. The angle between the long antenna and the earth's magnetic field is 90°. Since the dipole antenna is symmetric with respect to the spin axis, one-fourth period (4.5 second) later after the long antenna points downward it becomes parallel to the earth's magnetic field and the angle between them becomes zero, then one-fourth period later the long antenna point downward again, and so on. The values of the angle between the long antenna and the earth's magnetic field, deduced from such a way, is plotted along the tops of ionograms in Figures 5.4, 5.5, 5.6, 5.7, 5.10 and 5.11.

From Figures 5.4, 5.5 and 5.6 we can see that the intensity of the proton cyclotron echo obviously depends upon the angle between the earth's magnetic and the long dipole antenna, since the proton cyclotron echo is observed only when the angle is near the zero value. Thus the proton cyclotron echo appears only when the dipole is nearly parallel to the earth's magnetic field.

Figure 5.7 is a very good example of the proton cyclotron echoes. The ionogram was taken on May 31, 1972 at 1536/16 UT when the ISIS II satellite was located at $13.0°S$, $77.7°W$ geographic coordinates and 1368 km altitude. The dip angle was 1°. The satellite was moving southward near the celestial equator plane. The positions of the sun and the ISIS II satellite on the celestial sphere on May 31, 1972 1536/16 UT and the orientation of the spin axis of the satellite are shown in Figure 5.9. Since this ionogram was obtained on the same day as previous 3 ionograms (Figures 5.4, 5.5 and 5.6), the declination (DEC) and the right ascension (R.A.) are the same (27.8° and 67.0° respectively). From Table 5.2 we get that LAST is 102741 at 1536/16 UT. Thus the hour angle between the satellite and sun is 013219 (or 23.1°), i.e. $\angle AOD = 23.1°$. The right ascension and the declination of the spin axis of the satellite are 315° and 0° respectively (see above). Hence $\angle DOE = \angle BOE + \angle AOB - \angle AOD = 88.9°$. The conclusion is the the orientation of the spin axis was in the west-east direction and parallel to the horizontal plane of in 1.1° differences, with tending downwards to the west. The antenna was turning in the vertical plane containing the north - south direction with the spin period of the satellite (1.1° differences are ignored).

Figure 5.7 shows clearly that the fundamental proton cyclotron echo and its harmonics in intensity as well as the number of higher order harmonics are modulated by the antenna. When the sounding antenna is parallel to the earth's magnetic field, the fundamental proton cyclotron echo and its harmonics are strongest and the number of higher order harmonics observed is a maximum; when the sounding antenna is perpendicular to the earth's magnetic field, the fundamental proton cyclotron echo and its harmonics are not observed.

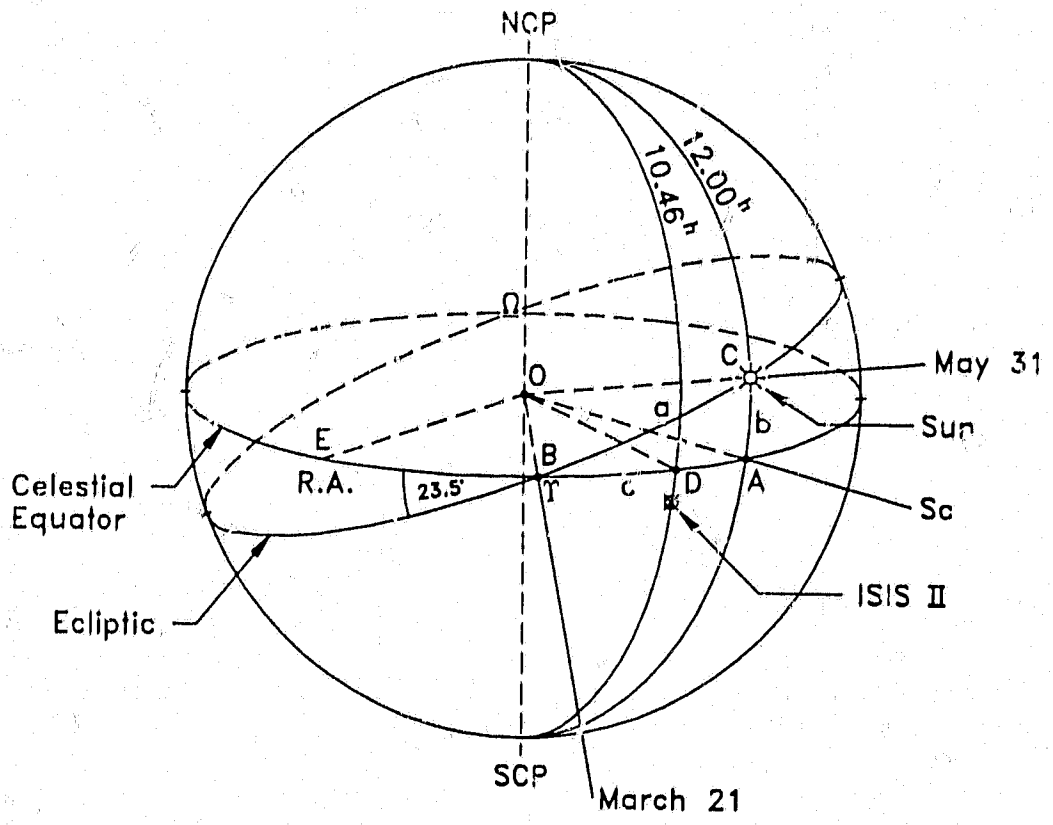

Figure 5.9: The positions of the sun and the ISIS II satellite on the celestial sphere on May 31, 1972 1536/16 UT and the orientation of the spin axis of the satellite.

5.6 Summary

The occurrence of proton cyclotron echoes and their harmonics in the ionosphere has been observed by the topside-sounder satellites: Alouette II, ISIS I and ISIS II (Matuura and Nishizaki, 1969; Horita, 1974 and 1987; Benson, 1975; Ondoh *et al.*, 1975; Oya, 1978; Chen and Horita, 1991). These studies are based on the swept-frequency ionograms from the satellites mentioned above. The swept-frequency sounder provides soundings with a gradually increased frequency so that each pulse is slightly higher in frequency than the preceding pulse. The proton cyclotron echoes usually appear in a particular frequency range (Horita 1974 and 1987; Oya, 1978). It is not possible to study on only swept-frequency ionograms the effects on the proton cyclotron echoes of antenna orientation with respect to the earth's magnetic field. Proton cyclotron echoes are also present on the fixed-frequency ionograms from ISIS I and ISIS II (see Chapter 4). The fixed-frequency sounder sounds in space at its six discrete frequencies. The data corresponding to each of the six frequencies are separated and six ionograms are generated. The ionograms produced by fixed-frequency observations show the delay as a function of varying plasma conditions encountered by the satellite. When the plasma parameters in a region are appropriate, the proton cyclotron echo may be under observation for a time interval long compared to several spin periods of the satellite. The modulation of the proton cyclotron echo intensity by the spin of the satellite has been observed (see Chapter 4). In this Chapter we have studied the antenna orientation effects of the proton cyclotron echoes to the earth's magnetic field in detail by using the combination of the fixed-frequency and the swept-frequency soundings. It has been shown the higher intensity and higher harmonics of proton cyclotron echoes occur when the sounding antenna is parallel to the earth's magnetic field.

A proton cyclotron echo occurs at RF between 0.1 MHz and 0.25 MHz on the

swept-frequency ionogram in Figure 5.10, but not in Figure 5.11. Figure 5.11 was obtained only about 45 seconds later than Figure 5.10. The only difference is that at RF range where the proton cyclotron echo is supposed to occur the sounding antenna is close to be aligned with the earth's magnetic field in Figure 5.10, but not in Figure 5.11. Thus the proton cyclotron echo occurs only when both the right RF range and right antenna orientation are satisfied simultaneously. This can explain why the proton cyclotron echoes on the swept-frequency ionograms occur less than they are supposed to.

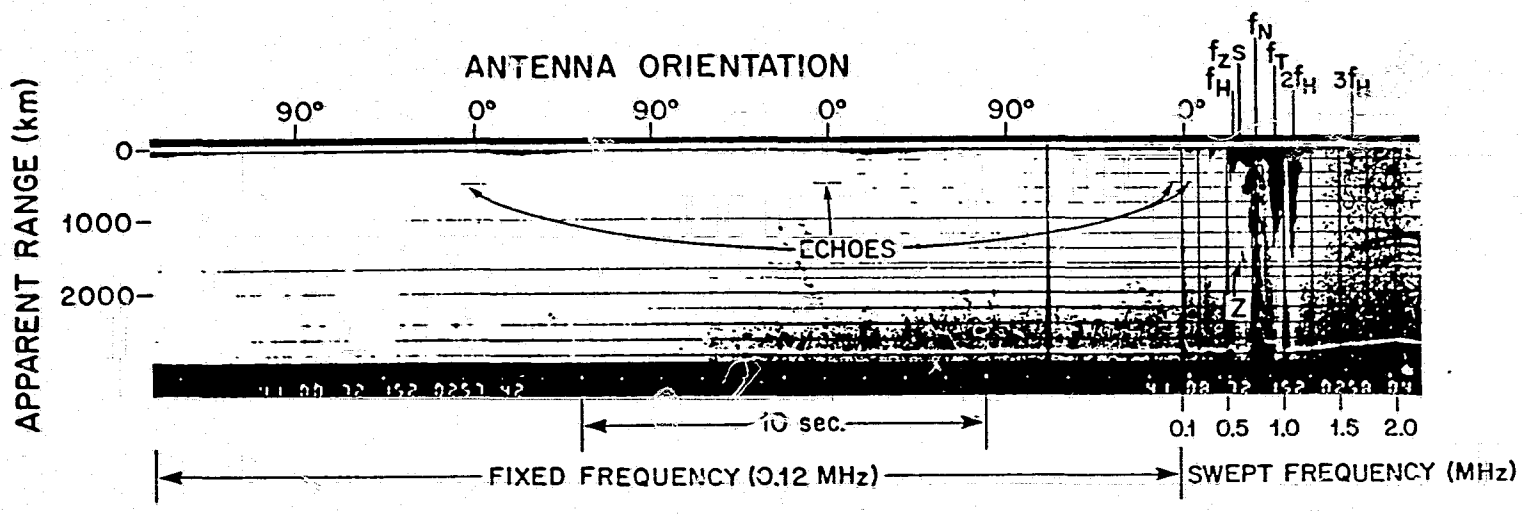

ISIS II, SNT, 31 MAY 1972 0257/42 UT (49.7° S, 70.1° W)
SATELLITE HEIGHT 1440 KM, DIP ANGLE -50°

Figure 5.10: ISIS II combined swept-frequency and fixed-frequency ionogram illustrating modulation of the proton cyclotron echoes in intensity by antenna orientation and showing occurrence of the proton cyclotron echoes on both swept-frequency and fixed-frequency soundings. The ionogram was recorded at 0257/42 UT on May 31, 1972.

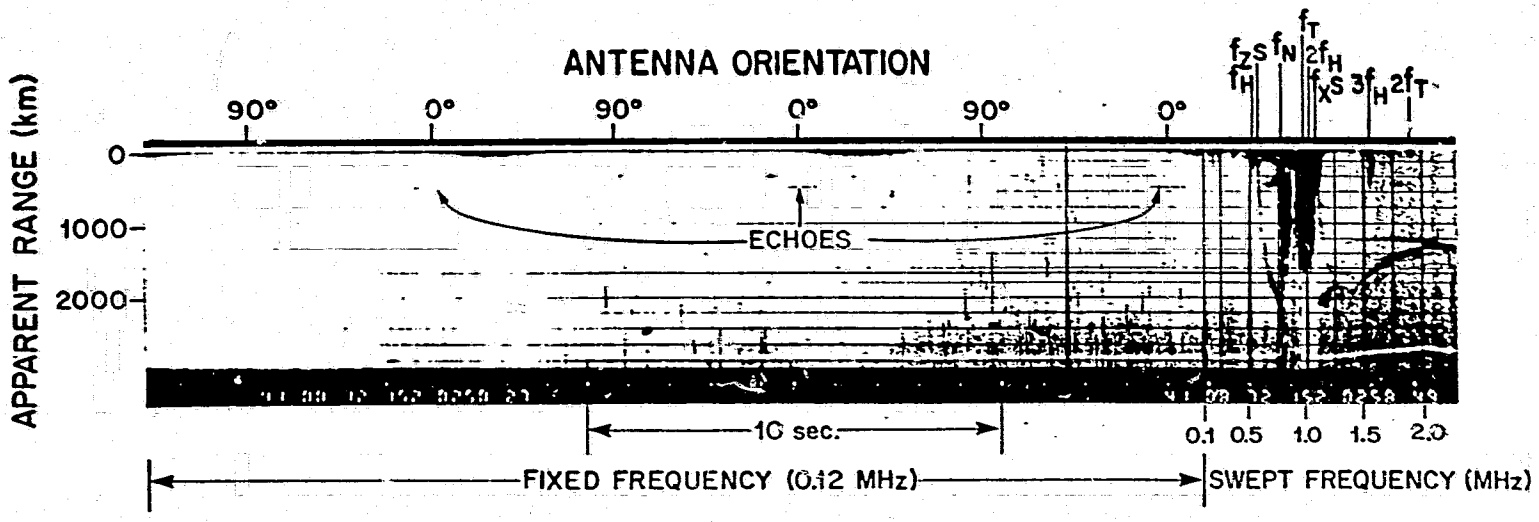

Figure 5.11: ISIS II combined swept-frequency and fixed-frequency ionogram illustrating modulation of the proton cyclotron echoes in intensity by antenna orientation and showing occurrence of the proton cyclotron echoes on fixed-frequency sounding only. The ionogram was recorded at 0258/27 UT on May 31, 1972.

GMT	LAST	GDLAT	GDLONG	HGT	GMLAT	GMLONG	DIP
025600	-221803	-55.07	-70.09	1440	-43.57	-0.86	-55
025700	-221911	-51.94	-70.06	1440	-40.24	-0.86	-52
025800	-222009	-48.81	-70.07	1440	-37.11	-0.88	-49
025900	-222101	-45.67	-70.10	1440	-33.98	-0.93	-47
030000	-222147	-42.54	-70.16	1439	-30.84	-0.99	-44
030700	-222544	-20.54	-70.92	1434	-8.85	-1.82	-13
030800	-222610	-17.39	-71.06	1433	-5.70	-1.98	-8
030900	-222636	-14.24	-71.21	1432	-2.55	-2.14	-2
031000	-222701	-11.09	-71.35	1431	0.60	-2.31	3
031100	-222726	-7.94	-71.50	1430	3.75	-2.48	9
031200	-222750	-4.78	-71.65	1429	6.91	-2.66	15
153500	102709	-8.90	-77.55	1365	2.67	-8.46	6
153600	102734	-12.11	-77.70	1367	-0.54	-8.50	0
153700	102800	-15.31	-77.84	1369	-3.75	-8.45	-5
153800	102826	-18.52	-77.98	1371	-6.95	-8.57	-11

Table 5.2: Partial Orbital Data of the ISIS II Satellite for May 31, 1972 from the World Map

Chapter 6

Proton Cyclotron Echoes on f_{Qn} Resonances

6.1 Introduction

Waves in a hot magnetoplasma were treated by Bernstein (1958). In Bernstein's approach the full set of Maxwell equations is employed and the ion dynamics are included. However, the electrostatic limit and neglecting ion motions have been considered. Bernstein's analysis shows that an initial perturbation of the plasma can lead to electrostatic waves. For the electron electrostatic waves propagating perpendicular to the constant magnetic field, there are gaps in the spectrum of allowed frequencies at multiples of the electron cyclotron frequency. Wave propagation is possible without Landau damping in a band of frequencies between harmonics of the electron cyclotron frequency. These waves are called the electron Bernstein waves or Bernstein modes. Stix (1962) and McAfee (1973) have shown that, for given plasma parameters, the electron Bernstein waves should occur above the upper hybrid frequency. An approximate formula has been developed by Dougherty and Monaghan (1966) to predict the frequencies at which these electrostatic resonances should appear on the topside ionograms. The formula can be written as

$$f_{Qn} = nf_H + \frac{0.464 f_N^2}{n^2 f_H} \tag{6.1}$$

where f_{Qn}, f_N and f_H are the frequencies of the resonances for the electron Bernstein waves, the electron plasma frequency and the electron cyclotron frequency respectively, and n is an integer. The f_{Qn} frequencies depend on both

the electron cyclotron harmonic and plasma frequencies.

The electron Bernstein waves or resonances were first observed on Alouette II topside ionograms by Warren and Hagg (1968). They called them the f_{Qn} resonances, where $nf_H < f_{Qn} < (n+1)f_H$, and they have been identified from f_{Q2} to f_{Q6} (Chapman and Warren, 1968). The f_{Qn} resonances are observed mainly at low latitudes. The f_{Q3} occurs most frequently, the f_{Q2} less frequently; the f_{Q4}, f_{Q5} and f_{Q6} are seldom observed because the frequencies of these resonances are often too close to their related electron cyclotron harmonic frequencies to permit separation. A convenient empirical relationship for the f_{Q2} and f_{Q3} resonances has been given from the Alouette II ionograms (Hagg, Hewens and Nelms, 1969):

$$f_{Q2} \approx 0.15\frac{f_N^2}{f_H} + 1.85f_H \tag{6.2}$$

$$f_{Q3} \approx 0.075\frac{f_N^2}{f_H} + 2.925f_H. \tag{6.3}$$

where f_{Qn}, f_N and f_H are in MHz.

The electron plasma resonances observed by topside sounders have been attributed to electrostatic waves. These resonances may be interpreted as due to the propagation characteristics of two kinds of electrostatic waves: one is the accompanying waves moving along with the satellite, their group velocity being equal to the satellite's velocity with respect to the plasma; the other is reflected waves, which propagate up to several hundred meters from the satellite and return to the receiver. Muldrew (1972a) has used dispersion equations for oblique propagation in a hot magnetoplasma to perform ray tracing near f_{Q2}. He has found that the waves responsible for the observed resonance effects have group velocities that are almost equal to the satellite velocity for the duration of the observed resonance. Thus we can say that for the f_{Q2} resonance, and probably for all the f_{Qn} resonances, the group velocity (or a component of the group velocity) of waves responsible for the resonances very nearly matches the

satellite velocity at the time of observation. So the f_{Qn} resonances should be attributed to the accompanying waves.

The electrostatic resonances f_{Qn} originally identified in the topside ionosphere have also been identified in the plasmasphere (Oya and Ono, 1981; Oya, Ono and Kamada, 1981; Oya *et al.*, 1990) and in the outer magnetosphere (Etcheto, de Feraudy and Trotignon, 1981) far from the earth. The observed f_{Qn} resonances in the plasmasphere and in the outer magnetosphere have much longer duration times and stronger intensity compared with the observations in the ionosphere.

It is found that the f_{Qn} resonances often split into two resonances called f_{Qn} and $f_{Q'n}$, a few hundred Hz apart (Higel, 1978; Etcheto *et al.*, 1981). Benson (1982) has also observed additional resonances associated with f_{Qn} resonances (at either a higher or lower frequency). They are called subsidiary resonances and labelled as f_{Qn+} and f_{Qn-}. f_{Qn+} occurs at a slightly higher frequency and f_{Qn-} at a slightly lower frequency, than f_{Qn}. He did not find that f_{Qn+} and f_{Qn-} coexist on the same ionogram. The f_{Qn} resonances are often observed to 'float' away from the zero time delay baseline whereas the f_{Qn+} or f_{Qn-} subsidiary resonances are observed to be nonfloating.

6.2 Electron Bernstein Waves

Equation (3.64) is the dispersion relation for electrostatic waves. In this dispersion relation both electron and ion motion are involved. Since the electron plasma and cyclotron frequencies are much larger than the proton plasma and cyclotron frequencies ($\omega_{pp}/\omega_{pe} = \omega_{cp}/\omega_{ce} = m_e/m_p = 1/1837$), ion motion may be ignored, the ions then simply forming a neutralizing background, when the electron plasma waves are considered. Hence j in equation (3.64) only refers to electrons. Dropping j and summation for it, we get the dispersion relation for

electron electrostatic waves,

$$k_x^2 + k_z^2 + \frac{\omega_p^2 m e^{-\lambda}}{\kappa T_{\|}} \sum_{n=-\infty}^{\infty} I_n(\lambda)\Bigg\{1+ i\left[\alpha_n - \frac{n\omega_c}{k_z}\left(\frac{m}{2\kappa T_{\|}}\right)^{1/2}\frac{T_{\|}}{T_{\perp}}\right]F_0(\alpha_n)\Bigg\} = 0 \tag{6.4}$$

This dispersion relation may be reduced further by the certain approximations. For example, $F_0(\alpha_n)$ for $|\alpha_n| \gg 1$ may be given by

$$F_0(\alpha_n) = \sqrt{\pi}\frac{k_z}{|k_z|}exp(-\alpha_n^2) + \frac{i}{\alpha_n}\left(1 + \frac{1}{2\alpha_n^2} + \frac{3}{4\alpha_n^4} + \cdots\right) \approx \frac{i}{\alpha_n} \tag{6.5}$$

Using (6.5), (6.4) becomes

$$k_x^2 + k_z^2 + \frac{\omega_p^2 m e^{-\lambda}}{\kappa T_{\perp}} \sum_{n=-\infty}^{\infty} I_n(\lambda)\frac{n\omega_c}{\omega + n\omega_c} = 0 \tag{6.6}$$

For perpendicular propagation, $k_z = 0$, (6.6) may be written as

$$1 + \frac{\omega_p^2}{\omega_c}\frac{e^{-\lambda}}{\lambda}\sum_{n=-\infty}^{\infty}\frac{nI_n(\lambda)}{\omega + n\omega_c} = 0 \tag{6.7}$$

or

$$1 - \frac{\omega_p^2}{\omega_c}\frac{e^{-\lambda}}{\lambda}\sum_{n=-\infty}^{\infty}\frac{nI_n(\lambda)}{\omega - n\omega_c} = 0 \tag{6.8}$$

Equation (6.8) is the same equation used by Dougherty and Monaghan (Eq. 8.6, p.228, 1966). If we make use of the symmetry

$$I_n(\lambda) = I_{-n}(\lambda) \qquad n \text{ integral} \tag{6.9}$$

Eq. (6.8) may be written (McAfee, 1973)

$$1 - 2\omega_p^2 e^{-\lambda}\sum_{n=1}^{\infty}\frac{I_n(\lambda)}{\lambda}\frac{n^2}{(\omega^2 - n^2\omega_c^2)} = 0 \tag{6.10}$$

or (Stix, 1962)

$$k_x^2 = \frac{\omega_p^2 m}{\kappa T_{\perp}}\alpha(q,\lambda) \tag{6.11}$$

with

$$\alpha(q,\lambda) = -2\sum_{n=1}^{\infty} e^{-\lambda} I_n(\lambda) \frac{n^2}{n^2 - q^2}$$
$$q = \frac{\omega}{\omega_c}$$

In the above derivations, the full set of Maxwell equations is employed, the elements of the mobility tensor and the equivalent dieletric tensor are derived, and then the electrostatic assumption is made to obtain the dispersion relations (6.8) or (6.10) or (6.11). Alternatively, Crawford (1965) made an electrostatic approximation at the outset and only Poisson's equation was used. This allowed him to work with scalar quantities. He obtained the same results as Stix and McAfee. The dispersion relation obtained by Crawford may be written as

$$1 = \frac{\omega_p^2}{\omega_c^2} \sum_{n=1}^{\infty} \frac{e^{-\lambda} I_n(\lambda)}{\left(\frac{\lambda}{2}\right)\left[\left(\frac{\omega}{n\omega_c}\right)^2 - 1\right]} \tag{6.12}$$

Bernstein (1958) solved the Vlasov-Maxwell set of equations, by the Laplace transform method initiated by Landau (1946), including a static magnetic field $\mathbf{B}_0$. The full set of Maxwell equation was employed. He found the dispersion relation for waves propagating perpendicular to the magnetic field without Landau damping, which have become known as the Bernstein waves. If we set $s = i\omega$, the dispersion relation obtained by Bernstein (Eq. (46) in his paper) can be written as

$$1 + k_x^2 \lambda_D^2 = \omega e^{-\lambda} \sum_{n=-\infty}^{\infty} \frac{I_n(\lambda)}{\omega - n\omega_c}$$
$$= e^{-\lambda}\left[I_0(\lambda) + 2\omega^2 \sum_{n=1}^{\infty} \frac{I_n(\lambda)}{\omega^2 - n^2\omega_c^2}\right] \tag{6.13}$$

where $\lambda_D = \left(\kappa T/m\omega_p^2\right)^{1/2}$ is the Debye length.

We make use of the Bessel function identity

$$e^{\lambda cos\omega_c^{\tau}} = \sum_{n=-\infty}^{\infty} I_n(\lambda) e^{in\omega\tau} \tag{6.14}$$

When we set $\tau = 0$, then we may obtain

$$e^{-\lambda} \sum_{n=-\infty}^{\infty} I_n(\lambda) = 1 \tag{6.15}$$

Making use of (6.15), and noting $k_x^2 \lambda_D^2 = \lambda \omega_c^2 / \omega_p^2$, (6.13) can be written as

$$\begin{aligned} \frac{\lambda\omega_c^2}{\omega_p^2} + e^{-\lambda} \sum_{n=-\infty}^{\infty} I_n(\lambda) - \omega e^{-\lambda} \sum_{n=-\infty}^{\infty} \frac{I_n(\lambda)}{\omega - n\omega_c} &= \\ \frac{\lambda\omega_c^2}{\omega_p^2} + \sum_{n=-\infty}^{\infty} I_n(\lambda) e^{-\lambda} \left(1 - \frac{\omega}{\omega - n\omega_c}\right) &= \\ \frac{\lambda\omega_c^2}{\omega_p^2} - \sum_{n=-\infty}^{\infty} I_n(\lambda) e^{-\lambda} \left(\frac{n\omega_c}{\omega - n\omega_c}\right) &= 0 \end{aligned} \tag{6.16}$$

then we can obtain

$$1 - \frac{\omega_p^2}{\omega_c} \frac{e^{-\lambda}}{\lambda} \sum_{n=-\infty}^{\infty} \frac{n I_n(\lambda)}{\omega - n\omega_c} = 0 \tag{6.17}$$

which is Eq. (6.8). Hence Stix (1962), Crawford (1965), Dougherty and Monaghan (1966), and McAfee (1973) obtained the Bernstein's result in various approaches. Here I would like to point out that Stix and McAfee assumed the background distribution function of electrons is Maxwellian across the magnetic field and shift-Maxwellian along the magnetic field, while Bernstein, Crawford, and Dougherty and Monaghan employed an isotropic Maxwellian electron distribution function. However they all obtained the same results for the dispersion relation of electron Bernstein waves.

6.3 f_{Qn} Resonances

Let us look for solutions of Eq. (6.8) near the harmonics of the cyclotron frequency. We assume $\omega = N\omega_c(1+\delta)$ where $|\delta| \ll 1$ and N is a particular integer. Thus ω is close to a cyclotron harmonic angular frequency and we drop all terms in the series of Eq. (6.8) except the N^{th}. Solving (6.8) for δ gives

$$\delta = \frac{e^{-\lambda} I_N(\lambda)}{\lambda} \left(\frac{\omega_p}{\omega_c}\right)^2 \tag{6.18}$$

and hence we get

$$\omega = N\omega_c \left[1 + \frac{e^{-\lambda} I_N(\lambda)}{\lambda} \left(\frac{\omega_p}{\omega_c}\right)^2\right] \tag{6.19}$$

Dougherty and Monaghan (1966) obtained a similar formula to (6.19) (see Eq. (6.1)). We can see from (6.18) that δ is always positive. Hence ω is always greater than each cyclotron harmonic frequency.

Crawford (1965) has solved the dispersion equation (6.12) for various values of ω_p^2/ω_c^2. Plots of the solutions are shown in Fig. 6.1. From Fig. 6.1 we can see that the group velocity $v_g = d\omega/dk = 0$ or is small at the three points: (1) $k = 0$; (2) $k = \infty$; (3) k finite and nonzero. At $k = 0$ we get $\omega = n\omega_c$ except the fundamental (n=2,3,...). At $k = \infty$ we get $\omega = n\omega_c$ again, but including the fundamental (n=1,2,...). At k finite and nonzero, zero group velocity occurs at the upper limiting frequency of the pass band. In this case we get $n\omega_c < \omega < (n+1)\omega_c$. Here we are only concerned with the k finite and nonzero case. The above theoretical predictions were first identified on Alouette II topside ionograms by Warren and Hagg (1968). They called them f_{Qn} resonances.

6.4 Observations of Proton Cyclotron Echoes at f_{Qn} Resonances

In the previous two section we have discussed the f_{Qn} resonances. Here we will present the proton cyclotron echoes which occur at the f_{Qn} resonances on topside sounder ionograms. The ionograms were obtained from the ISIS II satellite at the ground station in Santiago (SNT, 33.1°S, 70.7°W).

Figure 6.2 shows a typical example of the proton cyclotron echoes which occur at the f_{Qn} resonances. The ionogram was taken on 15 May 1972 at 1653:23 UT when the satellite was located at 9.6°S, 78.9°W geographic coordinates and 1363 km altitude. The dip angle was 5°. A number of features are clear from this figure. The regular proton cyclotron echo observed and studied previously is at

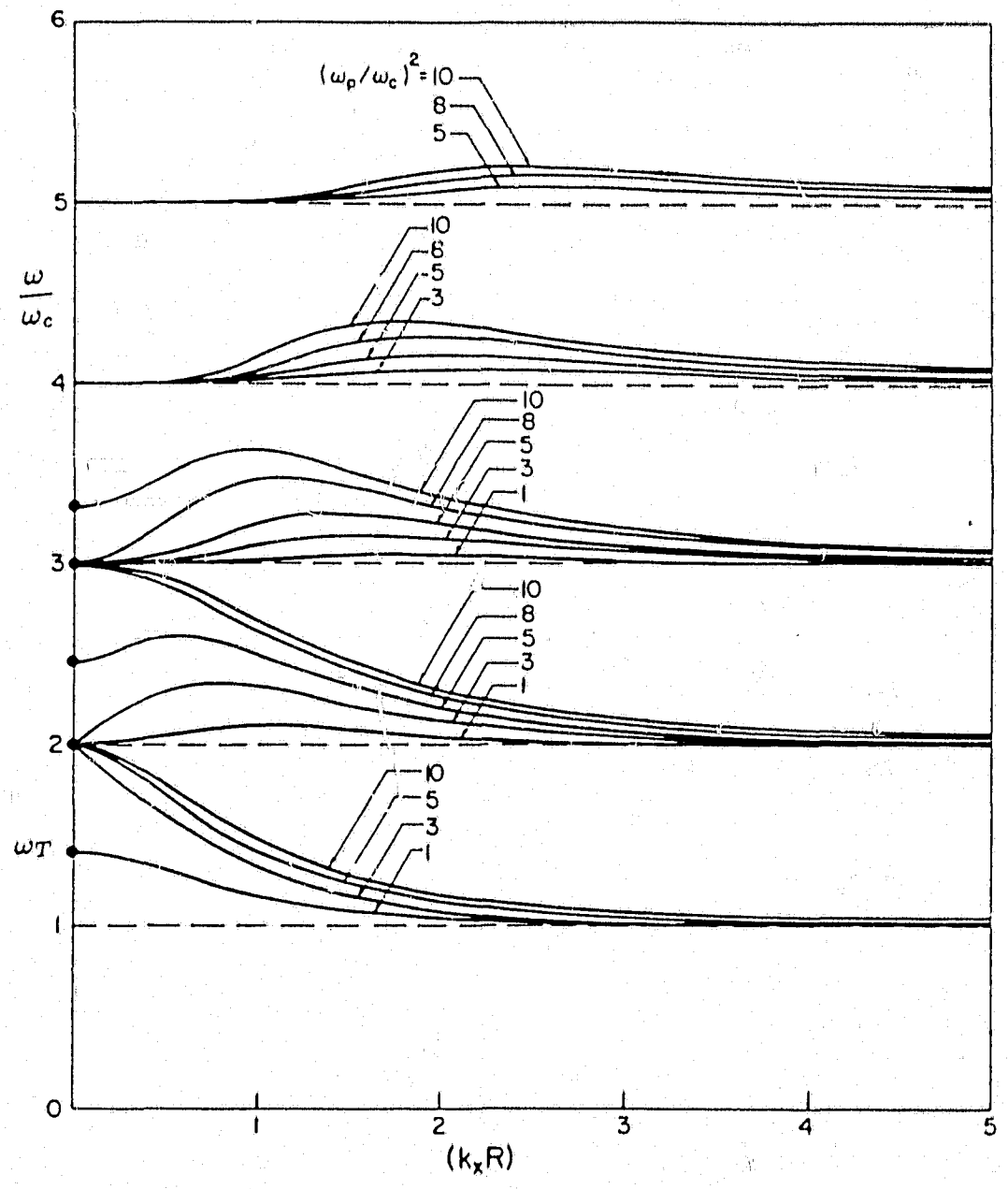

Figure 6.1: Electron Bernstein wave dispersion relation. Modified from Crawford (1965).

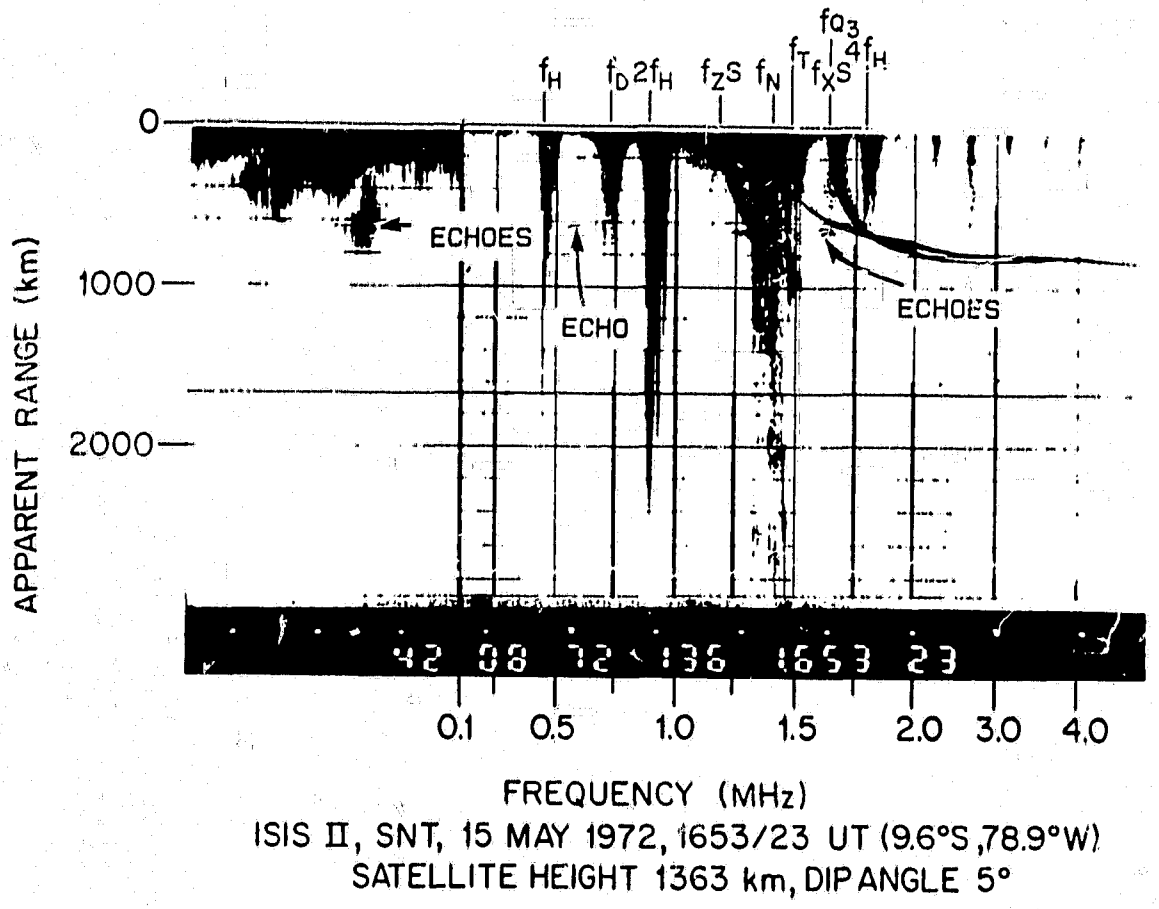

Figure 6.2: A typical example of proton cyclotron echoes which occur at the f_{Q3} resonance on an ISIS II ionogram taken at 1653:23 UT on May 15, 1972, at the ground telemetry station in Santiago (SNT, 33.1°S, 70.7°W) when the satellite was located at 9.6°S, 78.9°W geographic coordinates and 1363 km altitude, and the dip angle was 5°. The f_{Q3} resonance appears at frequencies from 1.61 to 1.69 MHz and extends from zero to about 700 km apparent range. The proton cyclotron echoes which occur at the f_{Q3} resonance are double: the weaker one occurs at about 641 km apparent range with the stronger one at 664 km apparent range. Also the regular proton cyclotron echo is shown at an apparent range of about 626 km at frequencies between the f_H and f_D resonances and double proton cyclotron echoes occur on the fixed-frequency (0.48 MHz) ionogram at apparent ranges of about 634 km and 660 km respectively.

an apparent range of about 626 km at frequencies between the f_H (0.45 MHz) and f_D resonances. The related apparent range corresponding to the calculated proton cyclotron period, which is derived from the electron cyclotron resonance frequency, is 609 km.

A very important new phenomenon in this figure is that a proton cyclotron echo occurs at the f_{Q3} resonance. The f_{Q3} resonance appears at frequencies from 1.61 to 1.69 MHz. The f_{Q3} resonance extends from zero apparent range to about 700 km apparent range. This denotes the received signals can persist for about 4.7 ms after the termination of the transmitter pulse of the sounder. Also we can see that the proton cyclotron echoes which occur at the f_{Q3} resonance are double: the weaker one occurs at about 641 km apparent range with the stronger one at 664 km apparent range. Double proton cyclotron echoes also occur on the fixed-frequency (0.48 MHz) ionogram at apparent ranges of about 634 km and 660 km respectively. The fixed frequency (0.48 MHz) is very close to f_H and, therefore, these echoes are probably located at the f_H resonance. A spur is observed on the f_N spike at about 650 km apparent range.

Figure 6.3 shows another example which displays very similar features to those in Figure 6.2. The ionogram was obtained 71 s later, and the satellite was located at 13.4°S, 79.0°W geographic coordinates with 1364 km altitude. The dip angle was −2°. Figure 6.4 gives a good example of the proton cyclotron echoes, which occur at the f_{Q3} resonance too. This ionogram was taken just 13 s after the one shown in Fig. 6.2. The satellite was located at 10.5°S, 78.9°W geographic coordinates and 1364 km altitude. The dip angle was 3°. This ionogram shows almost an identical case of the proton cyclotron echoes on the f_{Q3} resonance with that in Fig. 6.2. However, the regular proton cyclotron echo appears in a wide frequency range, starting at about 0.1 MHz, across the f_H and f_D spikes, and approaching $2f_H$ (0.9 MHz), and a stronger spur is attached to the f_N spike. Figure 6.5 shows an ionogram taken on 18 May 1972 at 1653:45

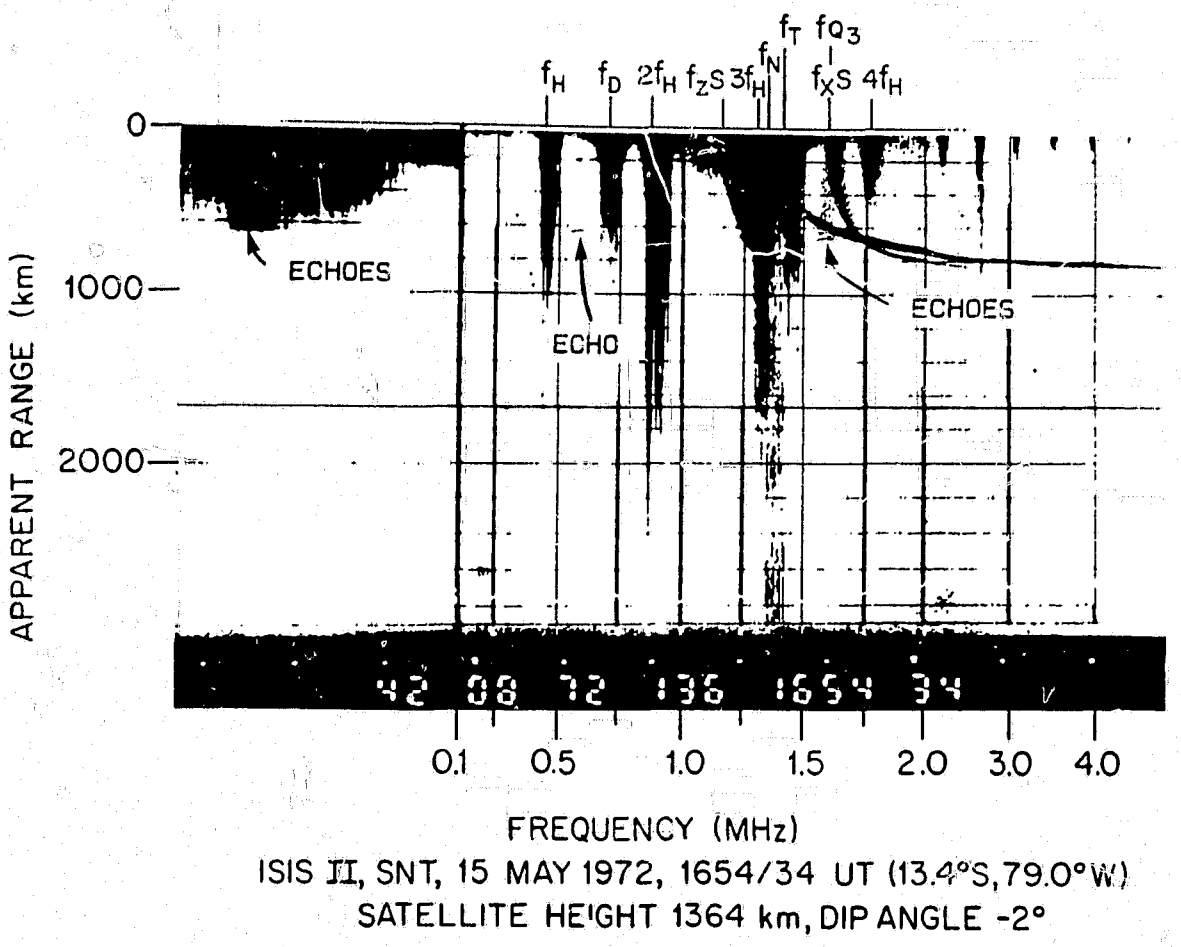

Figure 6.3: Proton cyclotron echoes at the f_{Q3} resonance were observed on an ionogram obtained 71 s following the one shown in Figure 6.2. The satellite was located at 13.4°S, 79.0°W geographic coordinates and 1364 km altitude, and the dip angle was −2°.

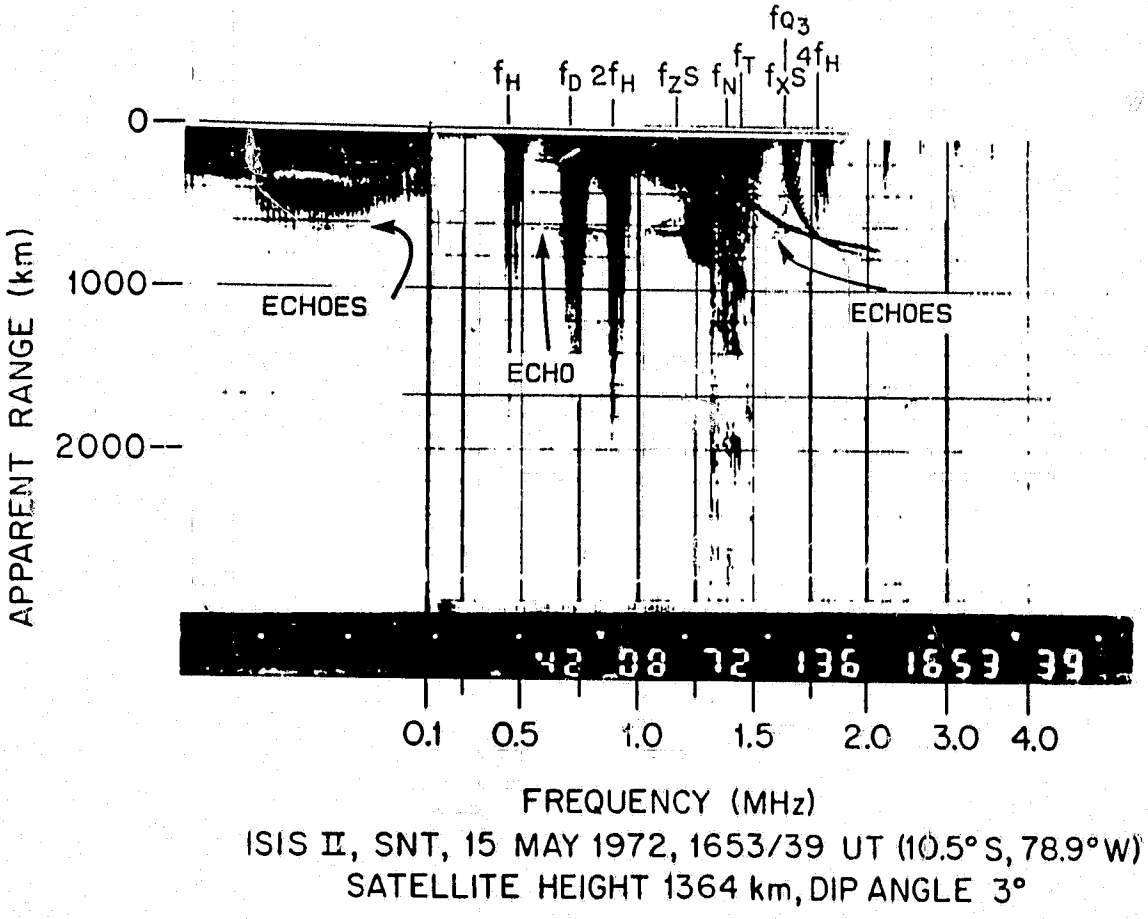

Figure 6.4: Proton cyclotron echoes at the f_{Q3} resonance on an ionogram taken just 16 s later after the one shown in Figure 6.2. The satellite was located at $10.5°S$, $78.9°W$ geographic coordinates and 1364 km altitude, and the dip angle was 3°. Proton cyclotron echoes at the f_{Q3} resonance similar to the ones shown in Figure 6.2 are observed. However, the regular proton cyclotron echo extends over a wide frequency range, starting at 0.1 MHz, across f_H and f_D (i.e., f_{D1}) resonances, and approaching $2f_H$ (0.9 MHz), and a stronger spur is attached to the f_N resonance.

UT when the satellite was located at $12.2°S$, $82.3°W$ geographic coordinates and 1363 km altitude. The dip angle was $-1°$. The regular proton cyclotron echo is at an apparent range of about 626 km at frequencies between f_H and f_D resonances. The proton cyclotron echoes occur on the f_{Q3} resonance. Also the proton cyclotron echoes on the f_{Q3} resonance are double. This time, however, the weaker echo occurs at about 671 km apparent range while the stronger one is at about 647 km apparent range. The stronger echo has a smaller apparent range in Figure 6.5 and a larger apparent range in Figure 6.2.

Figure 6.6 shows an ionogram exhibiting proton cyclotron echoes at both the f_{Q3} resonance and the $4f_H$ resonance. This ionogram was obtained about 68 s after the one shown in Figure 6.5. The dip angle was $-7°$. The proton cyclotron echoes at $3f_H$ and $4f_H$ have been discussed already (Chen and Horita, 1991). Here we only point out that the proton cyclotron echoes at the $4f_H$ resonance are also double. In this example the stronger echo occurs at about 636 km apparent range with the weaker one at about 657 km apparent range. For the proton cyclotron echoes at the f_{Q3} resonance, the stronger one has an apparent range of about 648 km with the weaker one at an apparent range of about 672 km. The apparent ranges of the corresponding proton cyclotron echoes at the f_{Q3} resonance are larger than the ones at the $4f_H$ resonance. The stronger echoes have smaller apparent ranges at both the f_{Q3} resonance and the $4f_H$ resonance. The regular proton cyclotron echo occurs at an apparent range of about 636 km at frequencies from f_H to f_N, across the diffuse resonance f_D. The proton cyclotron echo seems to link to the spur together.

All data of proton cyclotron echoes scaled from Figures 6.2 - 6.6 are summarized in Tables 1 and 2. R_{calc} and R_{regu} refer to apparent ranges of the calculated and regular proton cyclotron echoes, respectively, and R_1 and R_2 to apparent ranges of the double echoes. Their units in Table 1 are km. They are normalized by R_{regu} in Table 2. We also put the scaled data of the proton cyclotron echoes,

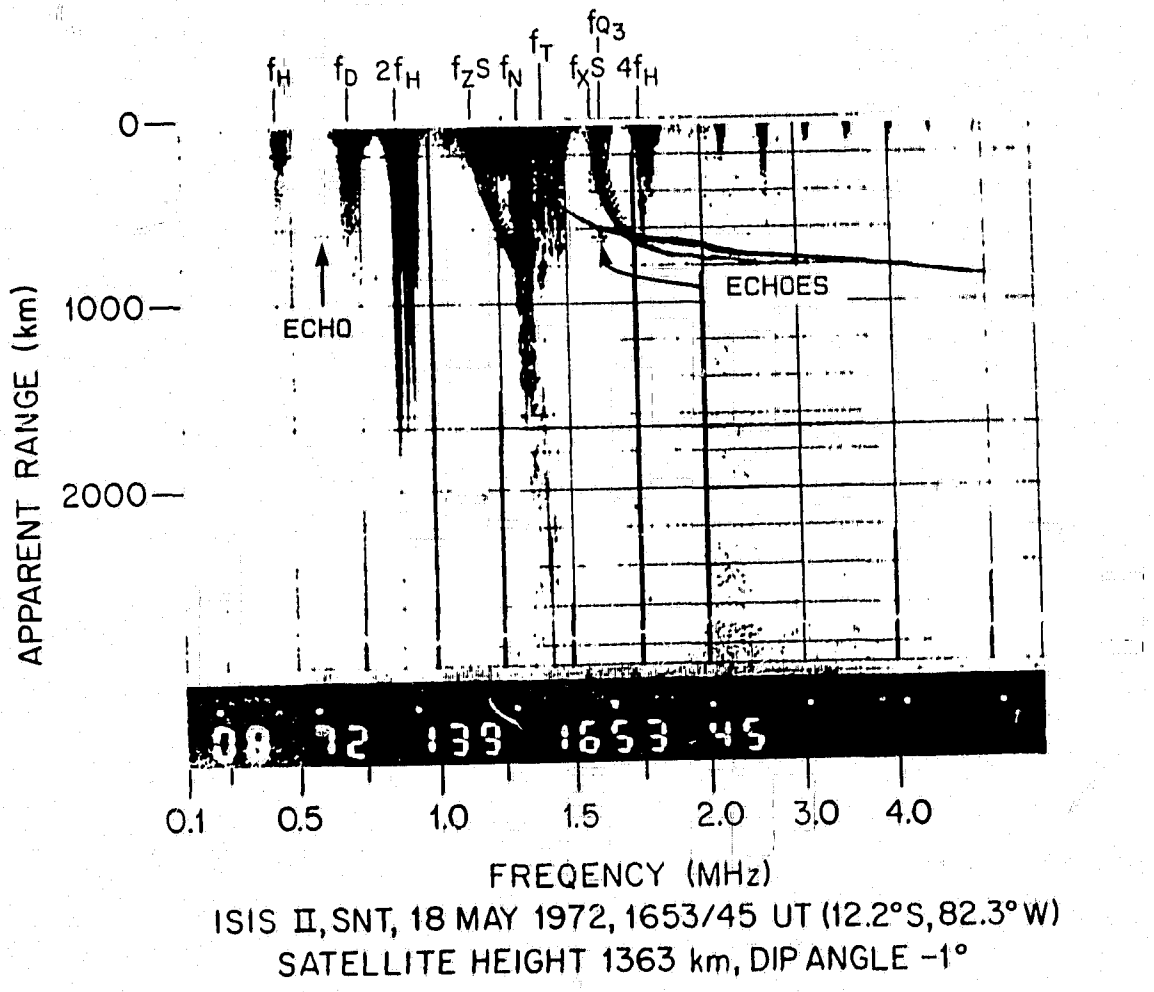

Figure 6.5: Proton cyclotron echoes at the f_{Q3} resonance on an ISIS II ionogram taken at 1653:45 UT on May 18, 1972 at the telemetry ground station in Santiago when the satellite was located at $12.2°S$, $82.3°W$ geographic coordinates and 1363 km altitude, and the dip angle was $-1°$. The proton cyclotron echo on the f_{Q3} resonance in this instance is different from the previous examples since the weaker echo now occurs at about 671 km apparent range below the stronger one at about 647 km apparent range. The regular proton cyclotron echo is at an apparent range of about 633 km at frequencies between f_H and f_D resonances.

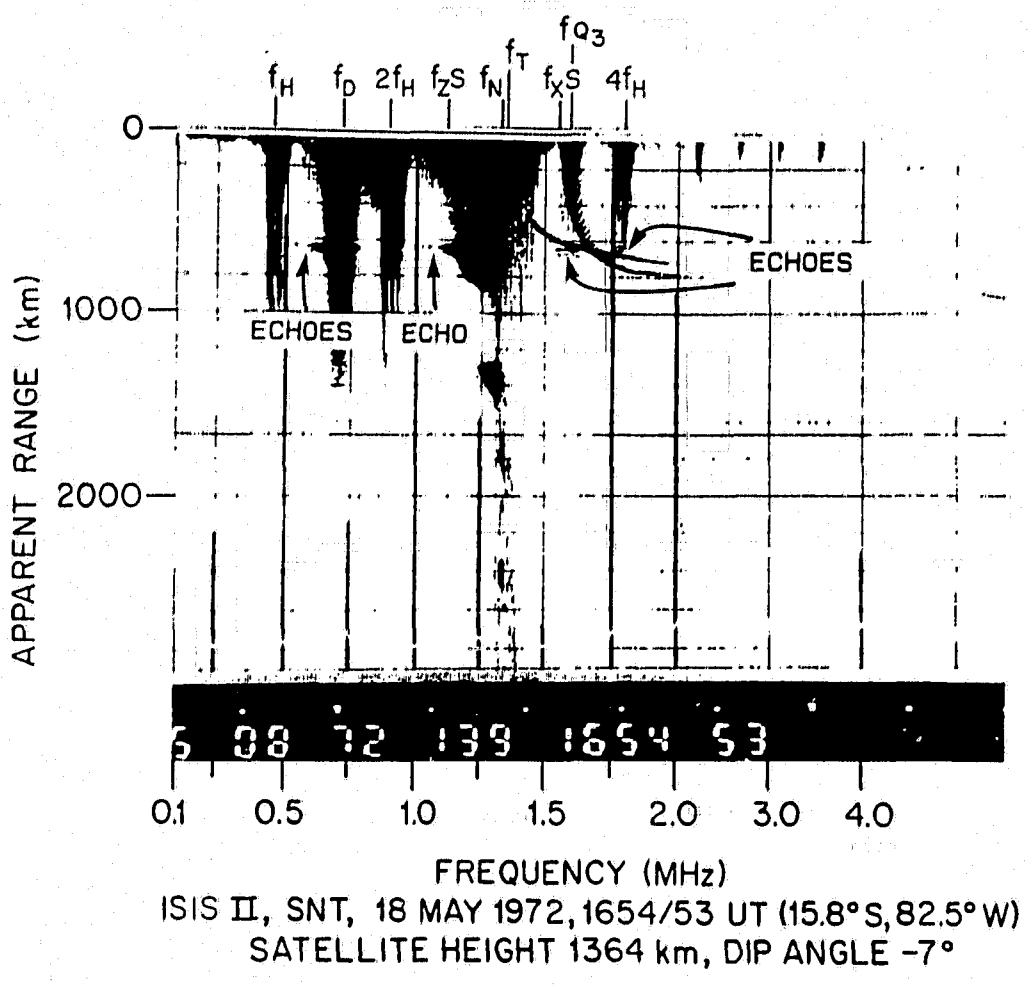

Figure 6.6: Proton cyclotron echoes located at both the f_{Q3} resonance and $4f_H$ resonance on an ionogram obtained 68 s following the one shown in Figure 6.5. The satellite was located at $15.8°S$, $82.5°W$ geographic coordinates, and 1364 km altitude, and the dip angle was $-7°$. Both proton cyclotron echoes at the f_{Q3} resonance and the $4f_H$ resonance are double. For the proton cyclotron echoes at the $4f_H$ resonance, the stronger echo occurs at about 636 km apparent range with the weaker one at about 657 km apparent range; for the proton cyclotron echoes at the f_{Q3} resonance, the stronger echo has an apparent range of about 648 km with the weaker one at an apparent range of about 672 km. The apparent ranges of the corresponding proton cyclotron echoes at the f_{Q3} resonance are larger than the ones at the $4f_H$ resonance. The stronger echoes at both the f_{Q3} resonance and the $4f_H$ resonance have smaller apparent ranges than the weaker ones, respectively. The regular proton cyclotron echo occurs at an apparent range of about 636 km at frequencies from f_H to f_N, and seems to link to the spur.

Figures	R_{calc}	R_{regu}	f_{Q3}		f_H		$4f_H$		f_D	
			R_1	R_2	R_1	R_2	R_1	R_2	R_1	R_2
Figure 6.2	609	626	641	664	634	660				
Figure 6.3	622	636	648	662	634	655				
Figure 6.4	615	626	642	660	626	646			628	655
Figure 6.5	611	626	647	671						
Figure 6.6	619	636	648	672			636	657	636	664

Table 6.1: Data of proton cyclotron echoes scaled from Figures 6.2 - 6.6

Figures	R_{calc}	R_{regu}	f_{Q3}		f_H		$4f_H$		f_D	
			R_1	R_2	R_1	R_2	R_1	R_2	R_1	R_2
Figure 6.2	0.97	1.00	1.02	1.06	1.01	1.05				
Figure 6.3	0.98	1.00	1.02	1.04	1.00	1.03				
Figure 6.4	0.98	1.00	1.02	1.05	1.00	1.03			1.00	1.05
Figure 6.5	0.98	1.00	1.02	1.05						
Figure 6.6	0.97	1.00	1.02	1.06			1.00	1.03	1.00	1.04

Table 6.2: Data of proton cyclotron echoes normalized by R_{regu}

which we observed at the f_D resonance, in Tables 1 and 2. From the Tables, especially, Table 2, we can see that apparent ranges of all proton cyclotron echoes are greater than apparent ranges of their corresponding calculated proton cyclotron echoes and apparent ranges of regular proton cyclotron echoes are very close or equal to apparent ranges (R_1) of the first echoes of their corresponding double proton cyclotron echoes, and therefore the regular proton cyclotron echo is probably corresponding the first echo of the double echoes.

It has been shown (Hamelin, 1980; Pottelette *et al.*, 1981; Belmont, 1981; Etcheto *et al.*, 1983; Trotignon *et al.*, 1986) that when the electrons of the plasma can be described by a Maxwellian distribution, the values of f_{Qn} (normalized to the electron cyclotron frequency f_H) only depend on the ratio of the electron plasma frequency to the electron cyclotron frequency f_N/f_H. It is therefore possible to use a diagram on which is displayed f_{Qn}/f_H as a function of f_N/f_H. Hamelin (Hamelin, 1980; Pottelette *et al.*, 1981) has introduced such a diagram

(e.g. Figure 6.7, which is then called the Hamelin diagram. We have plotted the f_{Q3} resonances, on which the proton cyclotron echoes occur, in Figures 6.2, 6.3, 6.5 and 6.6 on the Hamelin diagram with their error bars. They show a good accuracy with theory.

It has also been shown (Belmont, 1981; Etcheto *et al.*, 1983; Trotignon *et al.*, 1986) that in a bi-Maxwellian plasma (made of a dominant cold plus a hot population) there is a series of f_{Qn} (one in each branch between two successive electron cyclotron harmonics above the upper hybrid frequency) which only depend on the parameters of the cold population. Additional f_{Qn} resonances, called "hot f_{Qn}", depend on the characteristics of hot plasma. We have observed the double proton cyclotron echoes on f_{Qn} resonances. However, they do not seem to relate to these because their frequency differences are quite different.

6.5 Summary

In this chapter, we have reviewed the dispersion relations of electron Bernstein waves and previous studies of the f_{Qn} resonances. Then we have presented our discovery that the proton cyclotron echoes on the f_{Q3} resonances have been observed on topside sounder ionograms from the ISIS II satellite. All the above examples occur at locations where the dip angle magnitude is less than 8°. All the proton cyclotron echoes at f_{Q3}, and also at f_H, $4f_H$ and f_D are double, whereas the regular proton cyclotron echo is a single trace. The single regular proton cyclotron echo seems to correspond to the first echo of the double proton cyclotron echoes. The apparent ranges of all proton cyclotron echoes are greater than the corresponding apparent ranges calculated from the proton cyclotron period at the satellite locations, which are derived from the electron cyclotron resonance frequencies.

So far we have only observed the proton cyclotron echoes which occur at

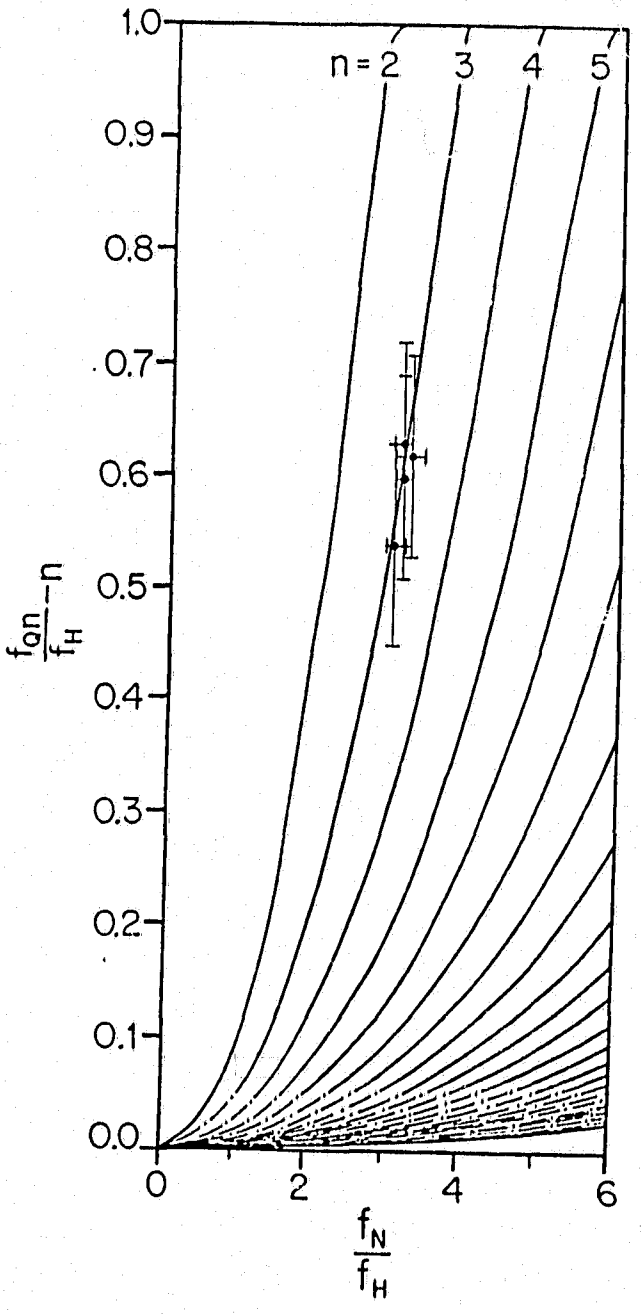

Figure 6.7: Observed f_{Qn} resonances with proton cyclotron echoes displayed on a Hamelin diagram. The ordinate determines the decimal part of f_{Qn}/f_H while its integer part is determined by the number n of each curve. The abscissa shows the ratio of f_N/f_H. The Hamelin diagram is modified from Belmont (1981).

the f_{Q3} resonances among the f_{Qn} resonances. This is probably because the f_{Q3} occurs most frequently, the f_{Q2} less frequently, and the f_{Q4}, f_{Q5}, f_{Q6} very seldom. However, there are good reasons to believe that the proton cyclotron echoes would occur at the other f_{Qn}, especially, f_{Q2} resonances if certain conditions were satisfied.

Chapter 7

Proton Cyclotron Echoes on f_H or nf_H Resonances

7.1 Introduction

There are two fundamental frequencies in magnetoplasmas, which are the electron cyclotron frequency

$$f_H = \frac{eB}{2\pi m_e} \tag{7.1}$$

and the electron plasma frequency

$$f_N = \frac{1}{2\pi}\left(\frac{n_e e^2}{m_e \varepsilon_0}\right)^{1/2} \tag{7.2}$$

Most resonances which appear on topside sounder ionograms are associated with these two fundamental frequencies. They are the plasma resonance which occurs at f_N, the cyclotron resonance at f_H, the harmonic cyclotron resonances at nf_H (n=2, 3, $\cdots$), and the upper hybrid resonance at $f_T = (f_N^2 + f_H^2)^{1/2}$. The above resonances are called the principal resonances, for they are consistently observed by the topside sounders. In addition, there are two other series of resonances. They are the f_{Qn} resonances and the diffuse resonances f_{Dn}. The f_{Qn} resonances occur above f_T between nf_H and $(n+1)f_H$ ($n = 2, 3, \cdots$), while the diffuse resonances occur below f_T between nf_H and $(n+1)f_H$ ($n = 1, 2, \cdots$).

Over 30 years since the initial observations of plasma resonances from rocket- and satellite-borne topside sounders (Knecht *et al.*, 1961, and Knecht and Russell, 1962, for the rocket observations; Lockwood, 1963, and Calvert and Goe, 1963, for the satellite observations), much has been learned about the above res-

onances respectively. Their studies have been described in papers, for example, by Fejer and Calvert (1964), Warren and Hagg (1968), Calvert (1969), Calvert and McAfee (1969), Oya (1970, 1971a), Andrews and Fang (1971), Dougherty and Watson (1971), Muldrew (1972a, b), McAfee (1973), Benson (1974), Bitoun *et al.* (1975), Benson (1977), Higel and de Feraudy (1977), Benson and Bitoun (1979), Kiwamoto and Benson (1979), Benson (1982), Osherovich (1987, 1989), and Osherovich and Benson (1991).

Proton cyclotron echoes were first reported by Matuura and Nishizaki in 1969 on Alouette II satellite topside sounder ionograms. Further studies were carried out by Horita (1974, 1987), Benson (1975), Ondoh *et al.* (1975), and Oya (1978). Chen and Horita (1991) have observed that proton cyclotron echoes occur on harmonic electron cyclotron resonances at the third and fourth harmonics of the electron cyclotron frequency. $3f_H$ and $4f_H$. In this Chapter we will approach this subject further.

7.2 Observations of the f_H and nf_H Resonances

Shortly after the launch of the Alouette I satellite, Lockwood (1963) first observed f_H and nf_H ($n > 1$) resonances on ionograms obtained from the Alouette I topside swept-frequency sounder. He called these resonances cyclotron spikes. He found that the observed spikes occur within less than 1% of integer multiples of the electron cyclotron frequency at the satellite location. An example of a swept-frequency ionogram that clearly illustrates f_H, nf_H and other resonances is shown in Figure 7.1. Calvert and Goe (1963) used the term 'resonances' to describe these phenomena. In addition to the f_H and nf_H resonances, they identified the resonances at f_N, f_T and $2f_T$. They made an extensive study of the distribution of these resonant frequencies as a function of geophysical latitude to assist in identification by examining sequences of topside ionograms recorded

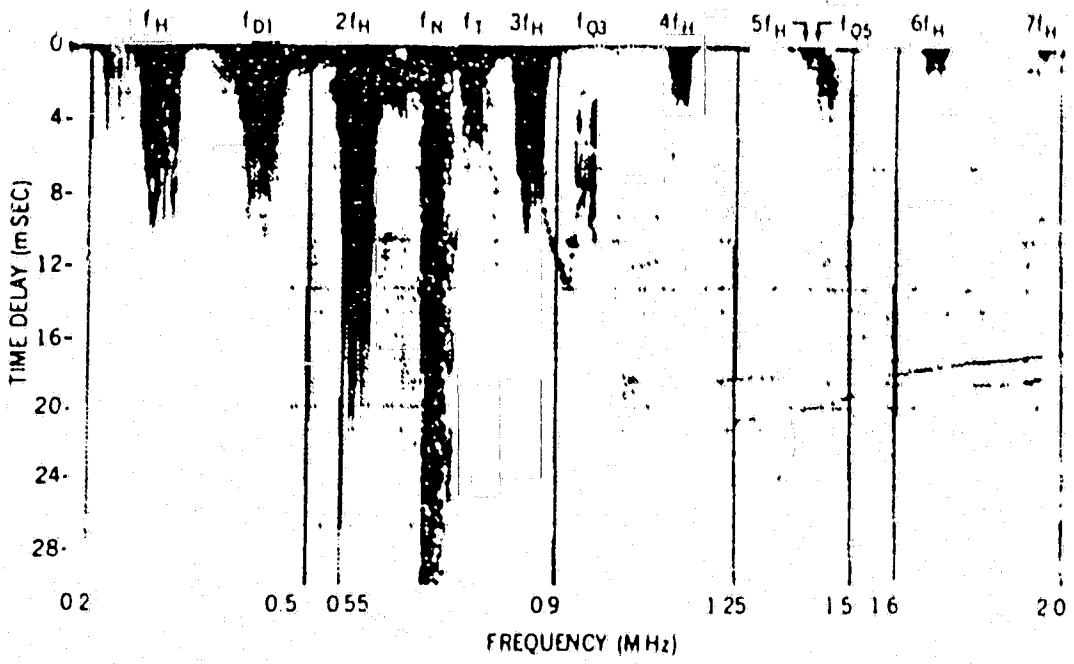

Figure 7.1: The high-resolution portion of an Alouette II ionogram recorded at the Quito Telemetry Station on May 4, 1967 (1214:22 UT; 25.2°S, 65.6°W, 2612 km in altitude). The heavy vertical traces, which are due to electrostatic waves of low group velocity in the vicinity of the sounder, are identified at the top of the ionogram; the weaker nonvertical traces are due to the ionospheric reflection of electromagnetic waves radiated by the sounder. After Benson (1977).

from Alouette I. This served to facilitate the distinction between resonances and to expose instrumental responses. Barrington and Herzberg (1966) found the nf_H on Alouette I ionograms to be within 1% of integral multiples of f_H obtained from model field calculations. Benson (1972) observed the actual frequency shift to be less than 0.2% on Alouette II ionograms from the the model field value. Higel *et al.* (1972) examined the actual received waveform of the resonance signal by a rocket-borne RF sounder experiment and indicated the nf_H resonances to be within less than 0.1% of the model field value. Cyclotron harmonics have been observed up to $22f_H$.

Lockwood (1965) studied the relationship between the occurrence of nf_H resonances and the antenna orientation to the earth's magnetic field. He observed that the number of cyclotron spikes occurring on an ionogram is a maximum when the sounding antenna is parallel to the earth's magnetic field. Calvert *et al.* (Calvert, Knecht and VanZandt, 1964; Calvert and VanZandt, 1966; Calvert and McAfee, 1969) found that on the ionograms of the fixed-frequency topside sounder aboard Explorer XX the harmonics of the electron cyclotron resonances were modulated both intensity and fringe pattern by the satellite spin. An example for $3f_H$ is given in Figure 7.2. Two patterns are shown; the one occurs when the antenna is parallel to the earth's magnetic field and it does not exhibit fringes while the other occurs when the antenna is perpendicular to the earth's magnetic field and it has modulated fringes. Stronger resonances and higher harmonics are observed when the antenna and the earth's magnetic field are aligned. The fundamental cyclotron resonance is not observed by Explorer XX because the sounding frequencies are too high. However Muldrew (1972b) presented a fringe pattern modulated by antenna orientation on f_H which occurred on an ISIS ionogram.

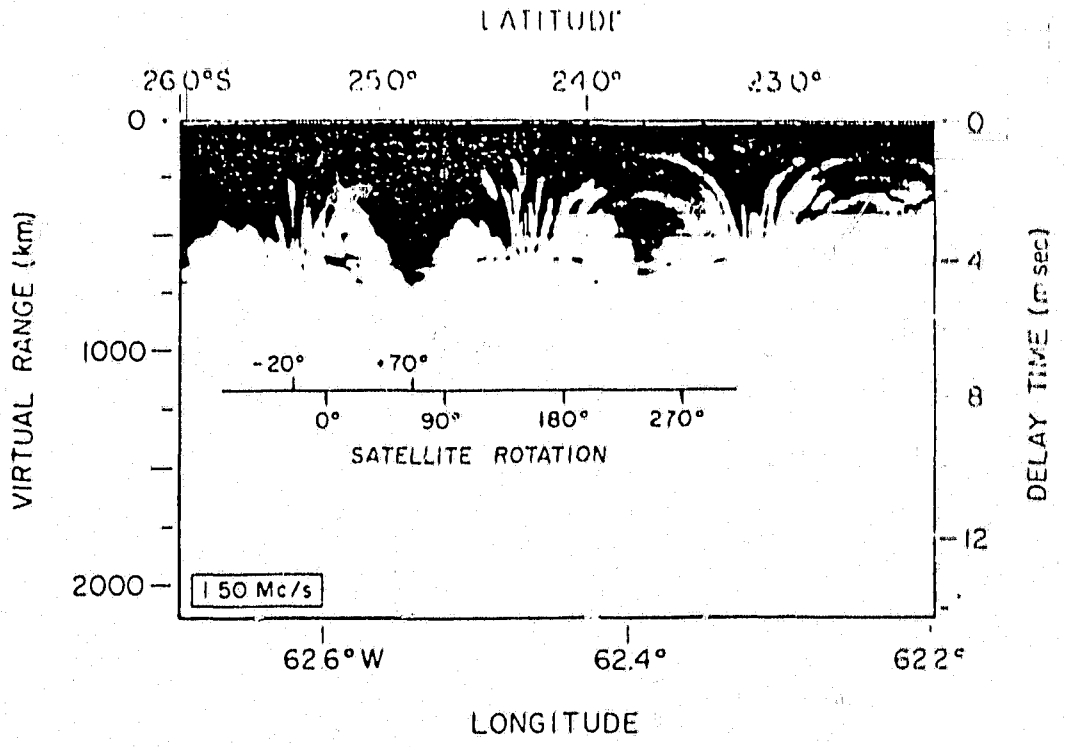

Figure 7.2: An Explorer XX fixed-frequency ionogram showing the modulation of the fringe pattern and antenna orientation effects at the $3f_H$ resonance (at $+70°$ the antenna is parallel to the earth's magnetic field and at $-20°$, perpendicular). After Calvert and VanZandt (1966).

7.3 Full-wave Dispersion Curves

In the electrostatic approximation, the waves in a hot magnetoplasma for $\theta = 0$ are unaffected by the ambient magnetic field, where θ is the angle between the propagation vector $\mathbf{k}$ and the ambient magnetic field $\mathbf{B}$. However as θ approaches $\pi/2$, new waves (the Bernstein modes) appear and as $\theta = \pi/2$ these waves are completely undamped. The dispersion curves given by *Crawford* (see Figure 6.1 on page 94) have shown that the group velocity equals zero or is small for the three cases. We have discussed the case for k finite and nonzero in detail, which leads to the f_{Qn} resonances. At $k \to 0$ the zero group velocity waves ($d\omega/dk \to 0$) occurs at $n\omega$, excluding $n = 1$. At $k \to \infty$ the zero group velocity waves again occur at $n\omega$, including $n = 1$. Thus the harmonics of the electron cyclotron waves with small or zero group velocity should be expected at both small and large k values. However, as $k \to 0$, the electrostatic approximation may not be valid (Stix, 1962; Swanson, 1989). The full-wave dispersion curves needed to be examined. The full wave dispersion relation has been given by equation (3.58).

Again we consider only electron motion and insert (3.41) into (3.56) with dropping j, we get the elements of $\mathbf{K}$ as follows

$$\begin{aligned}
K_{xx} &= 1 - i\frac{\omega_p^2}{\omega}\frac{e^{-\lambda}\kappa T_\perp}{mk_z}\sum_{n=-\infty}^{\infty}\frac{n^2}{\lambda}I_n[\langle\Theta\rangle_n] \\
K_{xy} &= i\frac{\omega_p^2}{\omega}\frac{e^{-\lambda}\kappa T_\perp}{mk_z}\sum_{n=-\infty}^{\infty} in(I_n - I_n')[\langle\Theta\rangle_n] \\
K_{xz} &= -i\frac{\omega_p^2}{\omega\omega_c}\frac{e^{-\lambda}\kappa T_\perp}{mk_z}\sum_{n=-\infty}^{\infty}\frac{nk_x}{\lambda}I_n[n\langle\Phi\rangle_n - \langle\Psi\rangle_n] \\
K_{yy} &= 1 - i\frac{\omega_p^2}{\omega}\frac{e^{-\lambda}\kappa T_\perp}{mk_z}\sum_{n=-\infty}^{\infty}\left(\frac{n^2}{\lambda}I_n + 2\lambda I_n - 2\lambda I_n'\right)[\langle\Theta\rangle_n] \qquad (7.3) \\
K_{yz} &= i\frac{\omega_p^2}{\omega\omega_c}\frac{e^{-\lambda}\kappa T_\perp}{mk_z}\sum_{n=-\infty}^{\infty} ik_x(I_n - I_n')[n\langle\Phi\rangle_n - \langle\Psi\rangle_n]
\end{aligned}$$

$$K_{zz} = -\frac{\omega e^{-\lambda}}{k_z} \sum_{n=-\infty}^{\infty} I_n[n\langle v_z\Phi\rangle_n - \langle v_z\Psi\rangle_n]$$

with the Onsager relation

$$\begin{aligned} K_{xy} &= -K_{yx} \\ K_{yz} &= -K_{zy} \\ K_{xz} &= K_{zx} \end{aligned} \tag{7.4}$$

In the case of $T_\perp = T_\parallel = T$ and no drift velocity, (3.42)-(3.50) become

$$\begin{aligned} \langle\Theta\rangle_n &= -2\left(\frac{m}{2\kappa T_\parallel}\right)^{3/2} F_0 \\ \langle v_z\Theta\rangle_n &= 2i\left(\frac{m}{2\kappa T}\right)(1+i\alpha_n F_0) \\ \langle\Phi\rangle_n &= 0 \\ \langle v_z\Phi\rangle_n &= 0 \\ \langle\Psi\rangle_n &= 2i\left(\frac{m}{2\kappa T}\right)(1+i\alpha F_0) \\ \langle v_z\Psi\rangle_n &= \frac{2i}{k_z}\left(\frac{m}{2\kappa T}\right)(\omega+n\omega)(1+i\alpha_n F_0) \\ F_0(\alpha_n) &= \sqrt{\pi}\frac{k_z}{|k_z|}exp(-\alpha_n^2) + 2iS(\alpha_n) \\ S(z) &= exp(-z^2)\int_0^z exp(t^2)dt \\ \alpha_n &= \frac{\omega+n\omega_c}{k_z}\left(\frac{m}{2\kappa T_\parallel}\right)^{1/2} \end{aligned} \tag{7.5}$$

when $\alpha_n \gg 1$, F_0 can take its approximate expression:

$$F_0 = \frac{i}{\alpha_n}\left(1+\frac{1}{2\alpha_n^2}+\frac{3}{4\alpha_n^4}+\frac{15}{8\alpha_n^6}\right) \tag{7.6}$$

Oya (1971b) carried out numerical computations for $T = 2000°K$ and various values of the plasma parameter q_N $(= \omega_N/\omega_H)$. The dispersion curves are presented in Figure 7.3 for various values of θ ranging from 0° to 90° and for $q_N = 1.6$. The left-hand side of the diagram ($kR < 5 \times 10^{-3}$) represents the

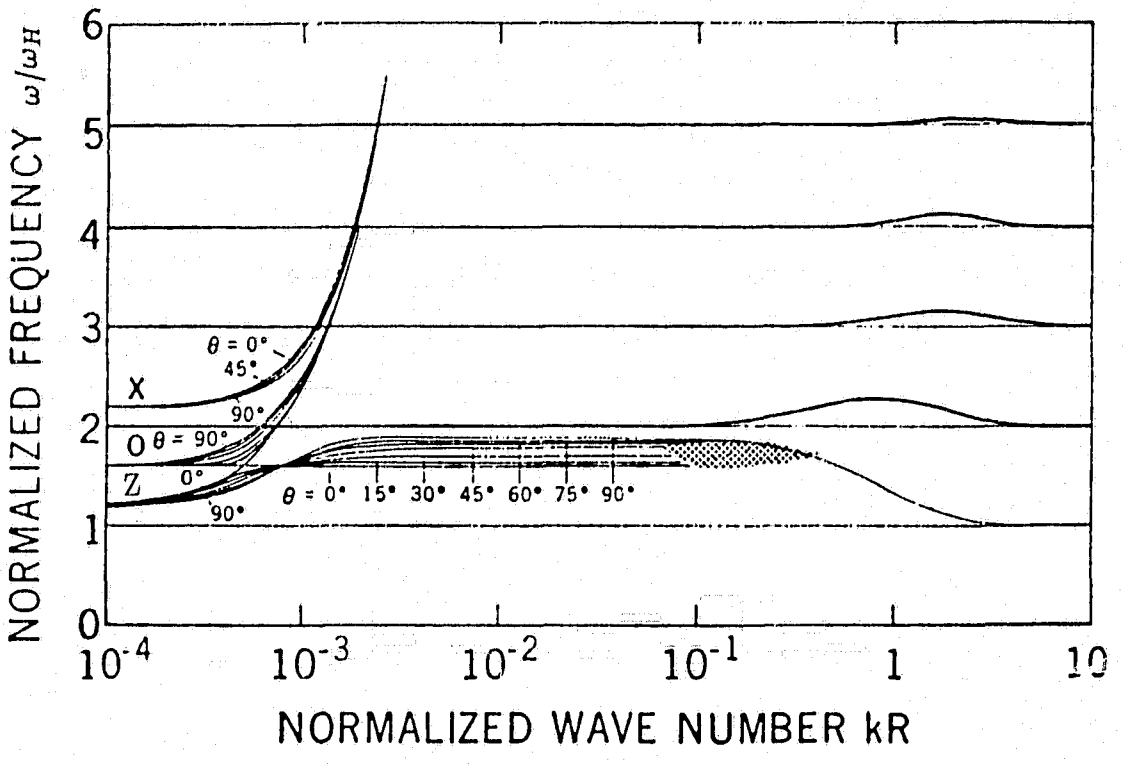

Figure 7.3: Normalized dispersion curves for the case where the electron thermal motions are included (but collisions neglected) with an ambient magnetic field. The angular frequency is normalized by the angular electron cyclotron frequency and the wave number is normalized by $1/R$ where $R = (\kappa T/m_e)^{1/2}/\omega_c$ is the electron cyclotron radius (κ, T, and m_e are Boltzmann's constant, the electron temperature, and the electron mass, respectively). The electromagnetic ordinary mode is designated by "O" while the extraordinary mode is designed by "X" (for the X branch) and "Z" (for the Z branch). The curves are presented for different angles θ of $\mathbf{k}$ relative to $\mathbf{B}$ except for the electrostatic Bernstein modes near the harmonics of $n\omega_H$ which are presented for $\theta = 90°$. Dotted area between $kR = 9 \times 10^{-2}$ and 4×10^{-1}, where $k = k_x/sin\theta$, indicates that the waves propagating in oblique directions are subject to damping. The diagram corresponds to the plasma conditions $f_N/f_H = 1.6$. After Oya (1971b).

electromagnetic waves while its right-hand side ($kR > 10^{-1}$) the Bernstein mode electrostatic waves. The intermediate wavelength region ($5 \times 10^{-3} \lesssim kR < 10^{-1}$) shows the connection between the electromagnetic Z wave and the electrostatic wave associated with the upper hybrid frequency (corresponding to $\theta = 90°$) and also shows the waves which are expected to occur at $n\omega_H$ ($n = 2, 3, \ldots$).

7.4 Explanations of the nf_H and f_H Resonances

Apart from identifying the resonant frequencies in terms of the dispersion relations, it is important to determine the mechanism whereby the energy remains in the vicinity of the antenna. Successive models have been progressively suggested.

At first, the f_H and nf_H resonances were attributed to the phase-bunching of electrons due to the nonuniform radiation field of the sounder antenna (Lockwood, 1963) or due to the nonuniform antenna sheath (Johnston and Nuttall, 1964). Shortly in addition to the f_H and nf_H resonances, the resonances at f_N and f_T were identified by Calvert and Goe (1963). They attributed the f_N and f_T resonances to the electron electrostatic oscillations along and across the earth's magnetic field, respectively. Fejer and Calvert (1964) attributed all the principal electron resonances (f_N, f_H, nf_H and f_T), which were consistently observed by the topside sounder, to electrostatic waves of near-zero group velocity. For this model, several possibilities were suggested. The first possibility was that the satellite moves through an excited volume of plasma, which is stationary (nonpropagating wave or standing wave) and the antennas take the energy from the excited plasma oscillations (Sturrock, 1965). The second possibility was that the group velocity of the slow electrostatic waves matches the velocity of the satellite. The energy in the waves tends to stay in the vicinity of the satellite with the decay of the resonance resulting from pulse spreading (Sturrock,

1965; Deering and Fejer, 1965; Shkarofsky, 1968; Andrews and Fang, 1971).

Neither a zero group velocity nor a matched group velocity could lead to a satisfactory explanation of the fringe patterns and also McAfee (1968, 1969a, 1969b, 1970) discovered that the electrostatic waves which initially match the satellite velocity near f_N would quickly be refracted away from the satellite due to the electron density gradient. The concept of the sounder stimulated electrostatic wave propagating away from the satellite and being reflected from a region near the satellite, returning to the satellite as an oblique echo was first introduced by McAfee (1968) for f_N and later for f_T (McAfee, 1969b). By ray tracing he found that these waves could be reflected and return to the satellite. The reflections are due to small changes in the electron density encountered by a wave propagating near f_N or f_T because of the extreme sensitivity of the dispersion relations to these small changes. Also it was found by McAfee (1968) that two types of waves are possible, corresponding to different orientation of the wave propagation vector. They are referred to as the forward wave and the backward wave respectively. At a given time the forward and backward waves will have slightly different frequencies (due to Doppler shift) and may be expected to result in the two waves adding to give a 'beating' to produce the observed fringe pattern. Bitoun *et al.* (1970) obtained similar results for the f_T resonance.

Andrews and Fang (1971) suggested that the oblique echo reflection mechanism for the f_N and f_T resonances may also be applied to the the harmonics nf_H of the electron cyclotron resonance. The first nf_H resonance to be interpreted in the oblique echo reflection mechanism was for $n = 3$ corresponding to Alouette II observations by Muldrew (1972b) using numerical ray tracing and later by Bitoun (1974) using analytical ray tracing. They found that the reflections for the nf_H wave were due to the small changes in the magnetic field strength rather than in the electron density. They showed that the ray paths

for $3f_H$ wave are approximately parabolic trajectories. The group velocity $\mathbf{v}_g$ is nearly perpendicular to the phase velocity $\mathbf{v}_p$, i.e., to the direction of propagation vector $\mathbf{k}$, except near reflection. Since $\mathbf{k}$ is nearly perpendicular to the magnetic field $\mathbf{B}$ for nf_H waves, the ray paths are elongated nearly parallel to $\mathbf{B}$. The analytical ray tracing approach was used to explain nf_H resonances observed at $n = 2$, 3, 4, and 5 by a rocket-borne sounder (Bitoun *et al.*, 1975) and to explain the Alouette I satellite observations (Benson and Bitoun, 1979). Benson and Bitoun indicate that the long duration nf_H resonances observed by the Alouette satellite (except $n = 2$), i.e. with $n = 3$, and 4, can well be explained by the analytical oblique echo theory. The $n = 2$ resonances observed by the satellite cannot be explained by the analytical oblique echo theory due to their long durations. This is in conflict with the conclusion of Bitoun *et al.* (1975) where the resonances were observed by the sounder operating at a lower peak-power and at a lower altitude. Also Benson (1977) points out that the nf_H resonances of $n \geq 5$ had time durations much less than the time required for the satellite to move a distance about antenna's length. Thus for high n resonances the wave velocity- satellite velocity matching is preferable to the wave reflection process.

The oblique echo theory for electrostatic waves has been well developed. Most resonances can be interpreted in terms of the reception of the electrostatic waves stimulated by the sounder pulse. In some cases these waves are received after being reflected in the nearby medium (for the f_N and f_T resonances or the nf_H resonances, $n = 3$, 4). In other cases the signal reception is due to the matching of a component of the wave group velocity to the satellite velocity (for the f_{Qn} resonances and the higher-order nf_H resonances, $n \geq 5$).

However, the above oblique echo theory for electrostatic waves could not account for the f_H resonance. A glance at the smaller wavenumber portion of the electrostatic region of the dispersion curves in Figure 7.3 ($0.1 < kR < 1$) reveals

the striking difference between the solutions near nf_H when $n > 1$ as compared to when $n = 1$. Tataronis and Crawford (1970) examined electrostatic treatments of pulse excitation of the plasma near f_H and indicated the f_H resonance is different from the other nf_H resonances. Andrews and Fang (1971) noted that the f_H resonance is unlikely to be caused by the reflection of electrostatic waves. Muldrew and Estabrobrook (1972), and Muldrew (1972b) computed dispersion curves of the whistler mode at frequencies close to f_H and indicated that ray tracing with a complex refractive index is very difficult near f_H, and hence the f_H resonance is not yet understood. Bitoun's calculations of the ray tracing at the nf_H are invalid for $n = 1$. These authors just suggest the f_H resonance may be due to simple in-phase gyration of electrons excited by the pulse, as has been proposed by Lockwood (1963), and Johnston and Nuttal (1964).

The EIDI 3 relaxation sounding rocket experiment (Higel and de Feraudy, 1977) has provided an opportunity to improve the studies of the f_H resonance (EIDI is an acronym for Experiment on the Impedance of a Dipole in the Ionosphere). This experiment, as well as the entire EIDI rocket launch program, was performed in order to study specifically the plasma resonance phenomena. The relaxation sounder in this experiment gives the signal with its envelope as in the Alouette case, and especially its waveform. The new results obtained from the EIDI 3 rocket experiment show the two main features for f_H: (1) the spectral features of the f_H resonance signal look like pure sine-waves whose frequency is very close to the electron cyclotron frequency deduced from the earth's magnetic field model (relative frequency shift less than $\sim 10^{-4}$); (2) the amplitude of the received f_H resonance signals vanish when the angle of the dipole antenna with respect to the earth's magnetic field is close to 90° and hence the f_H waves have an electric field parallel to the earth's magnetic field.

Higel and de Feraudy (1977) examined the various principal wave modes propagating close to f_H and found that the ordinary wave mode gives good

agreement with EIDI 3 results. The dispersion equation for the ordinary wave in a plasma propagating perpendicular to an external magnetic field had been investigated by Dnestrovskii and Kostomarov (1961). The numerical solution shows existence of the ordinary wave modes with small or zero group velocity for a finite k when $f_N > f_H$. The frequency of the ordinary wave is less than f_H and very close to it. Also the effects on the f_H resonance of antenna orientation with respect to the earth's magnetic field are interpreted by this mode easily

Thus f_H and nf_H resonances are attributed to wave propagation phenomena. The antenna pick up energy from the ordinary wave or the electrostatic wave (both propagating perpendicular to the earth's magnetic field) due to satellite-velocity and wave-group-velocity matching or wave reflection process.

7.5 Proton Cyclotron Echoes on the nf_H and f_H Resonances

Chen and Horita (1991) reported a new class of proton cyclotron echoes which appeared on the $3f_H$ and $4f_H$ resonance spikes of topside sounder ionograms obtained from Alouette II, ISIS I or II. Some characteristics of these echoes have been described.

Figure 7.4 shows an echo on the $4f_H$ resonance spike at an apparent range of about 650 km. The ionogram was obtained from the ISIS II satellite on May 4, 1972 at 1734:08 UT when the satellite was located at $13.5°S$, $76.4°W$ geographic coordinates and at an altitude of 1371 km. The data were collected at the Quito (QUI) ground telemetry station. The left portion of the ionogram shows a part of the fixed-frequency ionogram where the transmitter and the receiver are both fixed at a frequency value of 0.25 MHz during this time. To the right, beginning at 0.1 MHz is the swept-frequency ionogram showing the principal electron resonances at the frequencies f_N, f_T, f_H and nf_H $(n = 2, 3, \ldots)$ and the diffuse resonance at the frequency f_D. The main reflection traces of the radio waves

transmitted by the dipole antenna are also shown on the swept-frequency ionogram. These radio waves are the ordinary-wave (O-wave), extraordinary-wave (X-wave) and the Z-wave, respectively. The reflection traces result from these waves which propagate approximately vertically downward from the satellite, become reflected in the topside ionosphere and are received by the sounder receiver. The lowest frequency for a particular wave mode (Z, O, or X) which can propagate is called the mode cutoff, labelled by f_zS, f_oS $(= f_N)$ or f_xS, respectively, where S signifies the satellite height. The cutoffs occur at frequencies for which the refractive index for that mode is zero.

Here, however, we are interested only in the study for the proton cyclotron echoes. The regular proton cyclotron echoes observed and studied previously occur clearly at an apparent range of about 650 km at frequencies below and just above the f_H resonance (below the f_D resonance). This type of proton cyclotron echoes also occur on the fixed-frequency ionogram. Higher harmonics to the third of the proton cyclotron echo are shown on both the fixed- and swept-frequency ionograms. Previous work indicates that proton cyclotron echoes only occur at frequencies below the electron plasma frequency f_N and predominantly at frequencies slightly above the electron cyclotron frequency f_H. But in this figure an proton cyclotron echo is observed on the $4f_H$ resonance spike. The $3f_H$ resonance is masked by the f_N and f_T resonances. Also we note that the modulation of the f_N resonance on the swept-frequency ionogram is observed. This modulation corresponds to the proton cyclotron frequency.

Figure 7.5 shows another ionogram obtained about 45 s later still displaying the echo on the $4f_H$ resonance spike and the modulation related to the proton cyclotron frequency on the f_N resonance spike. Only the fundamental echo and its second harmonic of the regular proton cyclotron echoes are observed. The regular proton cyclotron echoes are barely visible on the fixed-frequency ionogram and below f_H on the swept-frequency ionogram. These are due to the

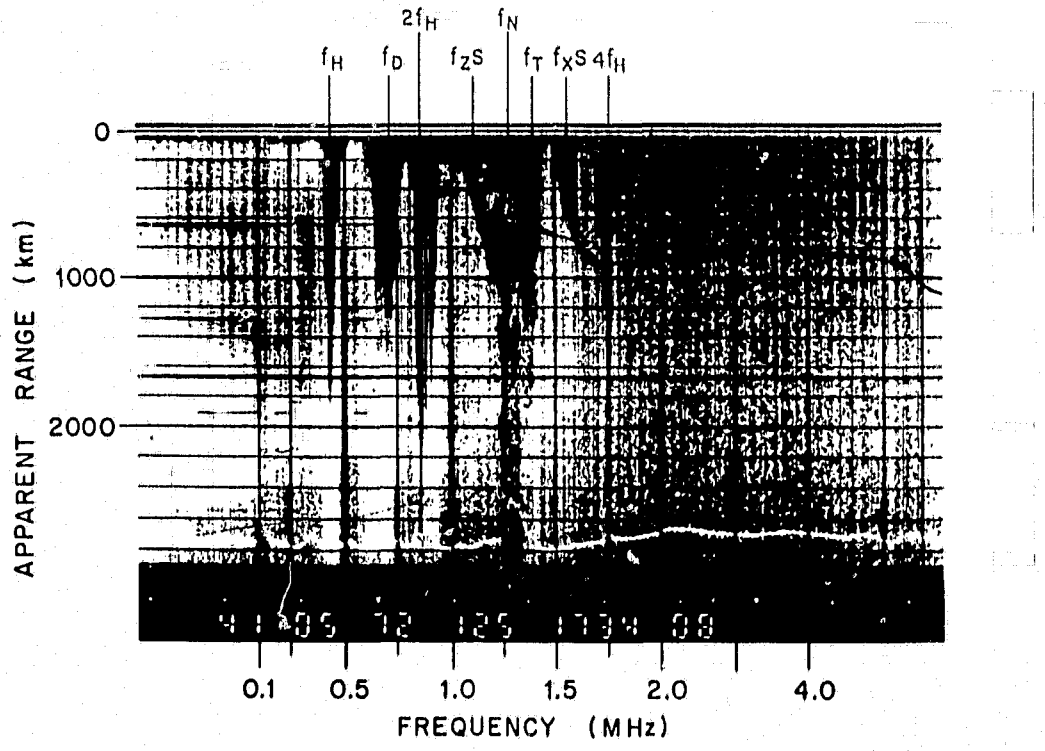

Figure 7.4: ISIS II ionogram obtained at 1734:08 UT on May 4, 1972, showing the proton cyclotron echo on the $4f_H$ resonance at an apparent range of about 650 km. The data were collected at the Quito (QUI) ground station. Also observed are the regular proton cyclotron echoes with harmonics on the fixed frequency (0.25 MHz) ionogram on the left and also on the swept frequency portion at frequencies above and below the electron cyclotron frequency f_H. After Chen and Horita (1991).

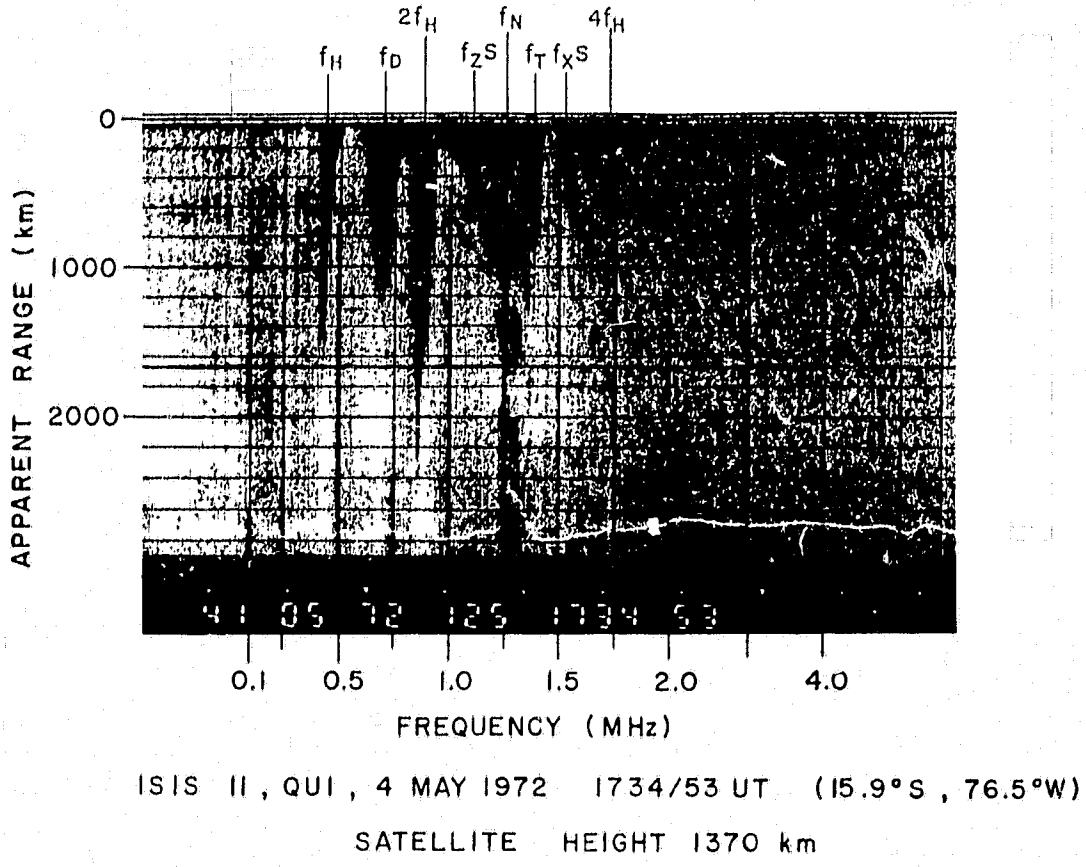

Figure 7.5: Proton cyclotron echo on the $4f_H$ resonance on an ISIS II ionogram obtained at 1734:53 UT on May 4, 1972. The data were also collected at the Quito (QUI) ground station. The regular proton cyclotron echoes are barely visible on the fixed frequency ionogram and below the f_H resonance on the swept frequency portion. After Chen and Horita (1991).

different orientation of the sounder antenna with respect to the earth's magnetic field. Up to the fourth modulation on the f_N resonance spike is observed, while only up to the third modulation occurs in Figure 7.4. Each modulation begins at an apparent range which corresponds to the one of the proton cyclotron echo and continues for about several hundred km.

Figure 7.6 shows an ionogram taken from the ISIS I satellite on February 17, 1969, at 1040:26 UT. In this ionogram the regular proton cyclotron echo just above f_H at an apparent range of about 1150 km exhibits some curvature, hard to see in Figure 7.6 but quite clear in the microfilm, while the new feature of the echo at $4f_H$ is that it is located at an apparent range greater than the maximum apparent range of the resonance spike. The previous examples showed the echoes to be located within the $4f_H$ resonance spike. The f_H resonance is also shown on the fixed-frequency (0.25 MHz) ionogram in this figure and modulated by the antenna orientation.

Figure 7.4 to 7.6 have shown some features of proton cyclotron echoes observed on the $4f_H$ resonance. Another very good example for proton cyclotron echoes on $4f_H$ resonance spike can be found in Figure 6.6 where the proton cyclotron echo exhibits double images. The two images have a difference in apparent range of about 21 km, which corresponds to a difference in frequency of about 7.5 Hz.

The proton cyclotron echoes on the $4f_H$ resonance spikes occur most frequently, and on the $3f_H$ resonance spikes somewhat less frequently. Figure 7.7 shows a proton cyclotron echo on the $3f_H$ resonance spike. The ionogram was taken from the Alouette II satellite on October 25, 1966, at 2349:24 UT. A new feature on this ionogram is the second harmonic echo located at about 1100 km. Also the regular proton cyclotron echoes occur at frequencies below and above f_H, and at frequencies just below f_D and above $2f_H$. Two more examples showing the proton cyclotron echoes on the $3f_H$ resonance are given in Figures 7.8

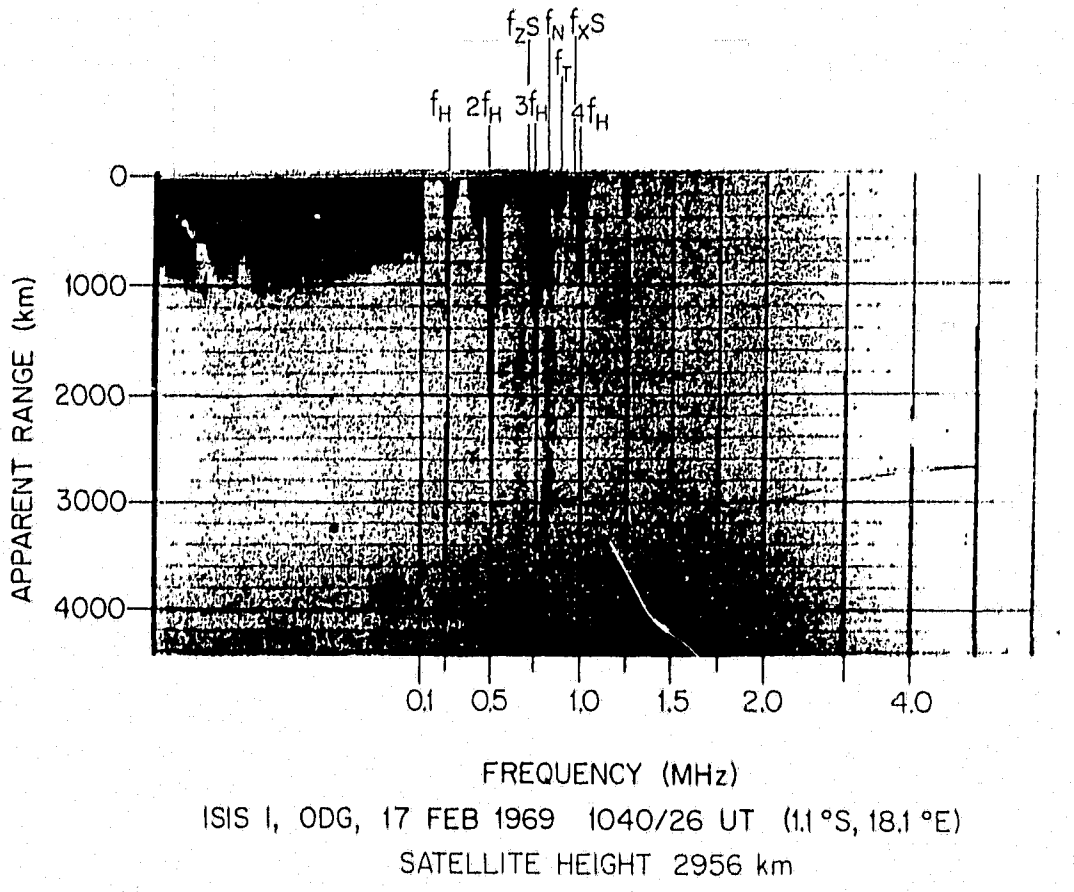

Figure 7.6: Proton cyclotron echo on the $4f_H$ resonance spike. The echo is actually below the resonance spike at an apparent range of about 1150 km. Note the regular proton cyclotron echo just above f_H has some curvature. The ground station where the data were collected was Ouagadougou (ODG). After Chen and Horita (1991).

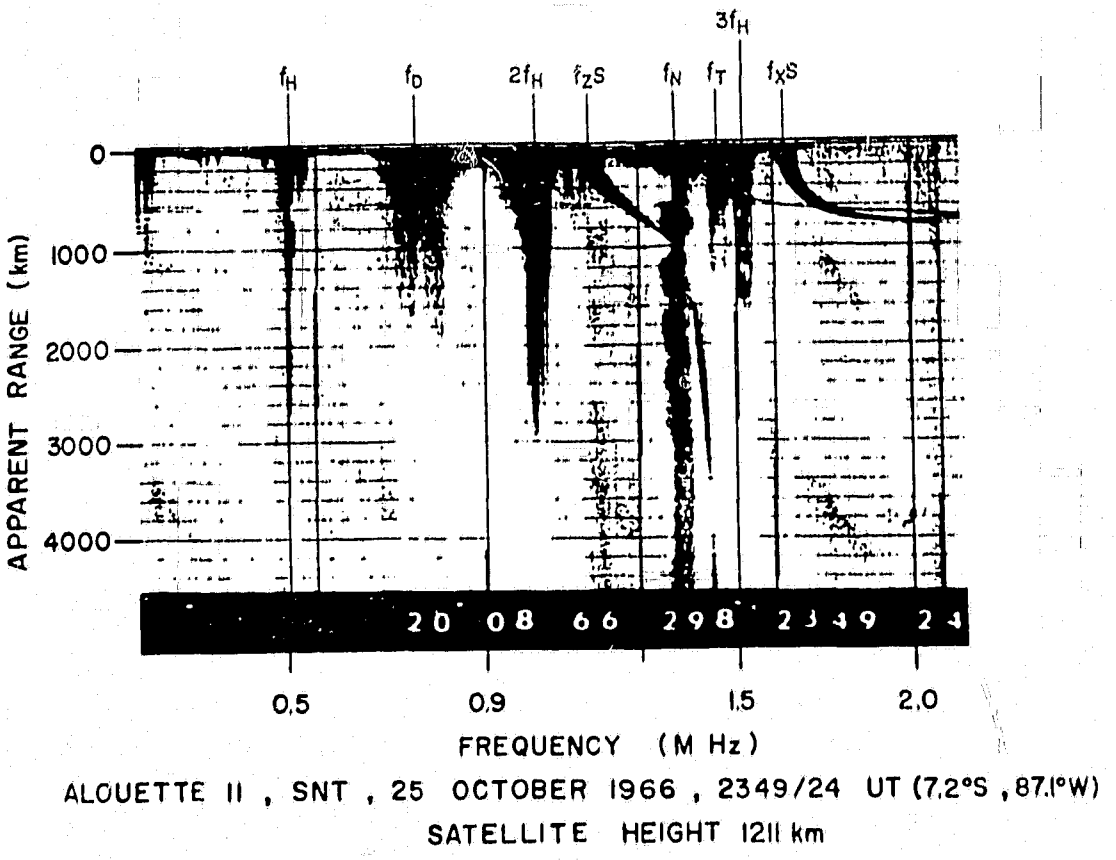

Figure 7.7: Proton cyclotron echo on the $3f_H$ resonance spike at an apparent range of about 550 km. The data were collected at the Santiago (SNT) ground station. After Chen and Horita (1991).

and 7.9.

The proton cyclotron echoes are seldom observed on the $2f_H$ resonance spikes. However we have found a very good example of the proton cyclotron echo on the $2f_H$ resonance spike, which is shown in Figure 7.10. The ionogram in this figure obtained from the ISIS I satellite at 1615:57 UT on April 23, 1969 when the satellite was located at $7.6°S$, $6.8°E$ geographic coordinates and at an altitude of 3525 km. The dip angle is $-23°$. The data of the ionogram were collected at the Ouagadougou (ODG) ground station. The echo on the $2f_H$ resonance spike is triplex with apparent ranges of about 1316 km, 1345 km and 1374 km respectively. The regular proton cyclotron echo occurs just above the f_H resonance spike at an apparent range of about 1331 km with some curvature. A spur related to the proton cyclotron echoes is attached to the f_N resonance spike.

Figure 7.11 shows an ionogram taken about 54 s prior to one in Figure 7.10. Similar but much weaker features are presented.

Previous studies have indicated that the f_H resonance and nf_H resonances have different generation mechanisms (see section 7.4). We have not observed proton cyclotron echoes on the f_H resonance spike. But we have observed proton cyclotron echoes on the fixed-frequency ionograms, which interact with the f_H resonances. For example, Figure 6.2 shows an ISIS II ionogram with the fixed-frequency portion (0.48 MHz) at the left and the swept-frequency portion at the right. The swept-frequency ionogram immediately following the fixed-frequency ionogram shows that an f_H resonance occurs at frequency about 0.48 MHz. Hence the resonance occurred on the fixed-frequency ionogram is the f_H resonance. A proton cyclotron echo appears in the f_H resonance on the fixed-frequency ionogram. The echo is doubled with apparent ranges of about 634 km and 660 km respectively. More example for interaction between the proton cyclotron echo and the f_H resonance can be found on the fixed-frequency

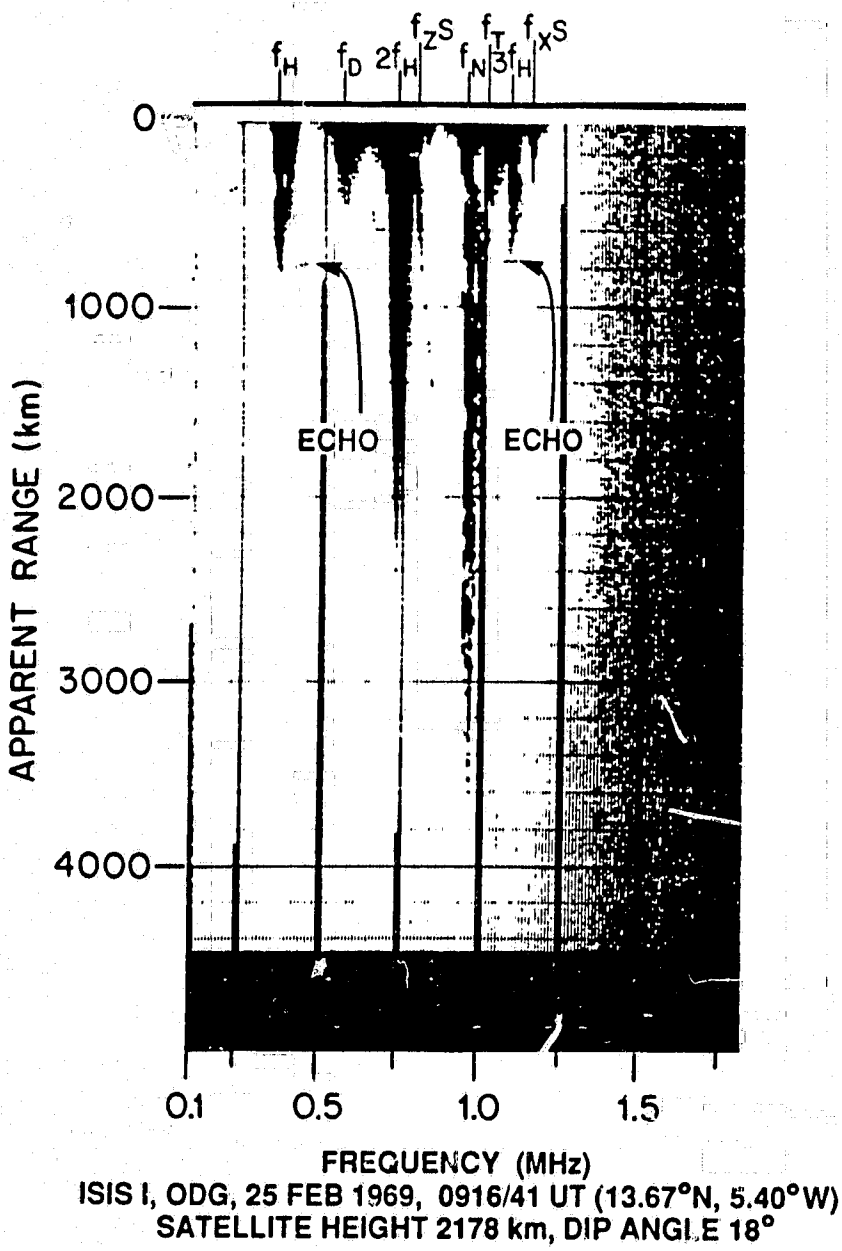

Figure 7.8: ISIS I ionogram obtained at 0916:41 UT on February 25, 1969, showing the proton cyclotron echo on the $3f_H$ resonance spike. The echo is single with apparent ranges of about 771 km. The regular proton cyclotron echo occurred at frequencies between the f_H and f_D resonance spikes with an apparent range of about 787 km exhibits curvature. The data of this ionogram were collected at the Ouagadougou (ODG) ground station.

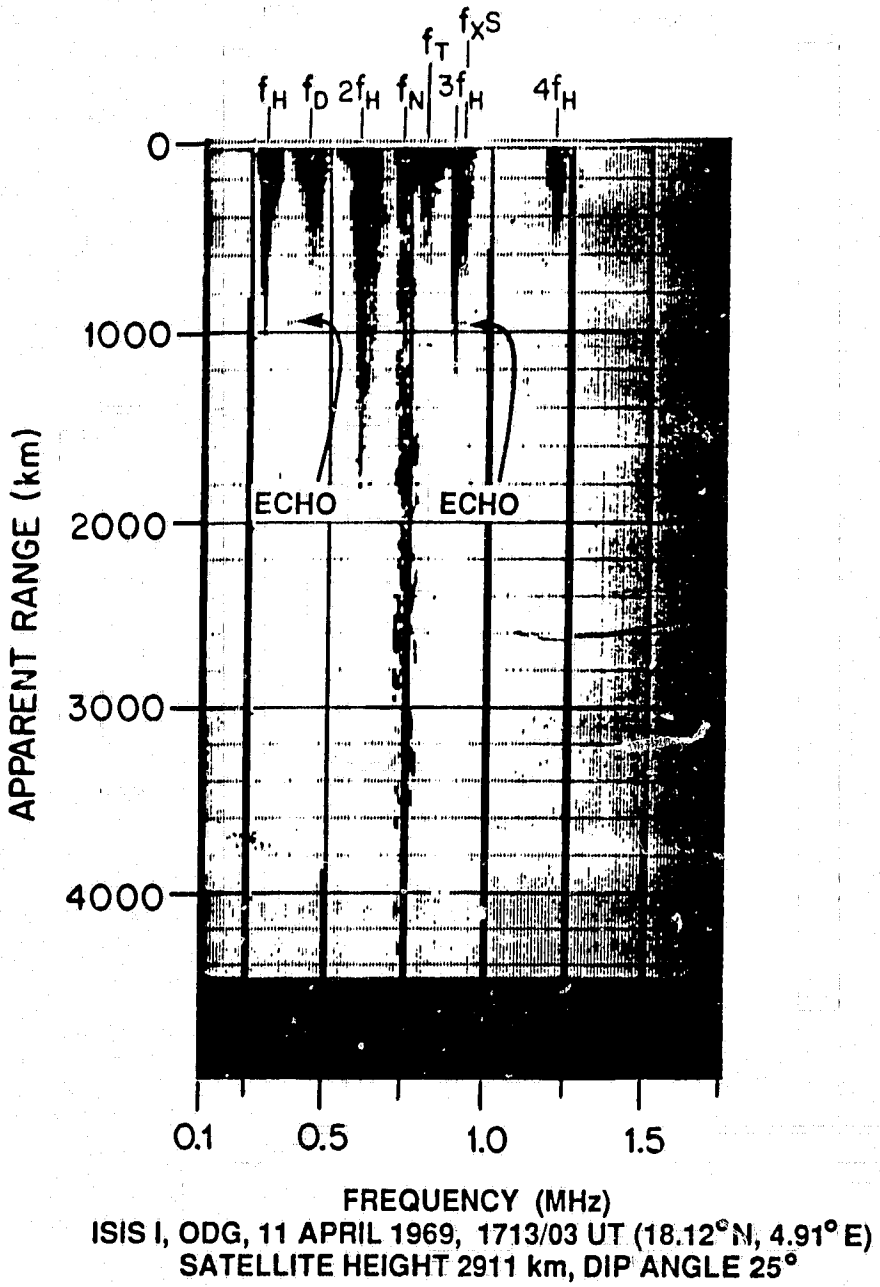

Figure 7.9: ISIS I ionogram obtained at 1713:03 UT on April 11, 1969, showing the proton cyclotron echo on the $3f_H$ resonance spike. The echo is single with apparent ranges of about 964 km. The regular proton cyclotron echo occurred at frequencies between the f_H and f_D resonance spikes with an apparent range of about 952 km exhibits curvature. The data of this ionogram were collected at the Ouagadougou (ODG) ground station.

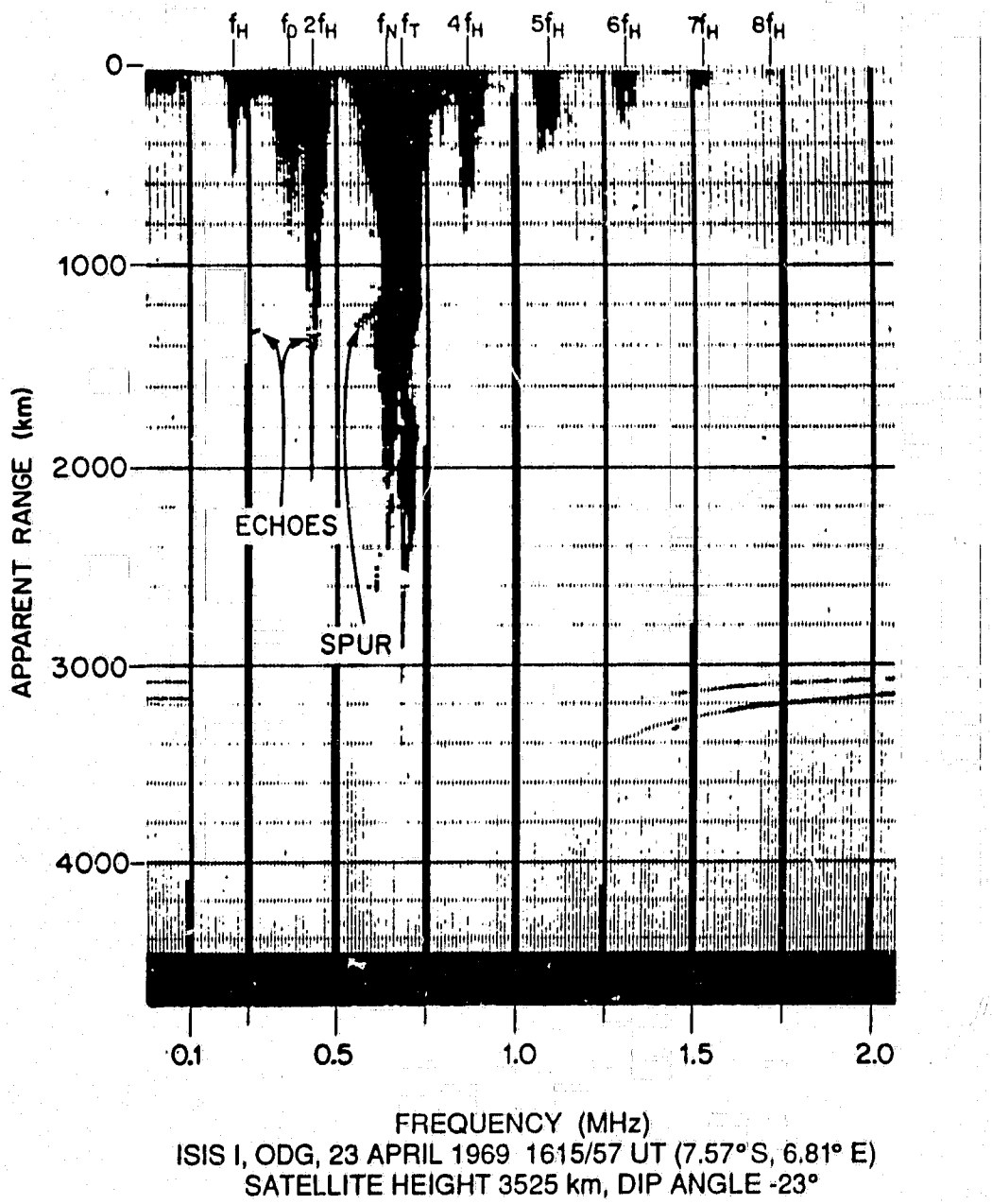

Figure 7.10: ISIS I ionogram obtained at 1615:57 UT on April 23, 1969, showing the proton cyclotron echo on the $2f_H$ resonance spike. The echo is triplex with apparent ranges of about 1316 km, 1345 km and 1374 km respectively. The regular proton cyclotron echo just above the f_H resonance spike with an apparent range of about 1331 km has some curvature. A spur related to the proton cyclotron echoes is attached to the f_N resonance spike. The data of this ionogram were collected at the Ouagadougou (ODG) ground station.

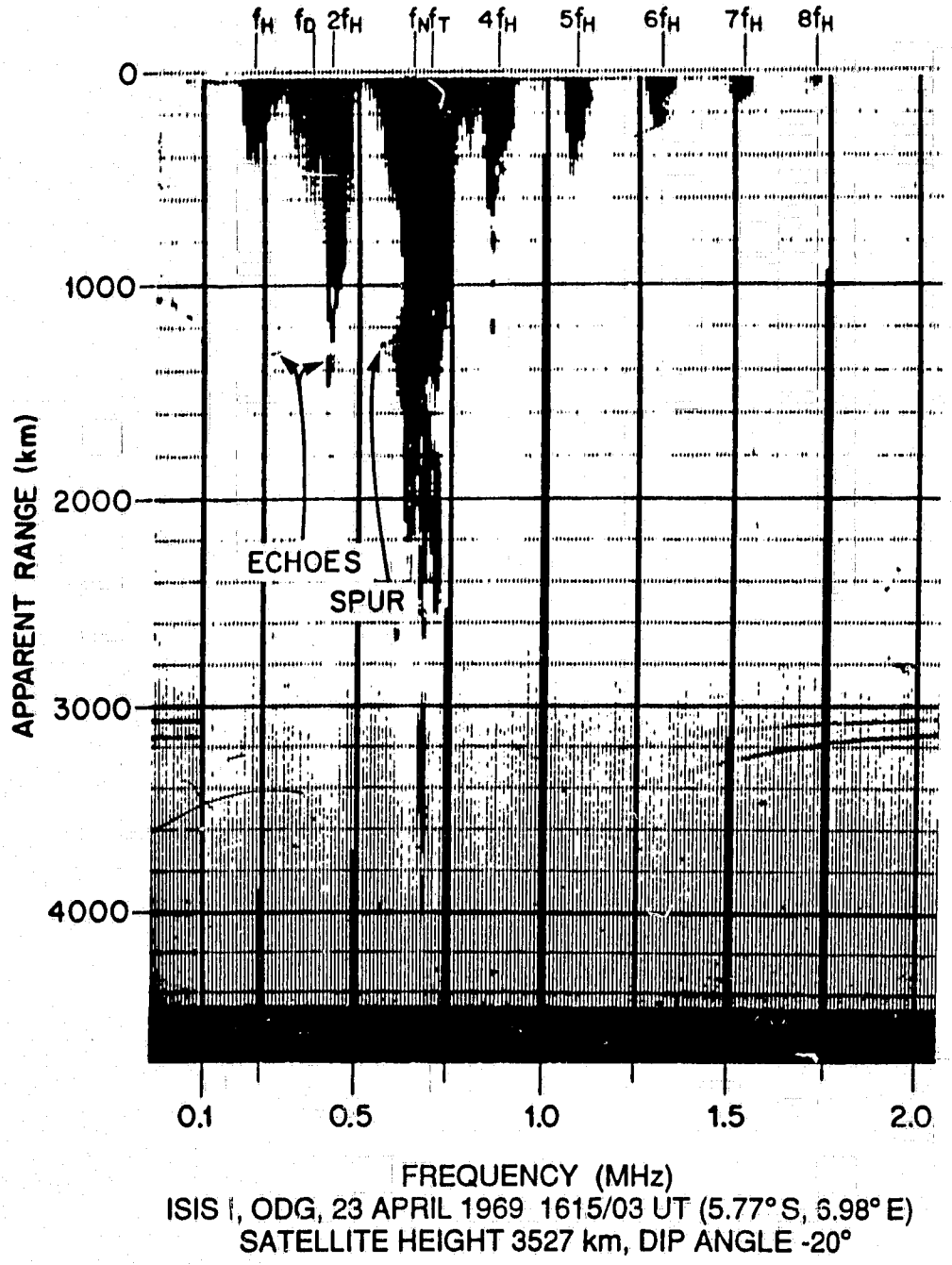

Figure 7.11: ISIS I ionogram obtained at 1615:03 UT on April 23, 1969, showing the proton cyclotron echo on the $2f_H$ resonance spike. The data were also collected at the Ouagadougou (ODG) ground station.

ionograms in Figures 6.3 and 6.4.

We have also observed absorption phenomena on the $3f_H$, $4f_H$ or f_{Q3} spikes near the proton cyclotron period on the swept-frequency ionograms occasionally. Two examples showing these absorption are given in Figures 7.12 and 7.13. Figure 7.12 shows the absorption on the $3f_H$ spike and the regular proton cyclotron occurs below the f_H resonance. The ionogram was taken by the ISIS II satellite on June 2, 1972, at 0224:35 UT. Figure 7.13 shows the absorption on the $4f_H$ spike and the regular proton cyclotron echo occurs at the frequency range between the f_H and f_D resonances. This ionogram was taken by the ISIS I satellite on February 27, 1969, at 0820:49 UT. An example showing the absorption on the f_{Q3} spike can be found in Figure 7 of the paper given by Hagg *et al.* (1969). The absorption phenomena observed on these resonances are not understood yet and further investigation is needed.

7.6 Summary

In this chapter, we have reviewed the full wave dispersion curves and previous observations and explanations of the nf_H ($n = 2, 3, 4$) and f_H resonances. Then we have presented our new observations: the interactions of proton cyclotron echoes with the f_H and nf_H resonances. The proton cyclotron echoes observed on the f_H and $4f_H$ resonances exhibit a doublet, on the $2f_H$ resonance a triplex and on the $3f_H$ resonance a singlet while the regular proton cyclotron echoes are always single. The most proton cyclotron echoes on the f_H and nf_H were observed at dip angles less than 8°, but a few examples gave values of dip angle up to 40° (Chen and Horita, 1991). A range of altitude for the proton cyclotron echoes on the f_H and nf_H resonances was observed from about 1200 km to over 3500 km.

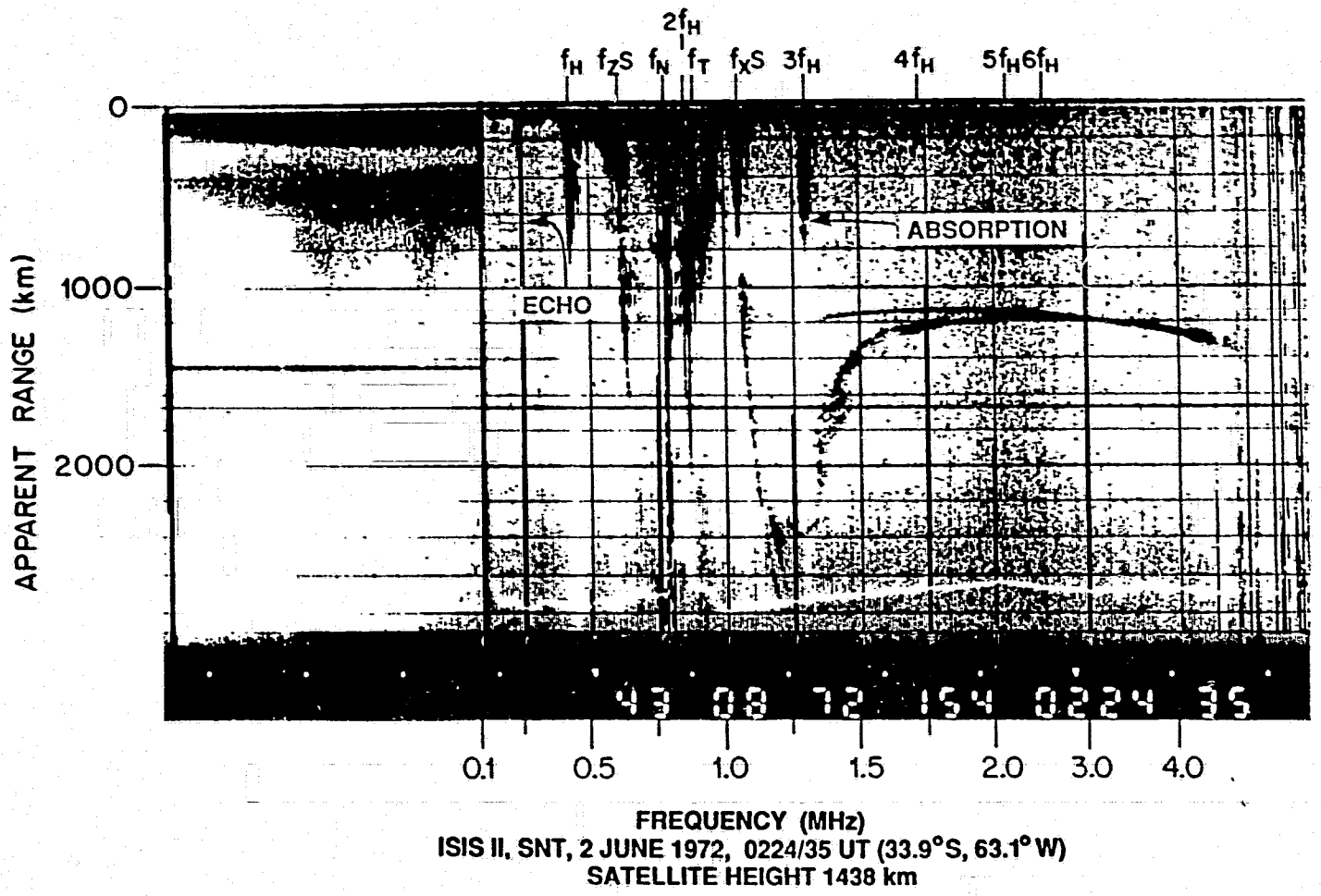

Figure 7.12: ISIS II swept-frequency ionogram showing the absorption on the $3f_H$ spike. The data were collected at the Santiago (SNT) ground station.

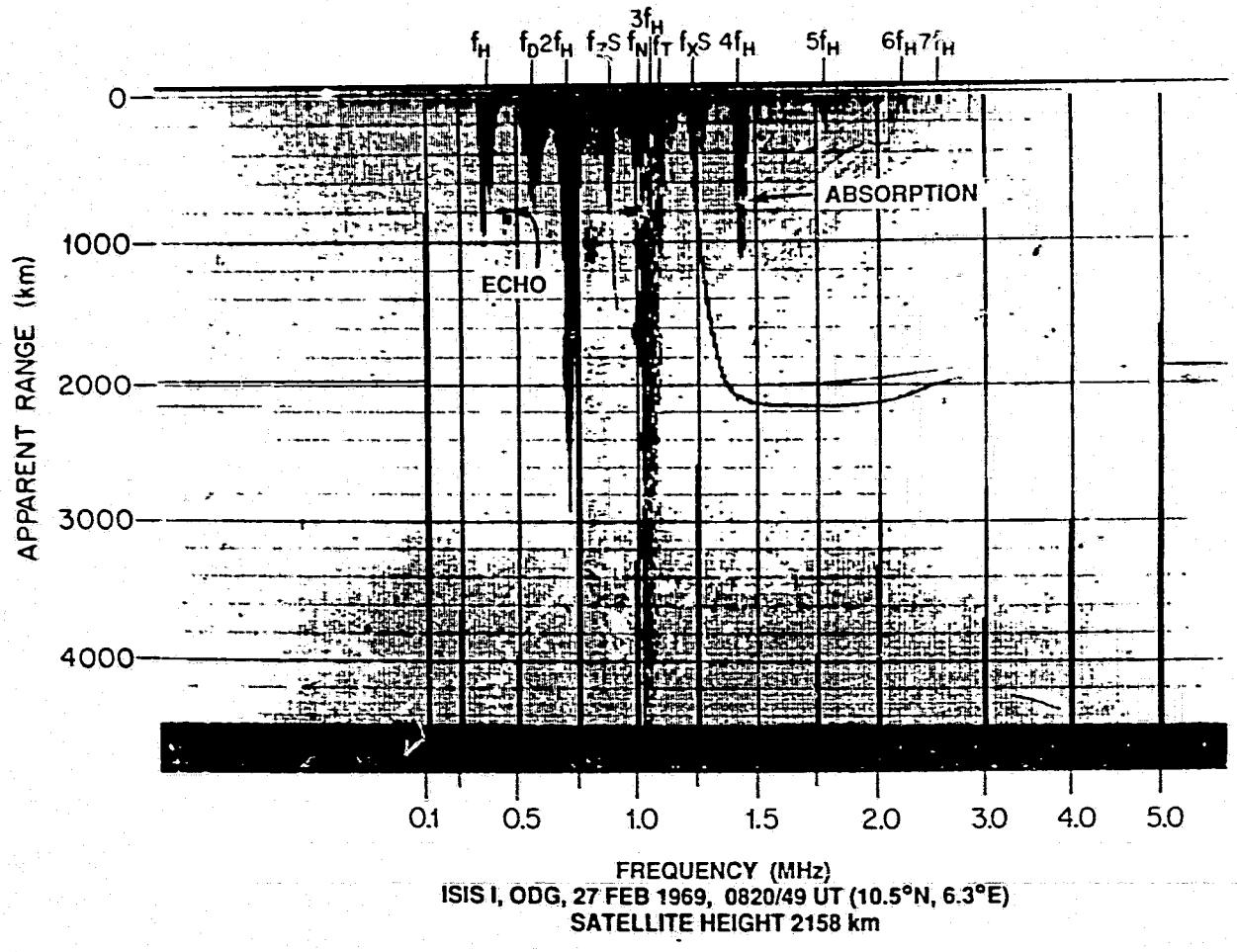

Figure 7.13: ISIS I swept-frequency ionogram showing the absorption on the $4f_H$ spike. The data were collected at the Ouagadougou (ODG) ground station.

Chapter 8

Generation Mechanism of Proton Cyclotron Echoes

8.1 Introduction

It has been over 30 years since the discovery of the electron plasma resonances and over 20 years since the discovery of the proton cyclotron echoes. Much theoretical work has been done on electron plasma resonances, but only the one paper by Oya (1978) attempted to explain the generation mechanism of the proton cyclotron echoes. The reason is, on one hand, that the electron plasma resonances are more conspicuous on ionograms than the proton cyclotron echoes, and on the other hand, the theoretical work on the proton cyclotron echoes is more difficult than on the electron plasma resonances. This chapter will be devoted to the theoretical interpretation of the proton cyclotron echoes. It must be remembered that the sounders for the Alouette-ISIS program are designed for different purposes and that, as a consequence, not all features of the proton cyclotron echoes can be determined satisfactorily from them. To better understand the proton cyclotron echoes, let's first analyze the methods of their observation and processing data.

8.2 Analysis of the Observational Methodology

So far all work on proton cyclotron echoes was mainly based on the ionograms obtained from the topside sounders aboard the Alouette-ISIS satellites. A topside sounder consists of an RF transmitter, a receiver tuned to the same frequency, and an appropriate antenna. A short pulse ($100\mu sec$) is transmitted and the

subsequent response detected by the receiver for about $15msec$. In the case of a swept-frequency mode the frequency is changed slightly while in the case of a fixed-frequency mode the frequency is not, and the process is repeated. The detected receiver output is put on the film in the form of a raster, which is called an ionogram. The ionogram consists of closely-spaced lines (like a television raster) the darkness of which corresponds to the received signal strength. The distance downward from the top of the diagram indicates the time, that is, the delay after the transmission of each sounding pulse, which is, usually, transferred to the apparent range. The lines for subsequent pulse are placed side by side in the ionogram. Thus the horizontal axis, for the swept-frequency mode, indicates the sounding frequency, and for the fixed-frequency mode, indicates the time of the sounding, or the position of the satellite. So all the information about the proton cyclotron echoes which can be extracted from the ionograms are the time of their occurrence after the termination of the sounding pulse, the frequency range of their occurrence, at which the pulse is transmitted and their intensity. The period of the proton cyclotron echo may be determined from the ionogram. Most previous work has been based on these three parameters.

The detected receiver output has another form of the presentation, called an A scan. For an A scan diagram, the ordinate is related to the amplitude of the received signal and the abscissa indicates the time following the sounding pulse. The period of the proton cyclotron echo may also be determined from the A scan diagram. Although the A scan diagram is not used in studies of the plasma resonances in topside sounding of the ionosphere as extensively as the ionogram, examples of its use can be found in the literature (e.g., Barrington and Herzberg, 1966; Ondoh *et al.*, 1975; Benson, 1975).

An excellent example illustrating the proton cyclotron echoes on both an ionogram and an A scan is given in Figure 8.1. The data were taken on the ISIS I satellite on February 27, 1973 at 0128:39 UT when the satellite was located

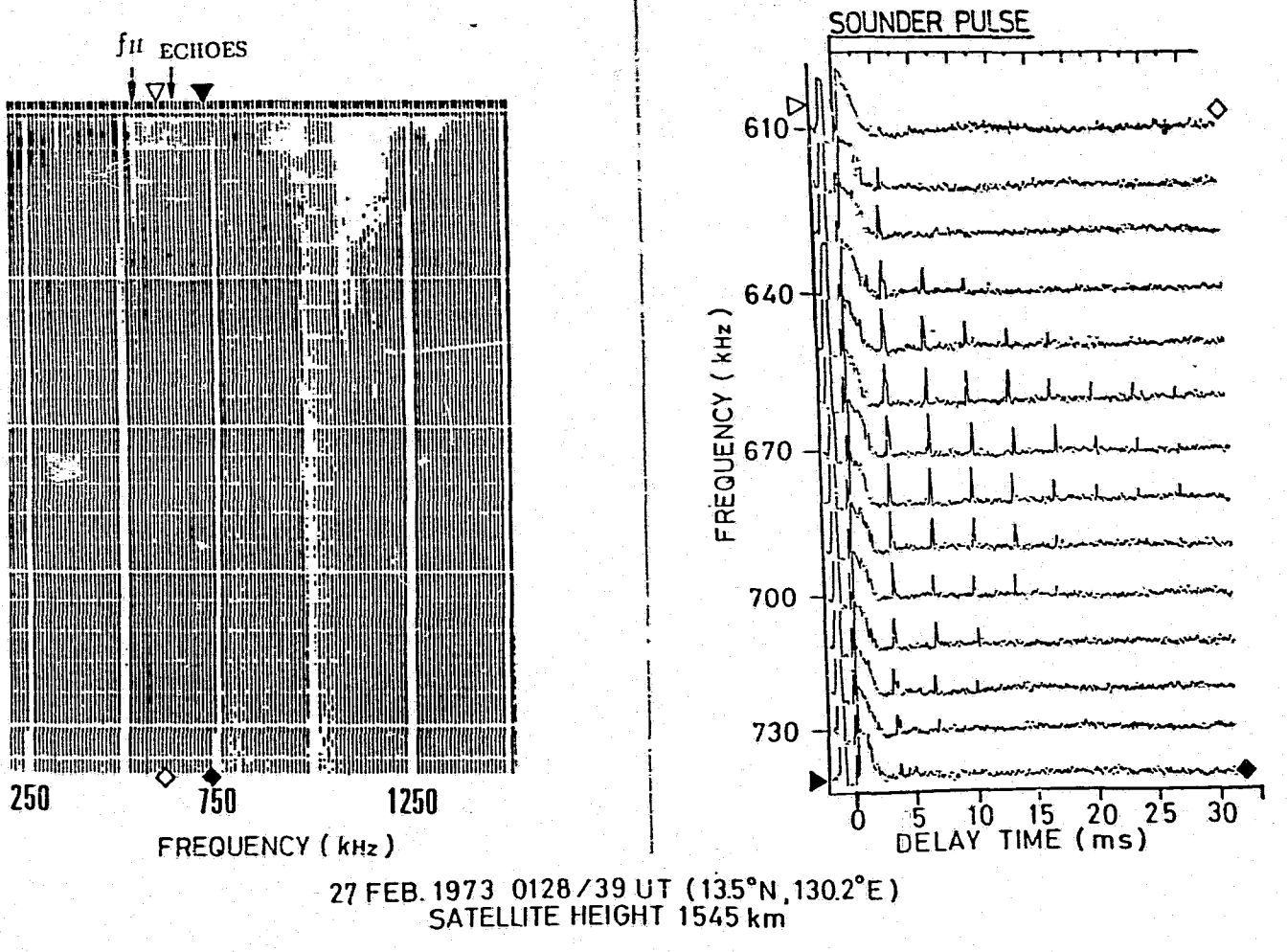

Figure 8.1: Example of the proton cyclotron echoes on both ISIS ionogram and A scan observed at 0128:39 UT on February 27, 1973 at Kashima (KSH) ground telemetry station.

at 13.5°N, 130.2°E geographic coordinates and at an altitude of 1545 km, and collected from the Kashima (KSH) ground telemetry station (36.0°N, 140.6°E), Japan. The left portion of the figure is the ionogram on which the proton cyclotron echoes occur as thin and horizontal traces between the frequency range indicated by two triangles or by two squares. The right portion of the figure shows the A scan on which the proton cyclotron echoes occur as pulse form following each sounder pulse. Up to eighth multiple echoes are shown on both diagrams.

From the A scan we can see that the proton cyclotron echoes occur as a sequence of pulses with a period equal to the proton cyclotron period. Let us look at the periodic functions and their Fourier transforms shown in Figure 8.2 where f_p and T_p are the proton cyclotron frequency and period, respectively. Obviously from this figure when n is large enough, the sequence of the pulses on the A scan in Figure 8.1 can be obtained. This suggests that a large number of multiple harmonics are involved in the proton cyclotron echoes.

However, the proton cyclotron frequency is in ULF range (0.0016 – 3 Hz, Campbell, 1967 and Fukunishi, 1987) or at most in ELF range (0.003 – 3 KHz) including its harmonics. The proton cyclotron echoes are observed at MF range (0.3 – 3 MHz, Okada and Iwai, 1988). If we assume that two waves exist near the antenna: one is related to the proton cyclotron frequency and the other is a MF wave, their interaction may produce the observed results. Let us write the former as

$$X_{pw} = A \sum_{n=1}^{N} cos(2\pi n f_p t) \tag{8.1}$$

and the latter

$$X_m = B cos(2\pi f_m t) \tag{8.2}$$

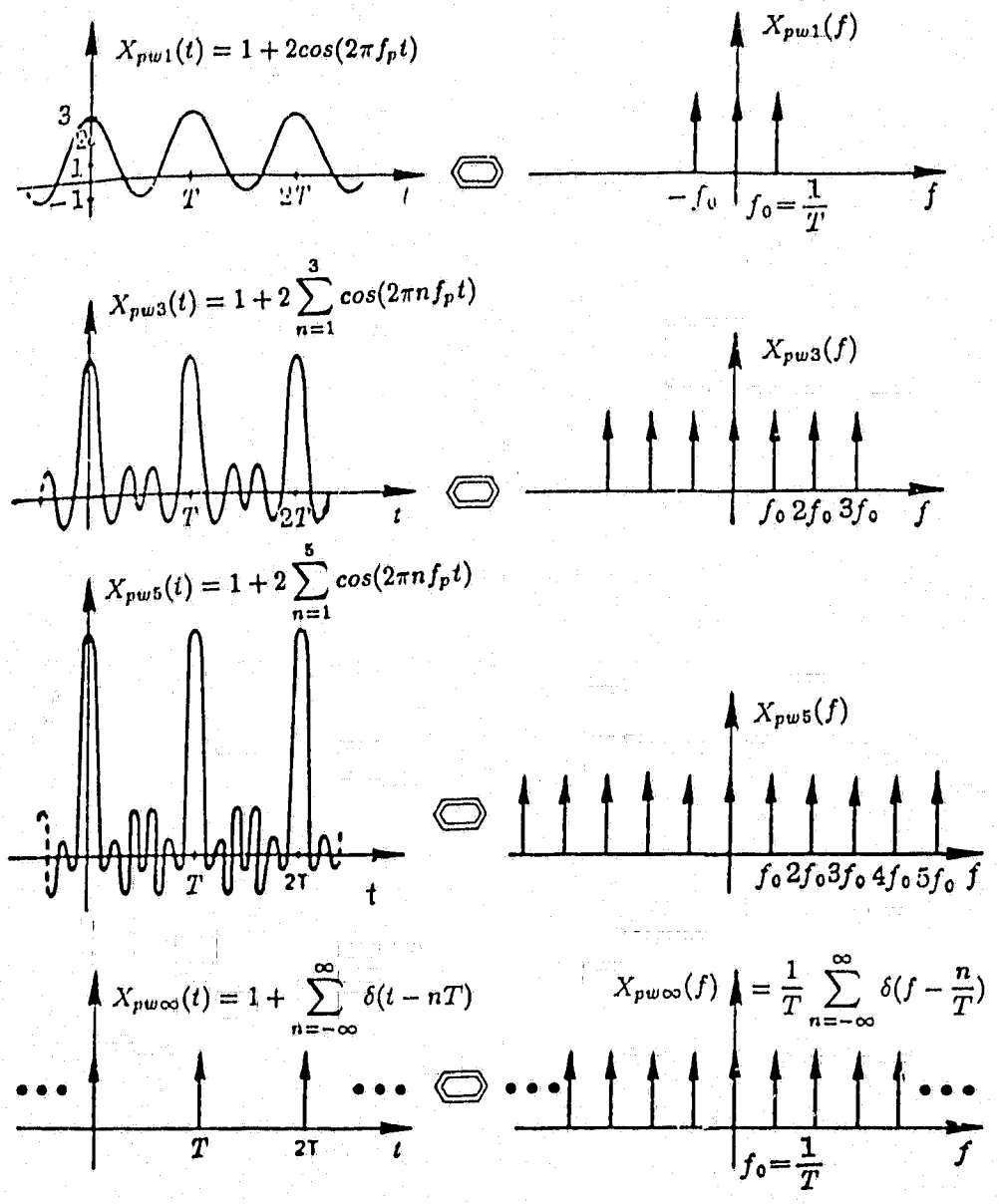

Figure 8.2: Graphical representation of equally spaced pulse sequences and their Fourier transforms. Modified from Brigham (1974).

Assume the interaction of two waves is nonlinear and we may get

$$X_{pe}^2 = (A\sum_{n=1}^{N} cos(2\pi n f_p t))^2 + 2AB\sum_{n=1}^{N} cos(2\pi n f_p t)cos(2\pi f_m t) + (Bcos(2\pi f_m t))^2 \tag{8.3}$$

since the receiver of the sounder is tuned to the center frequency of a rectangular RF pulse of $100\mu sec$ and IF bandwidth 33 KHz (Franklin and Maclean, 1969), only the second term in Equation 8.3 can be received. Since the receiver is a superheterodyne envelope detector (Franklin and Maclean, 1969), only the envelope is detected and the waveform information is lost. So the pulse sequence is observed and the MF wave does not occur on the A scan.

Improvements in the design of the VLF experiment aboard the ISIS II satellite made possible the detection of VLF signals that appear to be stimulated by pulses from the high-powered sounding transmitter. The ISIS II VLF experiment is basically a low frequency receiver covering the frequency range from .05 to 30 KHZ. The VLF receiver records the waveform of VLF signals rather than the envelope.

Ondoh *et al.* (1975) have reported that a proton cyclotron emission and its higher harmonics were observed by the VLF electric-field receiver on the ISIS II satellite at the same time as the proton cyclotron echoes. The proton cyclotron emission and its higher harmonics occur at frequencies: $f_1 = 330$ Hz, $f_2 = 690$ Hz ($f_2/f_1 = 2.09$), $f_3 = 1010$ Hz ($f_3/f_1 = 3.06$), and $f_4 = 1380$ Hz ($f_4/f_1 = 4.09$). From the time at which the proton cyclotron echo and its higher order multiple echoes we can derive the frequencies which are $f_1 = 333$ Hz, $f_2 = 660$ Hz ($f_2/f_1 = 2$), $f_3 = 999$ Hz ($f_3/f_1 = 3$), and $f_4 = 1332$ Hz ($f_4/f_1 = 4$). The two groups of frequency values are very close to each other. Thus the proton cyclotron emission observed by Ondoh *et al.* at VLF range may be corresponding to X_{pw} defined by us.

Palmer and Barrington (1973) examined VLF signals obtained from ISIS II

satellite and observed the stimulated lower hybrid resonance (LHR) emissions with a superimposed modulation at the proton cyclotron period. The emissions can be observed most readily when the sounding pulse is at near 2 MHz or near twice the upper hybrid resonance frequency and twice the electron cyclotron frequency. In this frequency range, emissions are found after each sounding pulse, and they normally decay in a fraction of the interpulse time. The wave forms of the LHR emissions are usually damped oscillations, and the proton cyclotron emissions are pulselike.

From the observations of the proton cyclotron echoes on the ionogram and the A scan, the proton cyclotron echoes (X_{pe}) are the results of interaction of two waves (X_{pw} and X_m). The proton cyclotron emissions have been observed on the ISIS II VLF experiment. Now we have to investigate that what X_{pw} and X_m are. Is the proton cyclotron emission X_{pw}? What are their generation mechanisms?

8.3 Ion Bernstein Waves

Current theoretical studies and laboratory work suggest that ion Bernstein modes are likely related to X_{pw} required, or related to the proton cyclotron emission observed. There are two different kinds of ion Bernstein waves depending upon the departure from perpendicularity for propagation across the magnetic field. The ones for which $k_z = 0$ are called pure ion Bernstein waves and the others for which k_z has a small but finite value are called neutralized ion Bernstein waves (Ault and Ikezi, 1970; Schmitt, 1973). Let us look at their dispersion relations in a Maxwellian electron-proton plasma.

Since we now investigate the lower-frequency case ($\omega \ll \omega_{ce}$), both electron

and ion motions must been considered. Equation (3.64) may be written as

$$k_x^2 + k_z^2 + \sum_{j=e,i} \frac{\omega_{pj}^2 m_j e^{-\lambda_j}}{\kappa T_{\|j}} \sum_{n=-\infty}^{\infty} I_n(\lambda_j) \Bigg\{ 1 + i \left[\alpha_{nj} - \frac{n\omega_{cj}}{k_z} \left(\frac{m_j}{2\kappa T_{\|j}} \right)^{1/2} \frac{T_{\|j}}{T_{\perp j}} \right] F_0(\alpha_{nj}) \Bigg\} = 0 \tag{8.4}$$

and we still take the approximation in equation (6.5). Thus equation (8.4) becomes

$$k_x^2 + k_z^2 + \sum_{j=e,i} \frac{\omega_{pj}^2 m_j e^{-\lambda_j}}{\kappa T_{\perp j}} \sum_{n=-\infty}^{\infty} I_n(\lambda_j) \frac{n\omega_{cj}}{\omega + n\omega_{cj}} = 0 \tag{8.5}$$

For pure Bernstein waves, $k_z = 0$, and hence equation (8.5) may be written as

$$1 + \sum_{j=e,i} \frac{\omega_{pj}^2}{\omega_{cj}} \frac{e^{-\lambda_j}}{\lambda_j} \sum_{n=-\infty}^{\infty} \frac{n I_n(\lambda_j)}{\omega + n\omega_{cj}} = 0 \tag{8.6}$$

After similar treating to that for electron in chapter 6, equation (8.6) becomes

$$1 = \sum_{j=e,i} \frac{\omega_{pj}^2}{\omega_{cj}^2} \sum_{n=1}^{\infty} \frac{e^{-\lambda_j} I_n(\lambda_j)}{\left(\frac{\lambda_j}{2}\right) \left[\left(\frac{\omega}{n\omega_{cj}} \right)^2 - 1 \right]} \tag{8.7}$$

which is similar to the dispersion relation for electron Bernstein waves given by Crawford (1965) (see equation (6.12)). However this dispersion relation includes the electron Bernstein waves and pure ion Bernstein waves.

Considering the wave frequency is much lower than the electron cyclotron frequency in ion Bernstein waves, equation (8.6) can written as

$$1 + \frac{\omega_{pe}^2}{\omega_{ce}^2} \frac{e^{-\lambda_e}}{\lambda_e} \sum_{n=-\infty}^{\infty} I_n(\lambda_e) + \frac{\omega_{pi}^2}{\omega_{ci}} \frac{e^{-\lambda_i}}{\lambda_i} \sum_{n=-\infty}^{\infty} \frac{n I_n(\lambda_i)}{\omega + n\omega_{ci}} = 0 \tag{8.8}$$

Using equation (6.15), then

$$1 + \frac{\omega_{pe}^2}{\omega_{ce}^2} \frac{1}{\lambda_e} + \frac{\omega_{pi}^2}{\omega_{ci}} \frac{e^{-\lambda_i}}{\lambda_i} \sum_{n=-\infty}^{\infty} \frac{n I_n(\lambda_i)}{\omega + n\omega_{ci}} = 0 \tag{8.9}$$

or

$$k_x^2 + \frac{\omega_{pe}^2 m_e}{\kappa T_{\perp e}} + \frac{\omega_{pi}^2 \omega_{ci} m_i e^{-\lambda_i}}{\kappa T_{\perp i}} \sum_{n=-\infty}^{\infty} \frac{n I_n(\lambda_i)}{\omega + n\omega_{ci}} = 0 \tag{8.10}$$

This is the dispersion relation for pure ion Bernstein waves.

For neutralized ion Bernstein waves, k_z is small but not too small. we take $\alpha_{ne} \ll 1$, but $\alpha_{ni} \gg 1$. Thus $F_0(\alpha_{ne})$ may take the approximation (Stix, equation (16), p. 193, 1962),

$$F_0 = \frac{\sqrt{\pi}\, k_z}{|k_z|} + 2i\alpha_{ne} + \cdots \tag{8.11}$$

Considering these conditions, equation (8.4) may be written as

$$k_x^2 + k_z^2 + \frac{\omega_{pe}^2 m_e e^{-\lambda_e}}{\kappa T_{\|e}} \sum_{n=-\infty}^{\infty} I_n(\lambda_e) + \frac{\omega_{pi}^2 m_i e^{-\lambda_i}}{\kappa T_{\|i}} \sum_{n=-\infty}^{\infty} I_n(\lambda_i) \frac{n\omega_{ci}}{\omega + n\omega_{ci}} = 0 \tag{8.12}$$

Using equation (6.15), we get

$$k_x^2 + k_z^2 + \frac{\omega_{pe}^2 m_e}{\kappa T_{\|e}} + \frac{\omega_{pi}^2 \omega_{ci} m_i e^{-\lambda_i}}{\kappa T_{\|i}} \sum_{n=-\infty}^{\infty} \frac{n I_n(\lambda_i)}{\omega + n\omega_{ci}} = 0 \tag{8.13}$$

This is the dispersion relation for neutralized ion Bernstein waves.

Note that pure ion Bernstein waves are dependent on the perpendicular temperature of electrons and ions to the magnetic field, whereas neutralized ion Bernstein waves of parallel temperature of them.

The dispersion properties of pure ion Bernstein waves and neutralized ion Bernstein waves are shown in Figure 8.3. Pure ion Bernstein waves have dispersion properties comparable to the one of electron Bernstein waves. Neutralized ion Bernstein waves have nothing particular at the lower hybrid. When the wave number k becomes small or approaches zero, both types of ion Bernstein waves have zero group velocity and proton cyclotron frequency. Zero group velocity also occurs at k finite and at $k = \infty$. There are no neutralized ion Bernstein waves which frequencies are below $n\omega_{ci}$ ($n \geq 1$, integer) and this is true for pure ion Bernstein waves above the lowest hybrid frequency ω_h. This dispersion property is consistent with the observations of proton cyclotron echoes in which no echoes of the class echo minus were found, e.g., the observed proton cyclotron

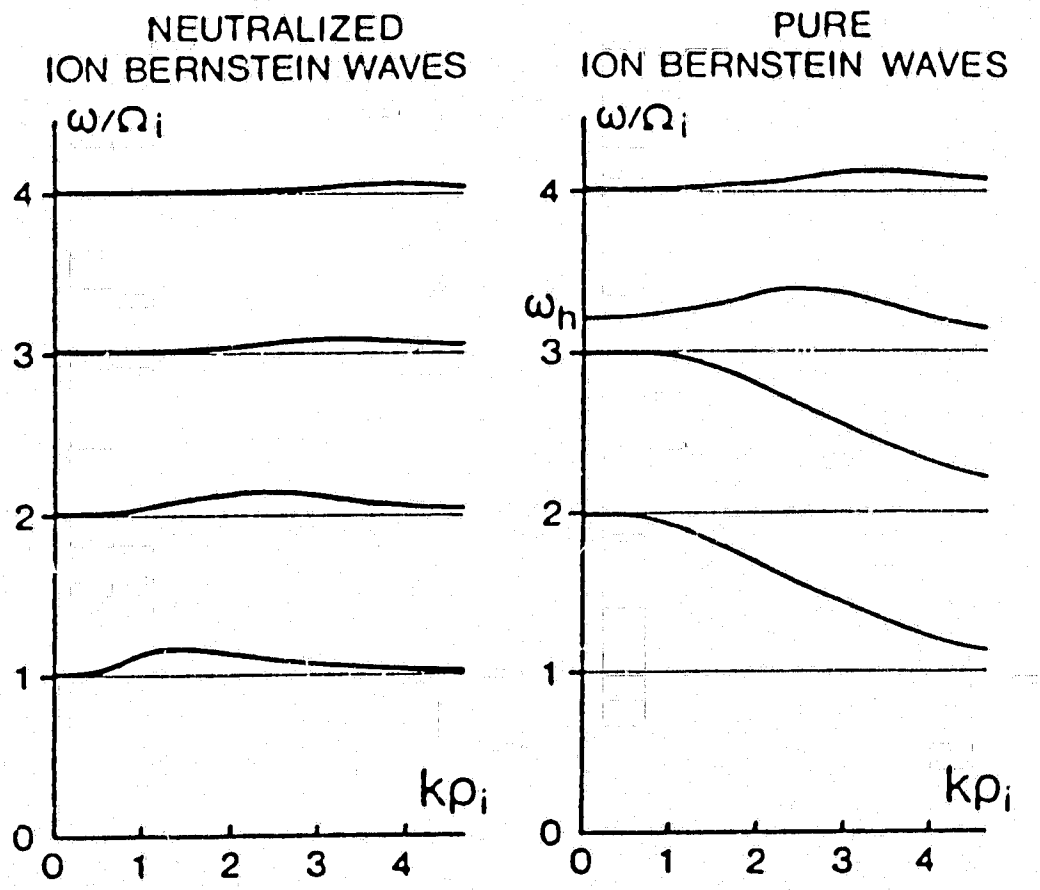

Figure 8.3: Dispersion curves for pure ion Bernstein waves and neutralized ion Bernstein waves for the same plasma conditions: $\omega_{pi} = 3\omega_{ci}$ and $T_e = T_i$ and $T_{||} = T_{\perp}$. $\omega_h = (\omega_{pi}^2 + \omega_{ci}^2)^{1/2}$ is the lowest hybrid frequency. Modified from Schmitt (1973).

periods in proton cyclotron echoes are always greater than the calculated proton cyclotron periods in the satellite location (Horita, 1987).

The ion Bernstein waves have sometimes been discussed under different title ion cyclotron waves. They are called the ion cyclotron harmonics (ICH) waves for $k_z = 0$ or the electrostatic ion cyclotron (EIC) waves for $k_z \neq 0$. The ion Bernstein waves or the ion cyclotron waves have already been observed in laboratory (D'Angelo and Motley, 1962; Motley and D'Angelo, 1963; Ault and Ikezi, 1970; Schmitt, 1973) and in space plasmas (Kintner *et al.*, 1978; Kintner, 1980; Maeda *et al.*, 1989).

8.4 Generation of Ion Bernstein Waves

In the previous section we have discussed the conditions of existence and propagation for ion Bernstein waves in terms of their dispersion relations. In the present section we will examine the generation mechanisms of ion Bernstein waves. Since the period of the proton cyclotron echoes and their repetition period are very close to the proton cyclotron period at the observation location, the controlling effect of the phenomena must be due to proton gyration in the earth's magnetic field, and since the echoes are observed after the sounding pulse, this motion of the protons must be related to the sounding pulse. Oya (1978) pointed out that when a RF pulse was applied to an antenna, a proton concentration surrounding the antenna was produced due to the negative excursion of the antenna potential. Also we should point out that in the presence of the powered pulse from the antenna, electrons and protons are strongly repelled from it due to the ponderomotive force. The ponderomotive force and its associated ponderomotive potential are given by (Chen, 1974; Swanson, 1989),

$$\mathbf{F}_p = -\frac{q^2}{4m\omega^2}\nabla(E_0^2) = -\nabla\psi \tag{8.14}$$

with

$$\psi_p = \frac{q^2}{4m\omega^2} E_0^2 \tag{8.15}$$

where q and m are electron or proton charge and mass, respectively, ω is the angular frequency of RF signal, and E_0 is the near-field RF electric field amplitude.

The ponderomotive force on the protons is smaller than that on the electrons by m_e/m_p. Hence a charge-separation field E_{cs} must created. The total force felt by the electrons is

$$\mathbf{F}_e = -\mathbf{E}_{cs} + \mathbf{F}_{pe} \tag{8.16}$$

The force on the ions is

$$\mathbf{F}_p = -\mathbf{E}_{cs} + \mathbf{F}_{pp} \tag{8.17}$$

In view of the above discussions, a ion sheath is formed near the antenna. outside the ion sheath there is an electron sheath. The region further outside has an infinite and homogeneous neutral plasma. The plasma sheath around an antenna or a conductor has been studied by many researchers (e.g., Whale, 1964; Laframboise, 1966; Rubinstein and Laframboise, 1970; Laframboise *et al*, 1975; Morin and Balmain, 1991).

The protons in the ion sheath are bunched and make cyclotron gyrations around the lines of the magnetic field. It is well known that a charged particle executes circular motion about the magnetic field lines in the magnetic field, It radiates electromagnetic waves (Bekefi, 1966; Boyd and Sanderson, 1969; Bekefi and Barrett, 1977). This is known as cyclotron emission. For a high-energy particle the electric field radiated by the charged particle is compressed into a cone about the charged particle's forward motion when viewed by a observer in the laboratory frame. As a result the observer will receive a pulsed emission whose Fourier spectrum has harmonics of the fundamental orbital frequency.

The ion Bernstein waves are likely related to this cyclotron emission of the protons in the ion sheath.

8.5 MF Waves (X_m)

When proton cyclotron echoes occur on the f_{Qn}, nf_H or f_H resonance spikes, the MF waves are simply corresponding electron electrostatic waves or electron Bernstein waves or DKO mode electromagnetic waves (see chapter 6 and 7). For regular proton cyclotron echoes, the MF waves are less understood. Ondoh *et al* (1975) suggested that the short-life mode electrostatic waves initially studied by Oya (1972) were these MF waves. The short-life mode waves are excited by the sounder MF pulse and damped out soon after their generation. They may give their energy to particles through the process of wave-particle interactions. Also there are other possibilities for the presence of the MF waves near the antenna, such as other electron electrostatic waves or DKO electromagnetic waves. These waves keep their energy around the antenna through the process of propagation and reflection or the matching of a component of the wave group velocity to the satellite velocity, as have been discussed in chapter 6 and 7, or through the process of wave trapping in cavitons.

The ponderomotive force expels the plasma from the vicinity of the wave amplitude maximum and this leads to a trough in the plasma around the satellite antenna. This plasma trough around the satellite antenna is called a caviton (Swanson, 1989). The formation of the caviton has been predicted theoretically (Zakharov, 1972; Morales and Lee, 1974 and 1977) and has been observed experimentally in laboratory (Eggleston *et al.*, 1982; Tanikawa *et al.*, 1984) and in the ionosphere (Fejer *et al.*, 1983; Wong *et al.*, 1983; Shoucri *et al.*, 1984). one of the essential features of cavitons is that the oscillating electric fields (or waves) can be trapped inside them, since the cavitons can serve as resonant

cavities. In addition, the plasma structures in cavitons or plasma sheaths are very complicated and extremely inhomogeneous. Interactions of em waves with inhomogeneous plasma will produce the conversion of em waves into es waves (Stenzel *et al.*, 1974; Wong, 1977; Muzino *et al.*, 1986).

8.6 Discussion

From the observations of proton cyclotron echoes on the ionogram and the A scan, we have suggested that the proton cyclotron echoes are the results of interaction (or modulation) of two waves. We have discussed possible candidates for the two waves or their generation mechanisms. Considering characteristics of the topside sounder receiver (envelope detector and narrow IF bandwidth), the basic features of the proton cyclotron echoes observed on the ionogram and the A scan can be explained by this model of interaction of two waves, which has been discussed in the preceding sections. The two waves interaction model can also explain other features of the proton cyclotron echoes which we have observed.

This two waves interaction model can explain the absence of echo minus (Horita, 1987) in terms of characteristics of the ion Bernstein waves, and can also explain fundamental proton cyclotron echoes and their higher order multiple echoes as the proton cyclotron emission waves consist of their fundamental frequency components and harmonics. The proton cyclotron echoes observed on the f_H, nf_H and f_{Qn} resonance spikes can be explained by the interaction of the proton cyclotron emission waves with corresponding electron waves.

From equations (8.10) and (8.13) we have known that the dispersion relations for ion Bernstein waves depend on electron and ion temperatures. Sasaki *et al.* (1993) have calculated dispersion curves of the neutralized ion Bernstein waves for some values of T_e/T_i, which are shown in Figure 8.4. From Figure 8.4 we can

see that the group velocity of the waves depends on the ratio of electron and ion temperatures. The changes of apparent ranges of the proton cyclotron observed on fixed-frequency ionograms and the curvatures of the proton cyclotron echoes observed on swept-frequency ionograms are likely related to the changes of the electron and ion temperatures.

Higel *et al.* (1972) investigated the experimental data about the envelope and the wave form of the electron resonance signals obtained by a rocket-borne RF sounder. They have found that the Fourier spectra for $3f_H$ computed from the numerical sampling of the recorded wave forms often show two peaks, about 1 kHz apart. Thus they suggested that the $3f_H$ resonance signals result from a superposition of two waves. Beating between the two waves may produce a modulation of the signal strength observed with the topside sounders (Calvert and McAfee, 1969). These modulation patterns have been observed at the $2f_H$, $3f_H$, f_N and f_T on fixed-frequency ionograms. It has also been observed that the f_{Qn} resonances often split into two resonances: f_{Qn} and $f_{Q'n}$, a few hundred hertz apart (Higel, 1978; Etcheto *et al.*, 1981). We have observed the double proton cyclotron echoes on the f_H, nf_H f_{Qn} and f_D resonances (even a triple proton cyclotron echo observed on a $2f_H$ resonance) (see Chapters 6 and 7). However the difference of the frequencies, for the double echoes, derived from their apparent ranges, is only about 8 Hz. Hence the proton cyclotron echoes have properties comparable to the ones for the electron resonances.

The ISIS II sounder can be operated with the transmitter held at a fixed-frequency and the sounder receiver swept from 0.1 to 20 MHz. An example of an ionogram obtained under such conditions is shown in Figure 8.5. The sounder transmitter is operated at the fixed frequency of 1.95 MHz on this ionogram. The most interesting thing of this ionogram is that almost all electron plasma resonances (f_N, f_T, f_H and nf_H) are excited by the pulses with a single frequency of 1.95 MHz. We should expect that the same effects occur for ions if the sounder

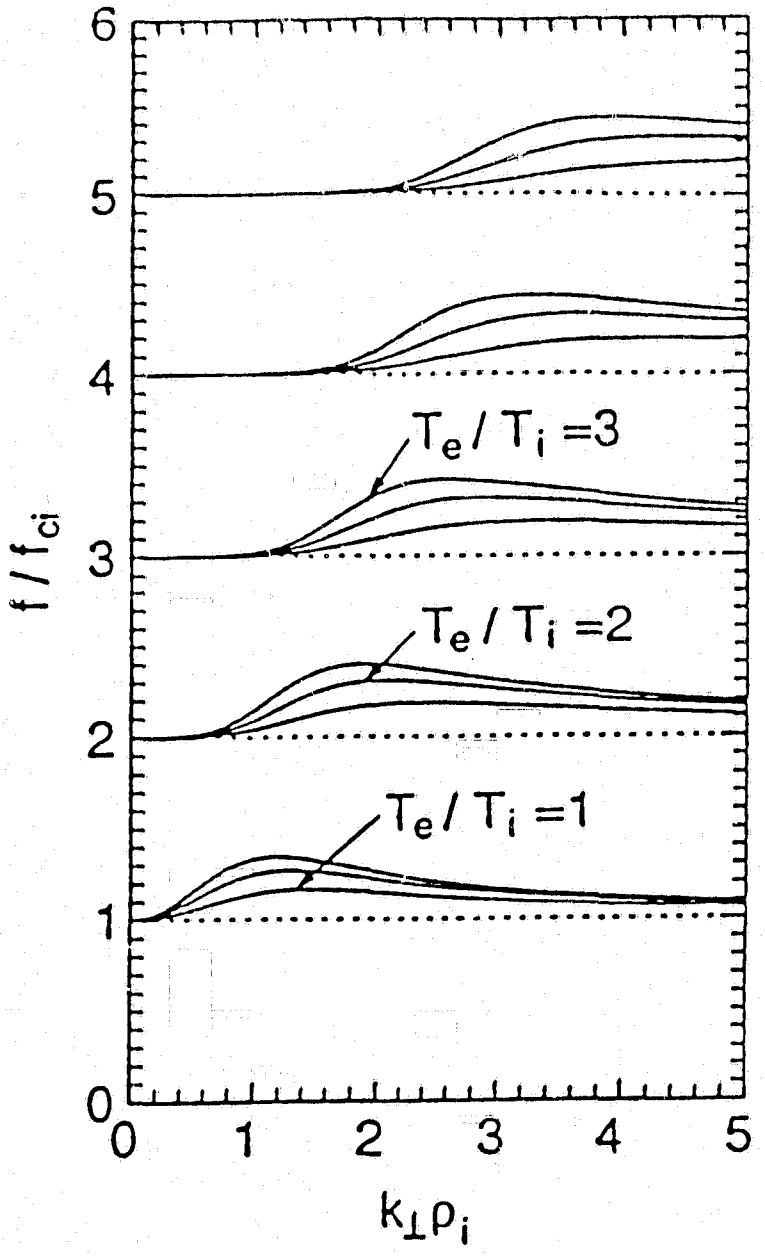

Figure 8.4: Dispersion curves of neutralized ion Bernstein waves for different values of T_e/T_i. From Sasaki *et al.* (1993).

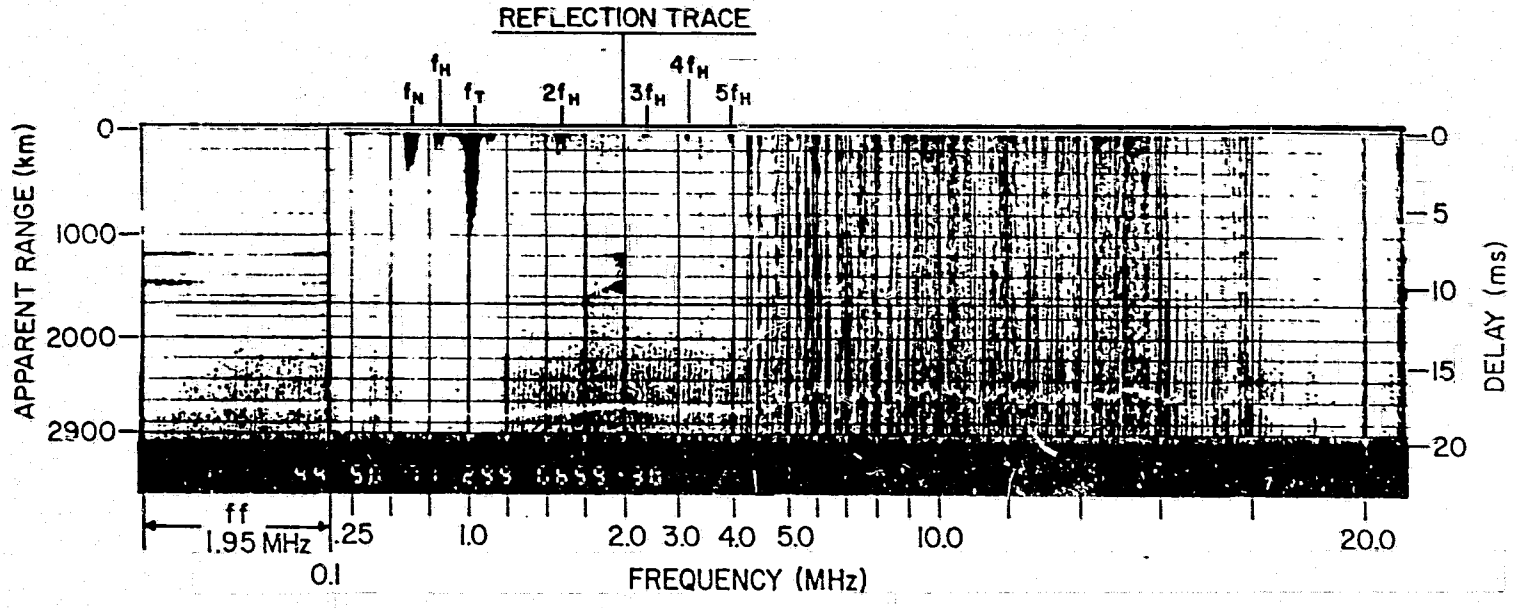

Figure 8.5: ISIS II Ionogram obtained on October 26, 1971, at 0659:30 UT when the sounder is operating at the fixed frequency of 1.95 MHz while the receiver is swept from 0.1 to 20 MHz. Here ff refers to the 3-sec period when the receiver remains tuned to the fixed frequency. The reflection trace is visible when the receiver frequency is about equal to the transmitter frequency. From Palmer and Barrington (1973).

receiver sweeps at a right range of the frequencies.

We had suggested an alternative model (Chen and Horita, 1991) for proton cyclotron echoes at $3f_H$ and $4f_H$ resonances, which was based on wave-particle interaction between the electron electrostatic waves and the protons. The essence of the model is shown in Figure 8.6. The sounding RF pulse makes the electron electrostatic waves and a proton concentration surrounding the antenna at $t = 0$. The electron electrostatic waves propagate away along the earth's magnetic field for a short distance, then return and intercept the bunched protons one gyroperiod later at time $t = T_p$ and are amplified. The amplified waves are observed at time $t = T_p + \Delta t$ (not shown in Figure 8.6) to give the $3f_H$ or $4f_H$ proton cyclotron echo. The waves that missed the interception with the bunched proton by passing through the region before or after time $t = T_p$ are not amplified and provide the normal resonance spike signals above and below the $3f_H$ or $4f_H$ echoes. This model may also be applied to the echoes at the f_{Q3} resonance.

Both wave-wave interaction and wave-particle models may interpret the proton cyclotron echoes, which occur on electron plasma resonances. However, at present it does not seem possible to distinguish between these two models without further observations and further theoretical work.

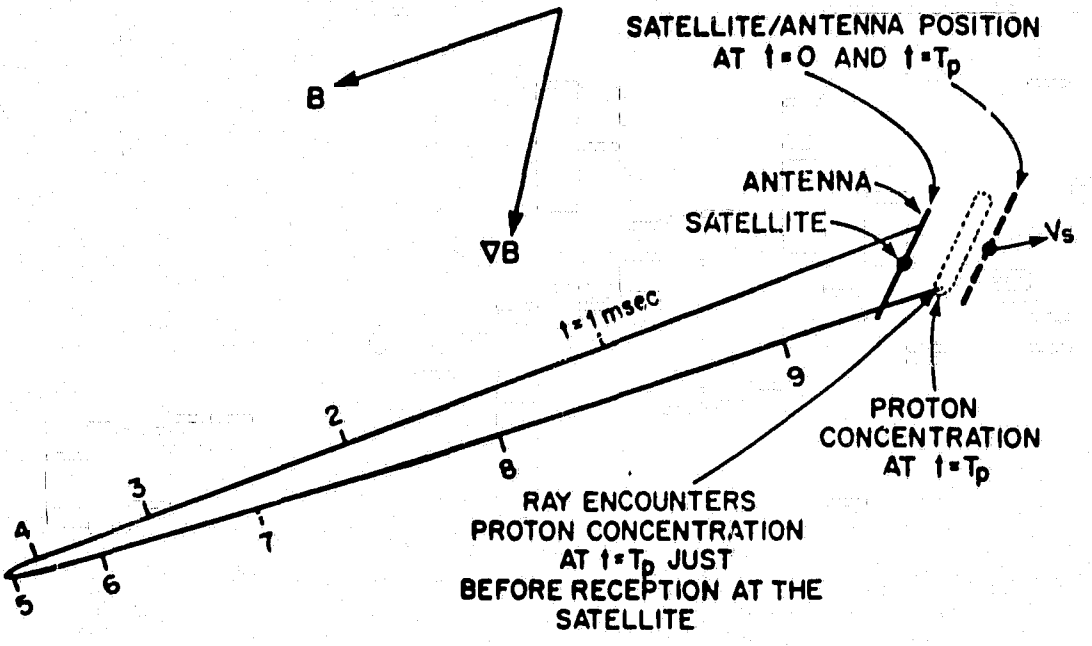

Figure 8.6: Sketch showing an electron electrostatic wave and a bunched proton concentration produced by the sounding RF pulse at time $t = 0$ both meeting a proton gyroperiod later at $t = T_p$ and being involved in wave-particle interaction. These electron electrostatic waves presumably receive energy from the protons and are amplified, leading to the $3f_H$ or $4f_H$ proton cyclotron echoes observed at time $t = T_p + \Delta t$ (not shown), while these electron electrostatic waves which missed the bunched proton concentration by passing through to the antenna before or after the protons had arrived produce the normal resonance spike above and below the echo. From Chen and Horita (1991).

Chapter 9

Conclusions

In this dissertation, the proton cyclotron echoes have been investigated in detail by using over 2000 topside sounder ionograms (both swept-frequency mode and fixed-frequency mode) obtained from the Alouette II, ISIS I and II satellites of the Alouette-ISIS program. The main results of this investigation are:

(1) Proton cyclotron echoes were first reported in 1969 on Alouette II swept-frequency ionograms. Subsequent studies were also based on swept-frequency ionograms from the Alouette-ISIS satellite observations. We have examined the combined fixed-frequency and swept-frequency ionograms obtained from the ISIS I and II satellites. Proton cyclotron echoes are first time found to occur on the fixed-frequency ionograms. Some examples of the proton cyclotron echoes observed on the fixed-frequency ionograms, which were taken from the ISIS I satellite at the ground station, Ouagadougou (ODG), Upper Volta, have been presented (Chapter 4). In addition to the features, such as constant apparent ranges and higher order multiple echoes, which have been already observed on the swept-frequency ionograms and also occur on the fixed-frequency ionograms, we have observed that under some conditions the apparent range doesn't remain constant and the proton cyclotron echo is subject to modulation in intensity. The change of the apparent range should be related to the plasma parameters or the group velocity for low group velocity electrostatic waves (ion Bernstein waves) in the vicinity of the satellite. This new information will give some insight into the generation mechanism of the proton cyclotron.

(2) In terms of the combined swept-frequency and fixed-frequency ionograms,

we have found the way to clarify effects on proton cyclotron echoes of antenna orientation with respect to the earth's magnetic field (Chapter 5). It has been long-cherished to study this subject, as this study can bring some light into the physics of the proton cyclotron echoes. However, it is not possible to do so only in terms of swept-frequency ionograms. The proton cyclotron echoes appear in a particular frequency range on the swept-frequency ionograms whereas the swept frequency is varied. Thus the proton cyclotron echoes are usually observed in a very short time period (less than 1 sec) whereas the spin period of the satellite (e.g., ISIS II) is between 17 – 24 sec. For fixed-frequency ionograms, the sounding frequency is fixed and we have observed that the proton cyclotron echoes can be under observation for several spin periods of the satellite and the proton cyclotron echo intensity is modulated by the spin of the satellite. We used satellite orbital parameters and spin axis attitude to determine the position of the satellite and the orientation of the satellite spin axis on the celestial sphere. Then the plane containing the antennas is determined since the antennas are perpendicular to the spin axis. We use the characteristics of the propagation of electromagnetic waves in the ionosphere or the magnetosphere and swept-frequency ionograms to determine the antenna orientation. It is concluded from our analysis of the combined ionograms that higher intensity and higher harmonics of proton cyclotron echoes occur when the sounding antenna is parallel to the earth's magnetic field. As this conclusion applies to the swept-frequency ionograms, the proton cyclotron echo can be readily observed on the swept-frequency ionograms only when both the right RF range and right antenna orientation are satisfied simultaneously.

(3) All previous work on proton cyclotron echoes were devoted to regular proton cyclotron echoes. The regular proton cyclotron echoes occur on the swept-frequency ionograms predominantly at frequencies below the electron plasma frequency f_N, and slightly above the electron cyclotron frequency f_H. We

have discovered a new class of proton cyclotron echoes, which occur on electron plasma resonances (Chapters 6 and 7). The proton cyclotron echoes on the f_H, nf_H ($n = 2, 3, 4$), f_{Q3} and f_D resonances have been observed and presented. Spurs observed on f_N or f_T (Benson, 1975) are likely different presentations of proton cyclotron echoes on the f_N or f_T resonances. We have checked the proton cyclotron echoes on the f_H, nf_H and f_{Q3} in more detail and their features have been presented. The proton cyclotron echoes observed on the f_H, $4f_H$, f_{Q3} and f_D resonances exhibit a doublet, on the $2f_H$ resonance a triplex and on $3f_H$ resonance a singlet while the regular proton cyclotron echoes are always single. A frequency difference of about 5 – 10 Hz exists between subechoes in a doublet or triplex echo. The regular proton cyclotron echo seems to correspond to the first echo of the double or triple proton cyclotron echoes. Apparent ranges of all proton cyclotron echoes are greater than the corresponding apparent ranges calculated from the proton cyclotron periods at the satellite locations, which are derived from the electron cyclotron resonance frequencies. The most proton cyclotron echoes on the electron plasma resonances were observed at dip angles whose magnitudes are less than 8°.

The f_H, nf_H and f_{Qn} resonances have been attributed to wave propagation phenomena. The antenna picks up energy from the ordinary electromagnetic wave (DKO mode) or the electrostatic waves (electron Bernstein mode), both propagating perpendicular to the earth's magnetic field and having very low group velocity, due to satellite velocity and wave group velocity matching or wave reflection process. We have suggested that the proton cyclotron echo is related to the ion Bernstein waves. Thus this new class of proton cyclotron echoes can be interpreted by nonlinear interactions of ion and electron Bernstein waves or ion Bernstein waves and DKO mode waves (for the f_H resonance).

We have additionally observed absorption phenomena on the $3f_H$, $4f_H$ or f_{Q3} resonance spikes near the proton cyclotron period on the swept-frequency iono-

grams occasionally. But they are not yet understood and further investigation is needed.

(4) Finally, we have presented a theory to interpret proton cyclotron echoes (Chapter 8). From the observations of proton cyclotron echoes on the ionogram and the A scan, the proton cyclotron echoes can be considered to be the result of nonlinear interaction (or nonlinear modulation) of two waves. One of the waves is suggested to be the ion Bernstein wave which is related to cyclotron emissions of bunched protons in the ion sheath. The ion sheath is formed by the high-power RF pulse. Another wave is a MF wave whose frequency is close to the frequency of the RF pulse. When proton cyclotron echoes occur on the f_{Qn}, nf_H and f_H resonances the MF waves are simply corresponding electron electrostatic waves or electron Bernstein waves or DKO mode electromagnetic waves. For regular proton cyclotron echoes, the MF waves are less well understood. However, several possibilities for their presence have been suggested. Many observational features of proton cyclotron echoes can be interpreted by this nonlinear interaction model of two waves.

Bibliography

1. Andrews, M. K., and M. T. C. Fang (1971), The propagation of plasma waves near multiples of the electron gyrofrequency, *J. Plasma Phys., 6*, 579–587.

2. Appleton, E. V., and M. A. F. Barnett (1925), On some direct evidence for downward atmospheric reflection of electric rays, *Proc. Roy. Soc. Lond., A109*, 621–641.

3. Ault, E. R., and H. Ikezi (1970), Propagation of ion cyclotron harmonic wave, *Phys. Fluids, 13*, 2874–2876.

4. Bagenal, F. (1985), Planetary magnetospheres, in *Solar System Magnetic Fields*, edited by E. R. Priest, Chapter 9, pp. 224–256, D. Reidel Pub. Co., Boston.

5. Barrington, R. E., and L. Herzberg (1966), Frequency variation in ionospheric cyclotron harmonic series obtained by the Alouette I satellite, *Can. J. Phys., 44*, 987–994.

6. Bekefi, G. (1966), *Radiation Processes in Plasma*, John Wiley and Sons, Inc., New York.

7. Bekefi, G., and A. H. Barret (1977), *Electromagnetic Vibrations, Waves, and Radiation* The MIT Press, Massachusetts.

8. Belmont, G. (1981), Characteristic frequencies of a non-Maxwellian plasma: A method for localizing the exact frequencies of intense natural waves near

f_{pe}, *Planet. Space Sci., 29*, 1251–1266.

9. Benson, R. F. (1972), Frequency shifts of ionospheric nf_H resonances, *J. Atmos. Terr. Phys., 34*, 1201–1214.

10. Benson, R. F. (1975), Ion effects on ionospheric electron resonance phenomena, *Radio Sci., 10*, 173–185.

11. Benson, R. F. (1977), Stimulated plasma waves in the ionosphere, *Radio Sci., 12*, 861–878.

12. Benson, R. F. (1982), Stimulated plasma instability and nonlinear phenomena in the ionosphere, *Radio Sci., 17*, 1637–1659.

13. Benson, R. F., and J. Bitoun (1979), Interpretation of satellite gyroharmonic resonance observations, *Radio Sci., 14*, 113–123.

14. Bernstein, I. B. (1958), Waves in a plasma in a magnetic field, *Phys. Rev., 109*, 10–21.

15. Birkeland, K. (1908), On the cause of magnetic storms and the origin of terrestrial magnetism, in *The Norwegian Aurora Polaris Expedition*, 1902–03, Aschenhoug, Oslo.

16. Bitoun, J. (1974), Analytical determination of propagation paths near gyroharmonics, *Radio Sci., 9*, 17–28.

17. Bitoun, J., L. Fleury, and B. Higel (1975), Theoretical study of gyroresonances with application to rocket experiments, *Radio Sci., 10*, 875–889.

18. Bitoun, J., P. Graff, and M. Aubry (1970), Ray tracing in warm magnetoplasma and applications to topside resonances, *Radio Sci., 5*, 1341–1349.

19. Boyd, J. M. (1964), Emission of radio noise by plasma, *Phys. Fluids, 7*, 59–63.

20. Boyd, T. J. M., and J. J. Sanderson (1969), *Plasma Dynamics*, Thomas Nelson and Sons Ltd, London.

21. Breit, G., and M. A. Tuve (1925), A radio method of estimating the height of the conducting layer, *Nature, 116*, 357–357.

22. Breit, G., and M. A. Tuve (1926), A test of the existence of the conducting layer, *Phys. Rev., 28*, 554–575.

23. Brigham, E. O. (1974), *The Fast Fourier Transform*, Prentice-Hall, Inc., Englewood Cliffs, New Jersey.

24. Budden, K. G. (1955), A method for determining the variation of electron density with height ($N(z)$ curves) from curves of equivalent height against frequency ((h', f) curves), in *The Physics of the Ionosphere*, pp. 323–339, Physical Society, London.

25. Budden, K. G. (1988), *The Propagation of Radio Waves*, Cambridge University Press, London.

26. Burch, J. L. (1987), Plasma populations in the magnetosphere, in *The Solar Wind and The Earth*, edited by S.-I. Akasofu and Y. Kamide, pp. 101–122, Terra Scientific Publishing Company, Tokyo.

27. Burrows, J. R., L. L. Cogger, and H. G. James (1981), Coordinated ionospheric and magnetospheric observations from the ISIS 2 satellite by the ISIS 2 experimenters: Volume 4 A. Large storms B. Airglow and related measurements C. VLF observations, *NSSDC/WDC-A-R&S, 81-01*, Greenbelt, MD.

28. Calvert, W. (1969), Resonances in the ionosphere, in *Plasma Waves in Space and in the Laboratory*, vol. 1, edited by J. O. Thomas and B. J. Landmark, pp. 41–54, Elsevier, New York.

29. Calvert, W., and G. B. Goe (1963), Plasma resonances in the upper ionosphere, *J. Geophys. Res., 68*, 6113–6120.

30. Calvert, W., R. W. Knecht, and T. E. VanZandt (1964), Ionosphere Explorer I satellite: first observations from the fixed-frequency topside sounder, *Science, 146*, 391–395.

31. Calvert, W., and J. R. McAfee (1969), Topside-sounder resonances, *Proc. IEEE, 51*, 1089–1096.

32. Calvert, W., and T. E. VanZandt (1966), Fixed-frequency observations of plasma resonances in the topside ionosphere *J. Geophys. Res., 71*, 1799–1813.

33. Campbell, W. H. (1967), Geomagnetic pulsations, in *Physics of Geomagnetic Phenomena*, edited by S. Matsushita and W. H. Campbell, pp. 821–909, Academic Press, New York.

34. Chapman, S., and V. C. A. Ferraro (1931a), A new theory of magnetic storms, *Terr. Magn. Atm. Elec., 36*, 77– .

35. Chapman, S., and V. C. A. Ferraro (1931b), A new theory of magnetic storms, *Terr. Magn. Atm. Elec., 36*, 171– .

36. Chapman, J. H., and A. R. Molozzi (1961), Interpretation of cosmic noise measurements at 3.8 MC/S from satellite 1960 ETA 1, *Nature, 191*, 480–480.

37. Chapman, J. H., and E. S. Warren (1968), Topside sounding of the earth's ionosphere, *Space Sci. Rev., 8*, 846–865.

38. Chen, F. F. (1974), *Introduction to Plasma Physics*, Plenum Press, New York.

39. Chen, G. H., and R. E. Horita (1991), Proton cyclotron echoes at $3f_H$ and $4f_H$ resonances, *Radio Sci., 26*, 23–29.

40. Clemmow, P. C., and J. P. Dougherty (1969), *Electrodynamics of Particles and Plasmas*, Addison-Wesley Publishing Company, Inc., London.

41. Colburn, D. S., and C. P. Sonett (1966), Discontinuities in the solar wind, *Space Sci. Rev., 5*, 439–506.

42. Cowley, S. W. H. (1980), Plasma populations in a simple open model magnetosphere, *Space Sci. Rev., 26*, 217–275.

43. Crawford, F. W. (1965), Cyclotron harmonic waves in warm plasmas, *Radio Sci., 69D*, 789–805.

44. D'Angelo, N., and R. W. Motley (1962), Electrostatic oscillations near the ion cyclotron frequency, *Phys. Fluids, 5*, 633–634.

45. Daniels, F. (1971), The ISIS-II spacecraft, *Communications Research Centre Report, 1218*, Department of Communications, Ottawa.

46. Deering, W. D., and J. A. Fejer (1965), Excitation of a plasma resonance by a small pulsed dipole, *Phys. Fluids, 8*, 2066–2079.

47. Dnestrovskii, Y. N., and D. P. Kostomarov (1961), Dispersion equation for an ordinary wave moving in a plasma perpendicular to an external magnetic field, *Sov. Phys. JETP, 13*, 986–990.

48. Dougherty, J. P., and J. J. Monaghan (1966), Theory of resonances observed in ionograms taken by sounders above the ionosphere, *Proc. Roy. Soc., Ser. 289*, 214–234.

49. Dougherty, J. P., and S. R. Watson (1971), The interpretation of plasma resonances observed by ionospheric topside sounders, in *Advances in Plasma Physics*, vol. 4, edited by A. Simon and W. B. Thompson, pp. 1–41, John Wiley, New York.

50. Eggleston, D. L., A. Y. Wong, and C. B. Darrow (1982), Development of two-dimensional structure in cavitons, *Phys. Fluids, 25*, 257–261.

51. Eastman, T. E., L. A. Frank, and C. Y. Huang (1985), The boundary layers as the primary transport regions of the earth's magnetotail, *J. Geophys. Res., 90*, 9541–9560.

52. Etcheto, J., G. Belmont, P. Canu, and J. G. Trotignon (1983), Active sounder experiments on GEOS and ISEE, in Active Experiments in Space, *Eur. Space Agency Spec. Publ., ESA-SP 95*, 39–46.

53. Etcheto, J., H. de Feraudy, and J. G. Trotignon (1981), Plasma resonance stimulation in space plasmas, *Adv. Space Res., 1*, 183–196.

54. Fejer, J. A., and W. Calvert (1964), Resonance effects of electrostatic oscillations in the ionosphere, *J. Geophys. Res., 69*, 5049–5062.

55. Fejer, J. A., H. M. Ierkic, R. F. Woodman, J. Röttger, M. Sulzer, R. A. Behnke, and A. Veldhuis (1983), Observations of the HF-enhanced plasma line with a 46.8-MHz radar and reinterpretation of previous observations with the 430-MHz radar, *J. Geophys. Res., 88*, 2083–2092.

56. Field, G. B. (1956), Radiation by plasma oscillations, *Astrophys. J., 124*, 555–570.

57. Fleming, J. A. (1902), Wireless telegraph, in *Encyclopedia Britannica*, 10th edition, vol. 33, p. 227.

58. Fleury, L., and M. Petit (1974), Antenna dependence of plasma resonance patterns, *J. Geophys. Res., 79*, 4817–4820.

59. Florida, C. D. (1969), The development of a series of ionospheric satellites, *Proc. IEEE, 57*, 867–875.

60. Franklin, C. A., and M. A. Maclean (1969), The design of swept-frequency topside sounders, *Proc. IEEE, 57*, 897–929.

61. Fukunishi H. (1987), Plasma wave phenomena in the earth's magnetosphere, in *The Solar Wind and the Earth*, edited by S.-I. Akasofu and Y. Kamide, pp. 183–212, Terra Scientific Publishing Company, Tokyo.

62. Gold, T. (1959), Motion in the magnetosphere of the earth, *J. Geophys. Res., 64*, 1219–1224.

63. Graff, P. (1967), Influence de la gyrofrequence protonique sur la resonance d'une antenna a la frequence du plasma electronique, *C. R. Acad. Sci. (Paris), 265B*, 618–620.

64. Hagg, E. L., E. J. Hewens, and G. L. Nelms (1969), The interpretation of topside sounder ionograms, *Proc. IEEE, 57*, 949–960.

65. Hamelin, M. (1980), Propagation and directive radiation properties of the cyclotron harmonic waves in a Maxwellian plasma, *Proceedings of International Conference on Plasma Physics*, 9a-II-02, p. 56, vol. I, Nagoya, Japan.

66. Heaviside, O. (1902), Telegraph, in *Encyclopedia Britannica*, 10th edition, vol. 33, p. 215.

67. Higel, B. (1978), Small scale structure of magnetospheric electron density through on-line tracking of plasma resonances, *Space Sci. Rev., 22*, 611–631.

68. Higel, B., J. Bitoun, and M. Petit (1972), Rocket observation of two waves beating at the $3f_H$ resonance, *J. Geophys. Res., 77*, 6254–6258.

69. Higel, B., and H. de Feraudy (1977), Experimental and theoretical first approach to f_H plasma resonance from a relaxation sounding rocket experiment, *Radio Sci., 12*, 879–889.

70. Holt, E. H., and R. E. Haskell (1965), *Foundations of Plasma Dynamics* The Macmillan Company, New York.

71. Horita, R. E. (1974), Proton cyclotron frequency phenomena in the topside ionosphere, *Planet. Space Sci., 22*, 793–799.

72. Horita, R. E. (1987), Proton cyclotron echoes and spurs observed on Alou ette II and ISIS II, *Radio Sci., 22*, 671–686.

73. Hultqvist, B. (1982), Recent progress in the understanding of the ion composition in the magnetosphere and some major question marks, *Rev. Geophys. Space Phys., 20*, 589–611.

74. Ichimaru, S. (1991), *Statistical Plasma Physics*, Addison-Wesley Publishing Company, Inc., Tokyo.

75. IEEE Stand. (1969), IEEE standard, *Definitions of Terms for Radio Wave Propagation, No. 211*, January 1969.

76. Jackson, J. D. (1975), *Classical Electrodynamics* John Wiley and Sons, Inc., New York.

77. Jackson, J. E. (1986), Alouette-ISIS program summary, *NSSDC/WDC-A-R&S, 86-09*, August 1986.

78. Jackson, J. E., E. R. Schmerling, J. H. Whitteker (1980), Mini-review on topside sounding, *IEEE Trans. Antennas and Propagation, AP-28*, 284–288.

79. Johnston, T. W., and J. Nuttall (1964), Cyclotron harmonic signals received by the Alouette topside sounder, *J. Geophys. Res., 69*, 2305–2314.

80. Jones, W. D., H. J. Doucet, and J. M. Buzzi (1985), *An Introduction to the Linear Theories and Methods of Electrostatic Waves in Plasmas*, Plenum Press, New York.

81. Kennelly, A. E. (1902), On the elevation of electrically conducting strata of the earth's atmosphere, *Elect. World and Eng., 15*, 473–.

82. King, J. W., and D. M. Preece (1967), Observations of proton gyro-effects in the topside ionosphere, *J. Atmos. Terr. Phys., 29*, 1387–1390.

83. Kintner, P. M., M. C. Kelley, and F. S. Mozer (1978), Electrostatic hydrogen cyclotron waves near one earth radius altitude in the polar magnetosphere, *Geophys. Res. lett., 5*, 139–142.

84. Kintner, P. M. (1980), On the distinction between electrostatic ion cyclotron waves and ion cyclotron harmonics waves, *Geophys. Res. lett., 8*, 585–588.

85. Kiwamoto, Y., and R. F. Benson (1979), Nonlinear Landau damping in the ionosphere, *J. Geophys. Res., 84*, 4165–4174.

86. Knecht, R. W., and S. Russell (1962), Pulsed radio soundings of the topside ionosphere in the presence of spread F, *J. Geophys. Res., 67*, 1178–1182.

87. Knecht, R. W., T. E. VanZandt, and S. Russell (1961), First pulsed radio soundings of the topside of the ionosphere, *J. Geophys. Res., 66*, 3078-3081.

88. Laframboise, J. G. (1966), Theory of spherical and cylindrical Langmuir probes in a collisionless, Maxwellian plasma at rest, UTIAS Rep. 100, 209 pp., University of Toronto Institute for Aerospace studies, Toronto, Canada M3H 5T6.

89. Laframboise, J. G., J. Rubinstein, and F. H. Palmer (1975), Theory of topside sounder transmission effects on antenna quasistatic sheath impedance, *Radio Sci., 10*, 773–784.

90. Landau, L. D. (1946), On the vibrations of the electronic plasma, *J. Phys. (U.S.S.R.), 10*, 25–34.

91. Lockwood, G. E. K. (1963), Plasma and cyclotron spikes phenomena observed in topside ionosphere, *Can. J. Phys., 41*, 190–194.

92. Lockwood, G. E. K. (1965), Excitation of cyclotron spikes in the ionospheric plasma, *Can. J. Phys., 43*, 291–297.

93. Lockwood, G. E. K., and L. E. Petrie (1963), Low latitude field aligned ionization observed by the Alouette topside sounder, *Planet. Space Sci., 11*, 327–330.

94. Lui, A. T. Y. (1987), Road map to magnetotail domains, in *Magnetotail Physics*, edited by A. T. Y. Lui, pp. 3–9, The Johns Hopkins University Press, Baltimore.

95. Lundin, R. (1988), On the magnetospheric boundary layer and solar wind energy transfer into the magnetosphere, *Space Sci. Rev., 48*, 263–320.

96. Maeda, K., S. F. Fung, and W. Calvert (1990), Ion cyclotron bands in VLF saucers, *Planet. Space Sci., 38*, 507–516.

97. Mar, J., and Garrett, T. (1969), Mechanical design and dynamics of the Alouette spacecraft, *Proc. of the IEEE, 57*, 882–896.

98. Matuura, N., and R. Nishizaki (1969), Proton cyclotron echoes in the topside ionosphere, *J. Geophys. Res., 74*, 5169–5172.

99. McAfee, J. R. (1968), Ray trajectories in an anisotropic plasma near plasma resonance, *J. Geophys. Res., 73*, 5577–5583.

100. McAfee, J. R. (1969a), Topside resonances as oblique echoes, *J. Geophys. Res., 74*, 802–808.

101. McAfee, J. R. (1969b), Topside ray trajectories near the upper hybrid resonance, *J. Geophys. Res., 74*, 6403–6408.

102. McAfee, J. R. (1970), Topside plasma frequency resonances as oblique echoes below the cyclotron frequency, *J. Geophys. Res., 75*, 4287–4290.

103. McAfee, J. R. (1973), Electron plasma resonances in the topside ionosphere, *Fundamentals of Cosmic Phys., 1*, 71–118.

104. Mizuno, K., J. S. DeGroot, and K. G. Estabrook (1986), Electron heating caused by parametrically driven turbulence near the critical density, *Phys. Fluids, 29*, 568–577.

105. Molozzi, A. R., and J. R. Richardson (1967), The measured impedance of a dipole antenna in the ionosphere, in *Space Research, 7*, pp. , North-holland Publ. Co., Amsterdam.

106. Morales, G. J., and Y. C. Lee (1974), Effect of localized electric fields on the evolution of the velocity distribution function, *Phys. Rev. Lett., 33*, 1534–1537.

107. Morales, G. J., and Y. C. Lee (1977), Generation of density cavities and loclized electric field in a nonuniform plasma, *Phys. Fluids, 20*, 1135–1147.

108. Morin, G. A., and K. G. Balmain (1991), Hydrodynamic radio-frequency model of an ion sheath near a conductor in a plasma, *Radio Sci., 26*, 459–467.

109. Motley, R. W., and N. D'Angelo (1963), Excitation of electrostatic plasma oscillations near the ion cyclotron frequency, *Phys. Fluids, 6*, 296–299.

110. Muldrew, D. B. (1969), Nonvertical propagation and delayed-echo generation observed by the topside sounders, *Proc. IEEE, 51*, 1097–1107.

111. Muldrew, D. B. (1972a), Electrostatic resonances associated with the maximum frequencies of cyclotron-harmonic waves, *J. Geophys. Res., 77*, 1794–1801.

112. Muldrew, D. B. (1972b), Electron resonances observed with topside sounders, *Radio Sci., 7*, 779–789.

113. Muldrew, D. B., and M. F. Estabrooks (1972), Computation of dispersion curves for a hot magnetoplasma with application to the upper-hybrid cyclotron frequencies, *Radio Sci., 7*, 579–586.

114. Nicholson, D. R. (1983), *Introduction to Plasma Theory*, John Wiley & Sons, New York.

115. Okada, T., and A. Iwai (1988), *Natural VLF Radio Waves*, John Wiley & Sons Inc., New York.

116. Ondoh, T., R. Nishizaki, and K. Aityo (1975), Proton gyro-emissions stimulated by MF pulses from ISIS II transmitter, *J. Atmos. Terr. Phys., 37*, 691–692.

117. Osherovich, V. A. (1987), Physical nature of the diffuse plasma resonances in the ionosphere, *J. Geophys. Res., 92*, 316–320.

118. Osherovich, V. A. (1989), Physical nature of the upper subsidiary diffuse resonances, *J. Geophys. Res., 94*, 5530–5532.

119. Osherovich, V. A., and R. F. Benson (1991), The lower subsidiary diffuse plasma resonances and the classification of radio emissions below the plasma frequency, *J. Geophys. Res., 96*, 19331–19341.

120. Oya, H. (1970), Sequence of diffuse plasma resonances observed on Alouette II ionograms, *J. Geophys. Res., 75*, 4279–4285.

121. Oya, H. (1971a), Verification of theory on weak turbulence relating to the sequence of diffuse plasma resonances in space, *Phys. Fluids, 14*, 2487–2499.

122. Oya, H. (1971b), Conversion of electrostatic plasma waves into electromagnetic waves: numerical calculations of the dispersion relation for all wavelengths, *Radio Sci., 6*, 1131–1141.

123. Oya, H. (1972), Short-life mode of electrostatic electron cyclotron harmonic waves, *J. Plasma Phys., 8*, 183–196.

124. Oya, H. (1978), Generation mechanism of proton cyclotron echoes due to pulsed radio frequency waves in space plasma, *J. Geophys. Res., 83*, 1991–2008.

125. Oya, H., A. Morioka, K. Kobayashi, M. Iizima, T. Ono, H. Miyaoka, T.Okada, and T. Obara (1990), Plasma wave observation and sounder experiments (PWS) using the Akebolo (EXOS-D) satellite-Instrumentation and initial results including discovery of the high altitude equatorial plasma turbulence, *J. Geomagn. Geoelectr., 42*, 411–442.

126. Oya, H., and T. Ono (1981), Stimulation of plasma waves in the magnetosphere using satellite Jikiken (EXOS-B), *Adv. Space Res. 1*, 217–220.

127. Oya, H., T. Ono, and T. Kamada (1981), Stimulation of plasma waves in the magnetosphere using satellite Jikiken (EXOS-B) Part 1 Observation of plasma resonances, *J. Geomagn. Geoelectr., 33*, 3–25.

128. Palmer, F. H., and R. E. Barrington (1973), Excitation of ion resonances by the ISIS II HF transmitter, *J. Geophys. Res., 78*, 8167–8179.

129. Papagiannis, M. D. (1972), *Space Physics and Space Astronomy*, Gordon and Breach, Science Publishers Ltd., New York.

130. Pottelette, R., M. Hamelin, J. M. Illiano, and B. Lembége (1981), Interpretation of the fine structure of electrostatic waves excited in space, *Phys. Fluids, 24*, 1517–1526.

131. Rubinstein, J., and J. G. Laframboise (1970), Plasma sheath around a floating cylindrical antenna at high power, *Can. J. Phys., 48*, 1882–1893.

132. Russell, C. T. (1987), The magnetosphere, in *The Solar Wind and the Earth*, edited by S.-I. Akasofu and Y. Kamide, Chapter 5, pp. 71–100, Terra Scientific Pul. Co. and D. Reidel Pul. Co., Boston.

133. Sasaki, K., T. Fujii, K. Takahashi, M. Nagatsu, and T. Tsukishima (1993), Excitation of electrostatic ion cyclotron waves by a power-modulated transversely excited atmosphere (TEA) CO_2 laser, *Phys. Fluids, B 5*, 1154–1159.

134. Schmitt, J. P. M. (1973), Dispersion and cyclotron damping of pure ion Bernstein waves, *Phys. Rev. Lett., 31*, 982–986.

135. Schwartz, S. J. (1985), Solar wind and the earth's bow shock, in *Solar System Magnetic Fields*, edited by E. R. Priest, Chapter 8, pp. 190–223, D.

Reidel Pul. Co., Boston.

136. Shkarofsky, I. P. (1968), Higher order cyclotron harmonic resonances and their observation in the laboratory and in the ionosphere, *J. Geophys. Res., 73*, 4859–4867.

137. Shoucri, M. M., G. J. Morales, and J. E. Maggs (1984), Ohmic heating of the polar F region by HF pulses, *J. Geophys. Res., 89*, 2907–2917.

138. Stenzel, R. L., A. Y. Wong, and H. C. Kim (1974), Conversion of electromagnetic waves to electrostatic waves in inhomogeneous plasma, *Phys. Rev. Lett., 32*, 654–657.

139. Stewart, B. (1878), Hypothetical views regarding the connection between the state of the sun and terrestrial magnetism, in *Encyclopedia Britannica*, 9th edition, vol. 16, p. 181.

140. Stix, T. H. (1962), *The Theory of Plasma Waves*, McGraw-Hill, New York.

141. Sturrock, P. A. (1965), Dipole resonances in a homogeneous plasma in a magnetic field, *Phys. Fluids, 8*, 88–96.

142. Swanson, D. G. (1989), *Plasma Waves*, Academic Press, Inc., Boston.

143. Tanikawa, T., A. Y. Wong, and D. L. Eggleston (1984), Trapping of plasma waves in cavitons, *Phys. Fluids, 27*, 1416–1426.

144. Tataronis, J. O., and Crawford, F. W. (1970), Alouette plasma resonance phenomena, in *Plasma Waves in Space and in the Laboratory*, vol. 2, edited by J. O. Thomas and B. J. Landmark, pp. 91–109, Edinburgh University Press.

145. Thomas, J. O. (1959), The distribution of electrons in the ionosphere, *Proc. I.R.E., 47*, 162–175.

146. Tidman, D. A. (1967), Turbulent shock waves in plasmas, *Phys. Fluids, 10*, 547–564.

147. Titheridge, J. E. (1961), A new method for the analysis of ionospheric $h'(f)$ records, *J. Atmos. Terr. Phys., 21*, 1–12.

148. Trotignon, J. G., J. Etcheto, and J. P. Thouvenin (1986), Automatic determination of the electron density measured by the relaxation sounder on board ISEE 1, *J. Geophys. Res., 91*, 4302–4320.

149. Warren, E. S., and E. L. Hagg (1968), Observation of electrostatic resonances of the ionospheric plasma, *Nature, 220*, 466–468.

150. Whale, H. A. (1964), Ion sheath effects near antennas radiating within the ionosphere, *J. Geophys. Res., 67*, 447–455.

151. Wong, A. Y. (1977), Electromagnetic wave interactions with inhomogeneous plasma, in *Laser Interaction and Related Plasma Phenomena*, edited by Helmut J. Schwarz and Heinrich Hora, Plenum, New York, Vol. 4B, PP. 783–840.

152. Wong, A. Y., J. Santoru, C. Darrow, L. Wang, and J. G. Roederer (1982), Ionospheric cavitons and related nonlinear phenomena, *Radio Sci., 18*, 815–830.

153. Zakharov, V. E. (1972), Collapse of Langmuir waves, *Sov. Phys. -JETP, 35*, 908–914.